FACULTY
OF MATHEMATICS
AND PHYSICS
Charles University

DOCTORAL THESIS

Marcel Štolc

Stars moving in gaseous medium near a galactic center

Astronomical Institute of the Charles University, Faculty of Mathematics and Physics, and Astronomical Institute of the Czech Academy of Sciences, Prague, Czech Republic

Supervisor of the doctoral thesis:	prof. RNDr. Vladimír Karas, DrSc.
Study programme:	Theoretical Physics, Astronomy and Astrophysics
Study branch:	P4F1

Prague 2024

I declare that I carried out this doctoral thesis independently, and only with the cited sources, literature and other professional sources. It has not been used to obtain another or the same degree.

I understand that my work relates to the rights and obligations under the Act No. 121/2000 Sb., the Copyright Act, as amended, in particular the fact that the Charles University has the right to conclude a license agreement on the use of this work as a school work pursuant to Section 60 subsection 1 of the Copyright Act.

In .... date ....

Author's signature

First of all, I express my gratitude to my supervisor, Prof. Vladimír Karas, for his guidance, all the time spent with me, the opportunities he provided me with, helpful comments and many discussions, and for all his patience. I wish to single out a very fruitful collaboration that I have developed in the course of time with Prof. Bożena Czerny at the Center for Theoretical Physics of the Polish Academy of Sciences in Warsaw. Further, I benefited from numerous consultations with Dr. Michal Zajaček of the Department of Theoretical Physics and Astrophysics at Masaryk University in Brno and, in the very early stages of my graduate studies, also with Prof. John Miller of the Astronomy Department, University of Oxford. I have the utmost respect for these researchers and I am truly grateful to have met them and had the opportunity to discuss with them during my PhD. studies. However, the list of people I am grateful to does not end there. My former college teachers/scientists, and colleagues all have contributed to my growth as well. Last but not least, I must not forget my family and friends. During these past 4 years, they have helped me to counter some of the hardships life has to offer, and I thank them for that.

Title: Stars moving in gaseous medium near a galactic center

Author: Marcel Štolc

Institute: Astronomical Institute of the Charles University, Faculty of Mathematics and Physics, and Astronomical Institute of the Czech Academy of Sciences, Prague, Czech Republic

Supervisor: prof. RNDr. Vladimír Karas, DrSc., Astronomical Institute of the Czech Academy of Sciences

Abstract: The standard notion of the central region of the galactic nucleus is strongly pointing toward the idea of a supermassive black hole residing in the core. The key process taking place is the gradual mass accretion fuelling the central engine. In this thesis, we focus on the well-accepted standard Shakura-Sunyaev thin accretion disc model, however, with additional perturbative elements involved. Specifically, we aim our focus on the broad (optical/UV) spectral properties of such systems and their deviations from the standard traits of the spectral energy distribution (SED). We introduce various perturbers changing either geometry of the accretion flow, namely i) optically thin plasma component in the form of advection driven accretion flow; ii) secondary black hole component; and iii) a combination of both ingredients. We show the qualitative changes in the spectra and discuss the possibility of inferring the perturbed system parameters based certain levels of uncertainty in measured flux. We also contemplate situation in which we supplement the central component (representing a hot corona) with the dust component (representing a more distant complex environment) and discuss possible disentanglement of systems with both components present simultaneously.

Keywords: Active Galactic Nuclei – Black Holes Physics – Accretion Processes – Radiation Mechanisms

Název práce: Hvězdy pohybující se v plynném prostředí v blízkosti galaktického centra

Autor: Marcel Štolc

Institut: Astronomický ústav Univerzity Karlovy, Matematicko-fyzikální fakulta. a Astronomický ústav Akademie věd ČR, Praha, Česká republika

Vedoucí práce: prof. RNDr. Vladimír Karas, DrSc., Astronomický ústav Akademie věd ČR, Praha, Česká republika

Abstrakt: Standardní představa o centrální oblasti galaktického jádra silně směřuje k myšlence supermasivní černé díry sídlící v jádru. Klíčovým procesem, který probíhá, je postupné narůstání hmoty zásobující centrální motor. V této práci se zaměřujeme na dobře přijímaný standardní Shakura-Sunyaev model tenkého akrečního disku, avšak s dalšími perturbačními prvky. Konkrétně se zaměřujeme na širokopásmové (optické/UV) spektrální vlastnosti takových systémů a jejich odchylky od standardních vlastností spektrální distribuce energie (SED). Zavádíme různé perturbery měnící buď geometrii akrečního toku, a to i) opticky tenkou složku plazmatu ve formě advekčně řízeného akrečního toku; ii) sekundární složku ve formě černé díry; a iii) kombinace obou složek. Ukazujeme kvalitativní změny ve spektrech a diskutujeme o možnosti odvodit parametry narušeného systému na základě určitých úrovní nejistoty měřeného toku. Uvažujeme také o situaci, kdy doplníme centrální složku (představující horkou korónu) prachovou složkou (představující vzdálenější komplexní prostředí) a diskutujeme možné rozvázání systémů s oběma složkami přítomnými současně.

Klíčová slova: Aktivní Galaktická Jádra – Fyzika Černých Děr – Akreční Procesy – Radiační Mechanismy

Contents

Preface

Continued and steadily growing interest flourishes in the field of exploration of observational effects and astrophysical consequences of strong gravity that influences electromagnetic radiation originating from glowing gas, stars, and stellar-mass compact objects orbiting near supermassive black holes (Eckart et al., 2005; Melia, 2007; Raine and Thomas, 2009; Meier, 2012). Only very recently the traditional methods of astronomy based on detected properties of light, namely, spectral properties and their temporal changes, have become joined by multi-messenger physics: production of neutrinos, cosmic rays, and the effects of emission of gravitational waves (Dermer and Menon, 2009; De Angelis and Pimenta, 2018; Maggiore, 2018). The main motivation for this research arises from that fact in this way the astronomers aim to reveal the effects General Relativity, in particular, the presence of curved spacetime in the immediate vicinity of the black hole. As early as in 1960s, following the discovery of quasars (Hazard et al., 1963; Schmidt, 1963) it has been speculated that an imprint of a massive central black hole must be encoded within the radiation propagating to a distant observer. Various conditions and different geometries have been explored (e.g. Shakura and Sunyaev, 1973a; Urry and Padovani, 1995; Elvis, 2000; Czerny, 2019, and further references cited therein) with the conclusion that observed radiation spectra of a standard accretion disc (i.e., thermal, multi-black body continuum with varied temperature) should be highly variable and significantly modified by the presence of hot corona (non-thermal, power law continuum) and the spectral-line features arising from their interaction (Svensson and Zdziarski, 1994; Zdziarski, 1998; Czerny et al., 2000). The most prominent signatures have already been examined in the pioneering works, namely, the methodology of transfer functions was introduced which determine gravitational lensing of light rays and the Doppler boosting of radiation (Cunningham, 1976; Karas et al., 1992; Miniutti and Fabian, 2004; Dovčiak et al., 2004; Schnittman, 2006), as well as the associated effects of reprocessing and self-irradiation (Fukue, 1992; Sanbuichi et al., 1993; Kuncic et al., 1997; Loska et al., 2004). Figure 1 illustrates the central engine of an active galactic nucleus.

The origin of most prominent relativistic effects visible in the electromagnetic domain can be briefly described as twofold: firstly, the structure of an accretion disc and its locally generated radiation depend on the location of its inner and outer rims (typically, the innermost stable and marginally bound orbits play a prominent role), which are in turn determined by the black hole parameters and the accretion flow intrinsic characteristics (Bardeen et al., 1973; Karas, 2006; Hagen and Done, 2023). Secondly, observed spectra differ in their shape from that emitted in the local disc frame, especially when observer's inclination is large, i.e., seen at close-to-edge-on view angle (e.g. Laor, 1991; Sochora et al., 2011; Štolc and Karas, 2019).

Lack of observational data limited the pace of progress until sensitive X-ray detectors with high spectral and timing resolution started providing reliable quantitative information. It was soon confirmed that the most energetic radiation arises from the inner regions of accretion, where the emission and absorption features are revealed with shapes and energy naturally explained in terms of relativistic

Figure 1: An artist's rendering of a supermassive black hole inside Active Galactic Nucleus. The enigmatic rotating supermassive black hole resides in the centre of the system, where it is surrounded by an accretion disc feeding it with gas. The apparent color of the accretion disc material indicates the inward-growing temperature in the inner region due viscous forces of magnetic turbulent heating acting on it. A layer of light-blue pictures the radiation originating from the hot corona (the image credits: ESO, ESA/Hubble, M. Kornmesser).

effects. Large equivalent width of the fluorescence Kα line and the positioning of its energy centroid can be understood if the line is produced in a medium at very rapid rotational motion with velocity (comparable to the speed of light) near a Kerr black hole. However, the early models suffered from a large number of unconstrained parameters and various degeneracies, while the observational evidence still could not restrict the accretion models sufficiently. Excellent spectral resolution and high signal-to-noise (S/N) ratio are necessary to confirm typical, double-horn profiles, while temporal resolution can enable various approaches to mapping of the source including the Doppler tracing (Marsh and Horne, 1988; Karas and Kraus, 1996; Albright and Richards, 1996) and interferometric imaging (Event Horizon Telescope Collaboration, et al., 2019a, 2022). Even more importantly, current understanding how the black hole accretion operates shows that the standard thin-disc scenario of a stationary and axially symmetric flow does not apply to most of astrophysically realistic situations and it has to be ameliorated by additional components. In this thesis we will embark on a detailed investigation of one of the inevitable modification of the standard accretion disc scenario, namely, we will investigate the role of gaps and truncation of the flow that can be caused by secondary, embedded orbiters.

It is the aim of the present work to touch on related signatures that appear elsewhere in the electromagnetic domain outside the dominant X-rays; in particular, we discuss the UV band that nowadays appears to be very promising to offer further relevant constraints. On the other hand, we concentrate mainly on radio quiet objects that do not form prominent jets. Hence, we do not discuss electromagnetic signatures prominent is the radio domain. The ultimate goal of our research is to improve our understanding and place limits on the synergetical mechanisms between different electromagnetic processes and those producing gravitational wave signal.

Additionally the thesis focuses on the effects of the reflection of high-energetic radiation off of an cold slab of matter forming the accretion disc, such as the strongest Fe Kα line (e.g. Tanaka et al., 1995). In this scenario the main parameters are the observer inclination θ_0 ($\theta_0 = 90$ deg for an edge-on observer, i.e. in the plain of the disc) and the black-hole dimensionless spin, a/M ($0 \leq a/M \leq 1$; gravitational field of a rotating Kerr black hole in geometric units). The key role is played by the radiation emissivity profile that is geometry-dependent and radially-dependent quantity (Fabian et al., 1989). Effectively in this thesis we set the a/M ratio equal to zero, hence we assume the central body to be a non-rotating Schwarzschild black hole. The specific effects the perturbers on the spectral line profile are in agreement with the predictions made by the McKernan et al. (2013). In our scenarios, however, the former studies are broadened by the effect of the multiple perturbers of different character, or multiple perturbers present at the same time.

The thesis is organized as follows. Section 1 gives a general overview of accreting supermassive black holes. Here, we set a stage for the subsequent sections that deal with the particular problem of spectral signatures arising from black hole accretion discs that are disturbed by embedded secondary bodies orbiting the SMBH. In the section 2 we further elaborate the aim of the thesis, namely the effects of the perturbers onto the optical/UV spectra and spectral line profile. The section 3 then illustrates the results of the study, plots of optical/UV spectra as well as simulations and their respective fitting results, followed by the sections 4 and 5 discussing the results, commenting on the the potential future prospected and concluding the study, respectively.

1. Introduction

1.1 Supermassive black holes in cores of galaxies

Supermassive black holes (SMBH) are found in active galactic nuclei (AGN) and quasars, where they are born as products of the inner dynamics and evolution. Indeed, different pieces of evidence show that most of massive galaxies harbour dark, supermassive, compact bodies that can be plausibly described as SMBH of varied mass and spin. They accrete matter from the cosmic environment and reach millions to billions of solar masses (Krolik, 1999). On the other hand, stellar-mass black holes are remnants of evolved, massive stars that have undergone gravitational collapse. The latter also often appear rather frequently as a product of interaction in stellar binary systems (Karas and Matt, 2007; Miller and Miller, 2015). Furthermore, there is a widely discussed theoretical possibility of primordial black holes as well as intermediate-mass black holes (IMBH), although the evidence for the latter two categories is predominantly speculative or circumstantial (at best).[1]

Our present work focuses on selected aspects of massive black holes embedded within and interacting with the surrounding gaseous environment of disc-type geometry that has been introduced as a basis of the so-called Unification Scheme (Antonucci, 1993; Urry and Padovani, 1995). Interestingly, the idea of mass-scaling allows us to relate potential astrophysical mechanisms that can govern vastly different types of black holes in diverse objects, ranging over the entire mass range, and describe them by interrelated astrophysical concepts. Some of the massive black holes have been described as likely candidates for binary systems orbiting each other. We will consider such scenarios in our work.

Albert Einstein's field equations of General Relativity (Einstein, 1915) describe the relevant physics in geometrical terms via tensorial formalism of curved spacetime. In a standard textbook notation of General Relativity we find the following equations (Misner et al., 1973)

$$R_{\mu\nu} - \tfrac{1}{2} R g_{\mu\nu} + \Lambda g_{\mu\nu} = \tfrac{8\pi G}{c^4}\, T_{\mu\nu}. \tag{1.1}$$

The spatial part of the last equation includes the Ricci tensor $R_{\mu\nu}$, a contracted form of the Riemann tensor, the Ricci scalar R, which is a contracted form of the Ricci tensor, and the metric tensor $g_{\mu\nu}$. On the right side of the equation stands the energy-momentum tensor $T_{\mu\nu}$. Further constants involve the gravitational constant G, the speed of light c and the cosmological constant Λ.

The eq. (1.1) represent a set of tensorial equations reduces in 4-dimensional spacetime to set of ten nonlinear partial differential equations of the second order. Six of them describe the gravitational field in terms of the respective metric tensor components, whereas the remaining four equations describe the source of the gravitational field via the conservation laws. It is especially the non-linearity of the equations that causes the so called effect of "back reaction". Not only the

---

[1] Several alternatives to SMBHs, such as Dark Stars and Boson Stars have been also subject of numerous lively debates over the recent decade (e.g. Wu et al., 2022; Della Monica and de Martino, 2023). These concepts are however rather speculative at the present stage.

changes in the source induce the changes in the gravitational field, i.e. metric, but the changes in the gravitational field itself imprint the conditions for the changes of the source.

To obtain the solution to the eq. (1.1) one needs to specify the source. That is, however, not enough from the practical point of finding solutions, as the complexity of the field equations must be reduced by the proper choice of symmetries. Karl Schwarzschild proposed the first spherically symmetrical vacuum solution (t, R, θ, φ) of the gravitational field generated by the point particle or a spherical star (Schwarzschild, 1916). The corresponding form of the spacetime interval reads as

$$\mathrm{d}s^2 = -\left(1-\frac{R_\mathrm{s}}{R}\right)c^2\mathrm{d}t^2 + \frac{\mathrm{d}R^2}{(1-\frac{R_\mathrm{s}}{R})} + r^2(\mathrm{d}\theta^2 + \sin^2\theta\mathrm{d}\varphi^2), \tag{1.2}$$

with the newly defined length-scales of Schwarzschild and gravitational radii,

$$R_\mathrm{s} = 2R_\mathrm{g} = 2\frac{GM}{c^2}. \tag{1.3}$$

There are two apparent singularities in eq. (1.2) as R equals 0 or R_S. The singularity located at R_S is just coordinate singularity, i.e. provided different coordinate system, the singularity will not be present anymore (curvature invariants are finite). Nevertheless, the eq. (1.2) shows that once you cross the Schwarzschild radius the character of the radial R becomes timelike and the time coordinate t become spacelike, i.e. to stand still is equivalent to having velocity higher than the speed of light. In fact, this can be best seen in a suitable ingoing coordinates. The Schwarzschild radius indicates the distance to the surface from which even light cannot escape. The singularity at $R = 0$ is a proper spacetime singularity and cannot be cancelled out using any coordinate transformation. Hence, the Schwarzschild solution gave rise to the black hole which is located at $R = 0$ and is surrounded by the event horizon located at $R = R_\mathrm{S}$.

The general axially symmetrical vacuum solution (t, R, θ, φ) to the Einstein's field equations caused by the presence of the rotating ($a \neq 0$), both electrically ($Q \neq 0$) and magnetically ($S \neq 0$) charged point particle is called Kerr-Newman solution (Newman et al., 1965). The square of the spacetime interval then reads as follows:

$$\mathrm{d}s^2 = -\frac{\Delta}{\Sigma}\left(\mathrm{d}t - a\sin^2\theta\,\mathrm{d}\varphi\right)^2 + \frac{\sin^2\theta}{\Sigma}\Big[a\,\mathrm{d}t - (R^2+a^2)\,\mathrm{d}\varphi\Big]^2 + \frac{\Sigma}{\Delta}\,\mathrm{d}R^2 + \Sigma\,\mathrm{d}\theta^2, \tag{1.4}$$

where the metric functions are defined in terms of

$$\Sigma = R^2 + a\cos^2\theta, \quad \Delta = R^2 - 2MR + a^2 + Q^2 + S^2. \tag{1.5}$$

The solution in eq. (1.4) is, however, not astrophysically a realistic solution for $Q \neq 0$ and/or $S \neq 0$, as the electric charge of the central singularity is not observed (however, Wald, 1972; Zajaček et al., 2018) and the magnetic charge serves merely for a generalization. Setting the spin of the particle and its magnetic charge to zero we arrive at the Reissner-Nordström solution as a special case (Reissner, 1916; Nordström, 1918). Solutions such as this might be theoretically interesting, but they do not pose much of an astrophysical relevance. The astrophysically most realistic solution is axially symmetric vacuum solution of the gravitational field surrounding the rotating particle, Kerr solution Kerr (1963). We obtain it as a limit case of the Kerr-Newman solution, when setting the electrical and magnetic charge to 0. The complexity of the solution translates into the spacetime structure as illustrated in Figure 1.1. Finally setting all three parameters, a, Q and S to 0 we arrive at Schwarzschild solution as in eq. (1.2). It might be tempting to try different set of parameters of the source particles and solve the Einstein field equations for the metric coefficients. No-hair theorem, however, states that once the particles starts collapsing all of its parameters will become obsolete and only three of them remain – mass, charge and spin of the now formed black hole (e.g. Misner et al., 1973).

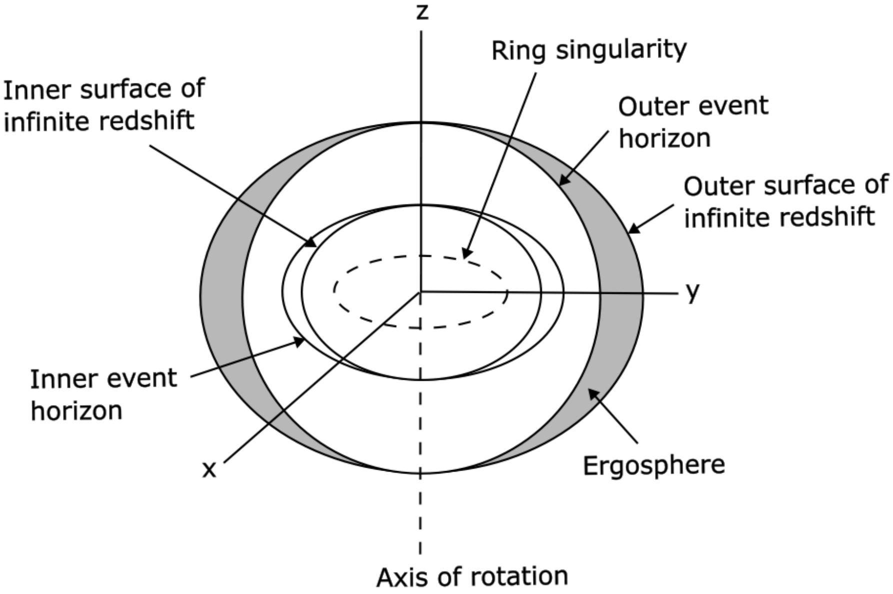

Figure 1.1: A schematic drawing of Kerr black hole horizon structure, with a non-vanishing value of spin $0 < a < 1$ (Misner et al., 1973). In the Kerr-Schild coordinates the curvature singularity takes form of a ring and is surrounded by a set of four regions that are separated by characteristic surfaces. Both the outer and inner surfaces of infinite redshift represent the static limit surfaces; test particles crossing the surfaces are unable to stand still with respect to infinity. Once crossing the outer or inner event horizon the test particles are unable to stand still with respect to infinity and additionally unable to escape the gravitational pull of the central object. The area between the outer surface of infinite redshift and the outer horizon is called the ergosphere, where the possible Penrose effect takes place (Penrose and Floyd, 1971). The altered image has been adapted from Guan et al. (2022).

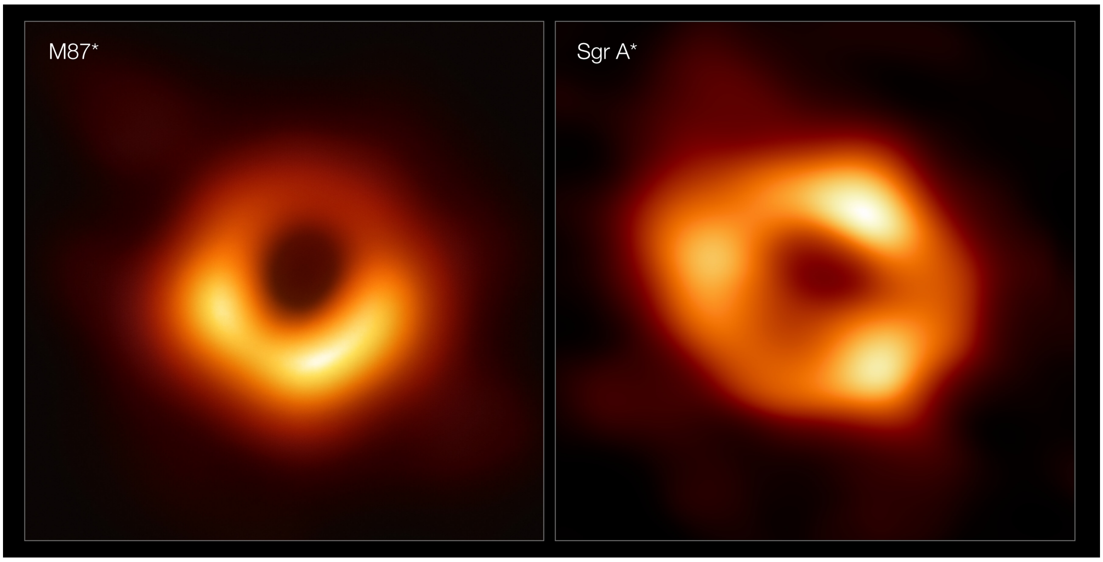

Figure 1.2: Recent evidence about SMBHs from the electromagnetic domain. Left panel: M87*, the SMBH located in the centre of the Messier 87 galaxy. Right panel: Sgr A*, the SMBH located in the centre of the Milky Way galaxy. The images of the inner accretion flow were obtained due to the usage of the following observational instruments: the Event Horizon Telescope (EHT), a global network of radio telescopes including the Atacama Large Millimeter/submillimeter Array (ALMA) and Atacama Pathfinder Experiment (APEX). Image credit: EHT Collaboration.

1.2 Gaseous environment near SMBH

The inescapable pull of black hole's gravity traps much of the surrounding matter; even light that reaches the critical surface of the event horizon must proceed towards the hidden singularity. The speed of the material falling in together with an internal friction cause the source to radiate and, rather paradoxically, it makes the darkest objects stand out as the most prominent bright sources in the Universe.

The process of central body attracting more and more mass incrementally is called accretion. This mechanism depends strongly on the geometry of the system. The choice of geometry depends mainly on the outer boundary conditions but also on the system parameters, such as the black hole spin parameter (denoted a in a dimensionless form hereafter). In case of spherical accretion the matter falls almost directly onto the central object (Bondi, 1952; Hoyle and Lyttleton, 1941) whereas it is the non-zero rotational or angular momentum of the infalling matter that leads to the formation of the disc-like structure called accretion disc. It was found that radiation efficiency of the quasi-spherical accretion is very limited (except perhaps for a possibility of formation of luminous boundary layer on the surface of a non-magnetized neutron star).

As early as in 1960s it was proposed that disc-like (toroidal) accretion around a massive black hole can explain properties of bright quasars and similarly bright galaxies (Lynden-Bell, 1969; Pringle and Rees, 1972). Originally, the idea arose from timing arguments and energy considerations (accretion is expected to vary on dynamical time-scale and it can reach very high efficiency even compared to the processes of nuclear burning on stellar cores). The accretion theory became gradually a well-established field with direct observational support. On the other hand, to this date the properties of accretion flows in galactic nuclei are understood to much less extent and physical understanding than it is with accretion in binary stellar systems. Still, the two vastly different types of objects share many common properties that allow for mass scaling of ten orders of magnitude. Geometrically thin accretion discs represent the best-understood approximation that is appropriate to objects with planar discs at (almost) Keplerian rotation and rather low accretion rates (Shakura and Sunyaev, 1973a,b; Pringle, 1981). In the present work we will treat the gaseous accretion flows in the approximation of vertically integrated quantities, although, at certain stages of the process this approximation is not appropriate, and the corresponding flows appears to be quasi-spherical and with low radiation efficiency.

Comparisons between models and observations of multiwavelength spectra are a fundamental diagnostic tool to probe the nature of accreting black holes and to reveal the geometry of these systems. To this end, both the continuum profiles and prominent spectral features from black hole accretion discs are investigated. Nonetheless, various simplifying assumptions must be introduced in order to handle computational challenges. The final goal of this effort is a self-consistent treatment of the problem with all effects of radiations transfer in strong gravitational fields taken into account. Complex conditions play a major role: the structure of density distribution, ionization properties of the environment, self/obscuration, etc.

There is a whole variety of accretion disc flavours that are based on intrinsically different model assumptions. Starting from the standard Shakura Sunyaev thin accretion disc (Shakura and Sunyaev, 1973b), the sequence then proceeds to the slim discs (Abramowicz et al., 1988), the geometrically thick fluid tori (Fishbone and Moncrief, 1976), and the intermediate case also introduced in (Abramowicz et al., 1988). A special case scenario would be represented by the puffy discs that lie in a certain sense in between the slim and thick discs and capture the effects of corona (Lančová et al., 2019), whereas Magnetically Arrested Disc scenario (MAD) assumes the presence of large-scale (organized) magnetic field (see Narayan et al., 2003, and references therein).

At the heart of viscous mass transport across the radii of the accretion disc lies the magnetorotational instability (Balbus and Hawley, 1991). The key is just a slight change in the poloidal component of the magnetic field. Should the poloidal component of the magnetic field be of rather significant value the highly ionized accreting material can adopt the MAD form and proceed along the magnetic field lines (see Narayan et al., 2003, and references therein).

Accreting black holes and neutron stars exhibit a rich phenomenology of their spectral states that are thought to correspond to different combinations of the system parameters, in particular, the accretion rate of matter falling onto the central mass, the spin of the central compact body, and the overall geometry of the accretion flow with respect to the spin axis. The *soft state* is dominated by a multi-color thermal (black-body) profile arising in the above-mentioned optically thick, geometrically thin accretion disc. On the contrary, the *hard state* is in

X-rays typically dominated by a hard power law spectrum that shows the high-energy cut-off due to Compton up-scattering of the disc seed photons in a cloud of hot electrons, referred to as the X-ray *corona*. The nature of the corona and its geometry are currently under debate (Poutanen et al., 2018). There is observational evidence for a patchy layer structure located near above the accretion disc plane, where magnetic reconnections play a crucial role (Galeev et al., 1979), or it could be a part of accretion flow dominated by advection inside a truncated disc (Eardley and Press, 1975) , or just a base of an emerging jet (Matt et al., 1992). For reviews, see e.g. Done et al. (2007); Bambi (2017).

Generally the plasma-like material behaviour is well approximated by the Boltzmann-Vlasov equation. The Boltzmann-Vlasov equation is essentially the partial differential equation describing the time evolution of the plasma distribution function to describe the statistical ensemble. To describe the macroscopic effects of the specific distribution function one can calculate the momenta of the Boltzmann-Vlasov equation and arrive at the key equations of magnetohydrodynamics. The zeroth moment of the Boltzmann-Vlasov equation, the continuity equation, yields

$$\frac{\partial \rho}{\partial t} + (\rho u^{\mu})_{;\mu} = 0, \tag{1.6}$$

where ρ corresponds to the density, u^{μ} to the four-velocity. Consequently, we write for the for the first moment of the Boltzmann-Vlasov equation, the Euler equation, following relation

$$\frac{\partial u^{\mu}}{\partial t} + u^{\nu} u^{\mu}{}_{;\nu} = -\frac{1}{\rho} P_{;}{}^{\mu} - \Phi_{;}{}^{\mu} + \frac{1}{\rho} \Pi^{\mu\nu}{}_{;\nu} \tag{1.7}$$

The covariant derivatives of scalar fields ρP and Φ correspond to the pressure $P_{,}{}^{\mu}$ and potential gradient $\Phi_{,}{}^{\mu}$, respectively. The $\Pi^{\mu\nu}$ is the stress tensor.

The equations in the subsequent subsections correspond to those listed, e.g., in the textbook Frank et al. (2002), unless stated otherwise.

1.2.1 Spherically symmetric accretion

Let us introduce the elements of the idea of spherically symmetric steady accretion onto a central body of mass M (Bondi, 1952; Zeldovich and Novikov, 1971). First we have to account for the spherical symmetry and that is by setting the coordinate system (r, θ, φ). To account for the steady solution we simply set the $\frac{\partial}{\partial t} = 0$. Under these circumstances the general form of continuity equation (1.6) then translates to

$$\frac{1}{r^2} \frac{\mathrm{d}}{\mathrm{d}r} (r^2 \rho v) = 0. \tag{1.8}$$

By integration we then obtain

$$4\pi r^2 \rho(-v) = \dot{M}. \tag{1.9}$$

The accretion rate $\dot{M}$ is radial function, and it is proportional to the $\rho(-v)$, with the minus sign caused by the infalling motion of the material.

We treat the general form of the Euler equation (1.7) similarly, setting the spherical symmetry and dropping the partial time derivatives. Hence we arrive at

$$v\frac{\mathrm{d}v}{\mathrm{d}r}+\frac{1}{\rho}\frac{\mathrm{d}P}{\mathrm{d}r}+\frac{\mathrm{d}\Phi}{\mathrm{d}r}=0. \tag{1.10}$$

The polytropic equation of state dictates $P = K\rho^{\gamma}$, $K = const$ allows us to study the system setup for the various choices of γ parameter, e.g. $\gamma = 5/3$ in case of adiabatic equation of state. The potential Φ is set to $-GM/r$, and we also neglect the presence of the stress tensor $\Pi^{\mu\nu}$. Hence, the Euler equation takes the following form

$$v\frac{\mathrm{d}v}{\mathrm{d}r}+\frac{c_{\mathrm{s}}^2}{vr^2}\frac{\mathrm{d}v}{\mathrm{d}r}+\frac{GM}{r^2}=0. \tag{1.11}$$

The spherical symmetry is invariant to the change of both angles θ, φ and the eq. (1.8) and (1.10) are essentially 1-dimensional differential equations. Rearranging the terms we get

$$\frac{1}{2}\left(1-\frac{c_{\mathrm{s}}^2}{v^2}\right)\frac{\mathrm{d}}{\mathrm{d}r}(v^2)=-\frac{GM}{r^2}\left[1-\left(\frac{2c_{\mathrm{s}}^2r}{GM}\right)\right]. \tag{1.12}$$

This differential equation is the “Bondi equation”: it represents the result of the steady spherical symmetric approximation of the classical equations due to Bondi (1952). We notice the right hand side of this equation can be set to 0, when the radius r is set to $r_{\mathrm{s}} = GM/(2c_{\mathrm{s}}^2)$, i.e. critical/sonic point. In general there are 6 classes of solutions based on the behavior when crossing the r_{s} (see e.g. Frank et al., 2002). The eq. (1.12) also hides the Parker stellar wind model solution in the steady spherical symmetric approximation.

Let us attempt to formulate the solution pertaining the accretion solution class and integrate the eq. (1.10)

$$\frac{v^2}{2}+\int\frac{\mathrm{d}P}{\rho}-\frac{GM}{r}=const \tag{1.13}$$

while we substitute $\mathrm{d}P = K\gamma\rho^{\gamma-1}\mathrm{d}\rho$, and integrate we follow with $\gamma P/\rho = c_{\mathrm{s}}^2$ and obtain the Bernouli integral

$$\frac{v^2}{2}+\frac{c_{\mathrm{s}}^2}{\gamma-1}-\frac{GM}{r}=const. \tag{1.14}$$

After a few subsequent adjustments we can express the speed of sound and density with respect to the infinity as

$$c_{\mathrm{s}}(r_{\mathrm{s}})=c_{\mathrm{s}}(\infty)\left(\frac{2}{5-3\gamma}\right)^{\frac{1}{2}} \tag{1.15}$$

and consequently

$$\rho(r_{\mathrm{s}})=\rho(\infty)\left[\frac{c_s(r_{\mathrm{s}})}{c_{\mathrm{s}}(\infty)}\right]^{2/(\gamma-1)}. \tag{1.16}$$

Finally, we write for the accretion rate the following

$$\dot{M}\cong 1.4\times10^{11}\left(\frac{M}{M_\odot}\right)^2\left[\frac{\rho(\infty)}{10^{-24}}\right]\left[\frac{c_{\mathrm{s}}(\infty)}{10km\,s^{-1}}\right]^3 g\,s^{-1} \tag{1.17}$$

The formula points out the expected level of the accretion rate to be rather low, given the conditions of the material placed at the infinity. It also identifies the radius of the influence of the accreting source as the critical/sonic point. That is the threshold value below which the material velocity turns supersonic (for a lucid exposition of elementary properties of transonic flows onto black holes, see Chakrabarti, 1990). The switch to the supersonic speed once crossing the critical/sonic point indicates there is a necessity to use different approach to account for the final interaction of the accreted material and the accretor, i.e. implement the plasma physics approach.

1.2.2 Axially symmetric disc accretion

In order to reflect the baseline axial geometry, hereafter we will adopt the axial coordinates (R, φ, z) and proceed with the introduction of key equations for the structure of the accretions disc and focus on the effects of the radiation in the standard Shakura-Sunyaev thin accretion disc scenario (Frank et al., 2002).

To illustrate the simple version of a mechanism behind the accretion we start with a simple accretion disc and focus on two streams located at R and $R+\Delta R$. Particles rotating in the accretion disc at the radius R interchange their position with the particles orbiting at the distance $R+\Delta R$, et vice versa. This simulates the viscous process taking place in the accretion disc across its radial layers (see Figure 1.3). We define the angular momenta of both particles as

$$\begin{aligned} l_{\text{inner}} &= R^2\Omega(R), \\ l_{\text{outer}} &= (R+\Delta R)^2\Omega(R+\Delta R). \end{aligned} \tag{1.18}$$

Their respective angular momenta change as their distances from the centre change $R \leftrightarrow (R+\Delta R)$ as follows

$$\begin{aligned} l_{\text{inner}} &= (R+\Delta)R\Omega(R), \\ l_{\text{outer}} &= R(R+\Delta)\Omega(R+\Delta R). \end{aligned} \tag{1.19}$$

We define the the difference between the outer and inner layer after interchanging the particles' position as

$$\Delta l = l_{\text{outer}} - l_{\text{inner}} = R(R+\Delta R)(\Omega(R+\Delta R) - \Omega(R)). \tag{1.20}$$

Multiplying the eq. (1.20) by the length of the accretion ring at R and the assuming its surface density profile Σ, we define the gravitational torque $G(R)$, which is proportional to kinematic viscosity ν, as

$$G(R) = 2\pi R\Sigma\nu R^2\Omega'(R), \tag{1.21}$$

while neglecting the $o(\Delta^2)$ terms. We record the Ω profile's profound effect as it prescribes the flow of angular momentum in the accretion disc. In case of Keplerian disc, with the $\Omega'(R) < 0$, we notice the angular momentum is being transferred to the outer layers of the accretion disc.

Adopting the Newtonian approximation, using the axial coordinates, let us rewrite the continuity equation (1.6) as

$$R\frac{\partial \rho}{\partial t} + \frac{\partial}{\partial R}(\rho v_R R) = 0. \tag{1.22}$$

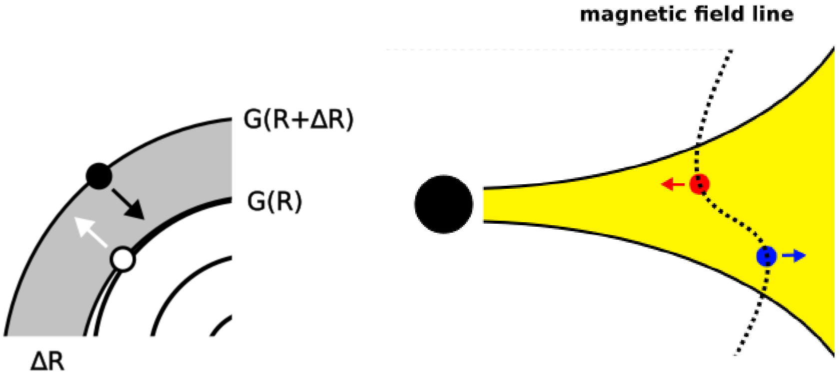

Figure 1.3: *Left panel:* The sketch of accretion disc's material layers (marked by grey color) illustrating the viscous processes in the top view. The interchanging of the material from inner and outer layer (marked by the white and black point particles, respectively) causes the angular momentum to be transported outwards, whereas the material is spiralling down onto the central object. However, this type of viscosity appears to be far too low in astrophysically realistic conditions of accretion discs (Frank et al., 2002). *Right panel:* Edge on view of the accretion disc immersed in the non-zero poloidal magnetic field causing the shift of the point particles (marked by red and blue color) between the layers of the accretion disc (marked by yellow color), a direct result of the magnetorotational instability. The latter mechanism is considered to be the origin of effective viscosity that drives accretion (Balbus and Hawley, 1991).

We further rewrite the Euler equation (1.7), describing the angular momentum conservation, in the following form

$$R^3\frac{\partial(\rho v_\varphi)}{\partial t}+\frac{\partial}{\partial R}(R^3 v_R v_\varphi \rho)=\frac{\partial}{\partial R}\left(R^3\nu\rho\frac{\partial\Omega}{\partial R}\right). \tag{1.23}$$

In both equations we denote the density still as ρ, both the radial and azimuthal components of the velocity as v_R and v_φ, kinematic viscosity as ν and the angular velocity as Ω.

It is convenient to transform, both the continuity equation and angular momentum conservation equation, by vertically integrating the density ρ as $\int_0^h \rho\,\mathrm{d}z=\Sigma$, with accretion surface density denoted as Σ. By doing so we rewrite the eq. (1.22) to

$$R\frac{\partial\Sigma}{\partial t}+\frac{\partial}{\partial R}(\Sigma v_R R)=0. \tag{1.24}$$

Following the same steps we vertically integrate the Euler eq. (1.23) and arrive at

$$R^3\frac{\partial(\Sigma v_\varphi)}{\partial t}+\frac{\partial}{\partial R}(R^3 v_R v_\varphi \Sigma)=\frac{\partial}{\partial R}\left(R^3\nu\Sigma\frac{\partial\Omega}{\partial R}\right). \tag{1.25}$$

The latter eq. (1.25) can be rewritten as

$$R^3\frac{\partial(\Sigma v_\varphi)}{\partial t}+\frac{\partial}{\partial R}(R^3 v_R v_\varphi \Sigma)=\frac{1}{2\pi}\frac{\partial G(R)}{\partial R}. \tag{1.26}$$

The $G(R)$ is a R-dependent quantity called gravitational torque, describing the transfer of angular momentum across the accretion disc (from inside out) and is written (in a bit different way than the eq. (1.21)) as

$$G(R) = 2\pi R^3 \nu \Sigma \frac{\partial \Omega}{\partial R}. \tag{1.27}$$

Combining the two eq. (1.24) and(1.25) we can write the surface density evolution equation of the accretion disc as

$$\frac{\partial \Sigma}{\partial t} = \frac{3}{R}\frac{\partial}{\partial R}\left[\sqrt{R}\frac{\partial}{\partial R}(R\nu\Sigma)\right]. \tag{1.28}$$

This partial differential equation resembles the heat equation and similarly as one describes the diffusion-like process. However, this eq. describes the mass flow across the accretion disc its point of origin (see Figure 1.4). For the systems involving the Kerr black hole, the equation describing surface density (1.28 of the accretion disc gets more complex (see e.g. Balbus and Mummery, 2018), nevertheless, still keeps the heat-equation-like form.

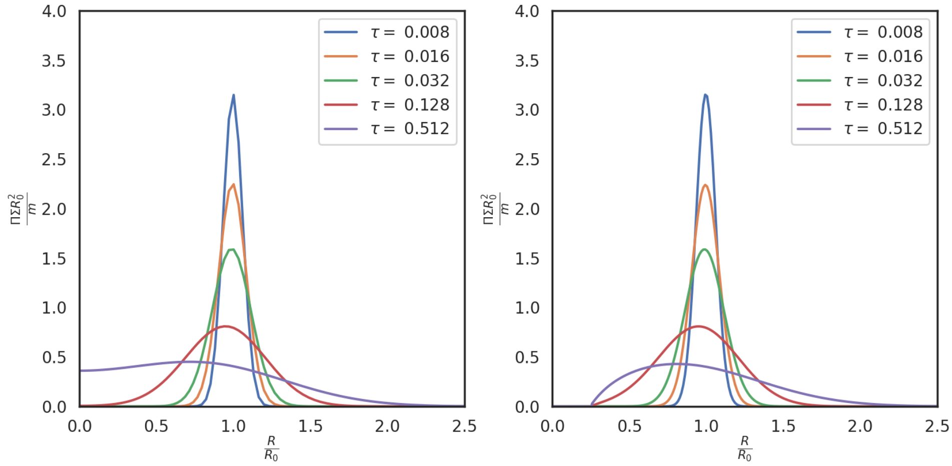

Figure 1.4: Temporal evolution of an accretion ring surface density treated as a solution of diffusion-type equation (1.28). *Left panel*: A numerical solution to eq. (1.28), given the boundary condition $\Sigma(R_{\text{inner}} = 0, t) = \Sigma(R_{\text{outer}}, t) = 0$. *Right panel*: As in the left panel but for the boundary condition $\Sigma(R_{\text{inner}} = 6R_{\text{g}}, t) = \Sigma(R_{\text{outer}}, t) = 0$ (adapted from Štolc and Karas (2019)).

Now to describe the dynamics of the accretion disc's material we expect it to rotate around the central body with angular velocity Ω. The usual choice is for the accretion disc to be rotating with the angular velocity following the Keplerian angular velocity profile, i.e.

$$\Omega(R) = \Omega_{\text{K}}(R) = \sqrt{\frac{GM}{R^3}}. \tag{1.29}$$

Consequently the Keplerian angular velocity profile is corresponding to the azimuthal component of velocity and taking form of Keplerian velocity

$$v_{\varphi}(R) = R\Omega(R) = R\Omega_{\text{K}}(R) = \sqrt{\frac{GM}{R}}. \tag{1.30}$$

If we assume $\frac{\partial}{\partial t} = 0$, the continuity eq. (1.24) yields

$$\Sigma v_R R = constant. \tag{1.31}$$

The relation holds at any point in the radial direction across the accretion disc and we define the accretion rate as

$$\dot{M} = 2\pi\Sigma(-v_R)R, \tag{1.32}$$

where v_R is is negative, hence the minus sign.
Again, setting $\frac{\partial}{\partial t} = 0$ in the angular momentum eq. (1.25) we arrive to the following relation

$$\frac{\partial}{\partial R}(R^3 v_R v_\varphi \Sigma) = \frac{1}{2\pi}\frac{\partial G(R)}{\partial R} \tag{1.33}$$

We now make use of the latter eq. as well as the gravitation torque formula (1.27) and the eq. (1.32) and we get

$$\nu\Sigma = \frac{\dot{M}}{3\pi}\left[1 - \sqrt{\frac{R_{\mathrm{inner}}}{R}}\right]. \tag{1.34}$$

The eq. (1.34) defines the dissipation rate and helps to eliminate the kinematic viscosity ν from the following formula:

$$D(R) = \frac{3GM\dot{M}}{8\pi R^3}\left[1 - \sqrt{\frac{R_{\mathrm{inner}}}{R}}\right]. \tag{1.35}$$

We further define the luminosity in the region between two radii R_1 and R_2 as follows

$$L(R_1, R_2) = 2\int_{R_1}^{R_2} 2\pi R\, D(R)\, \mathrm{d}R. \tag{1.36}$$

Plugging the the dissipation rate formula from eq. (1.35) into the eq. (1.36) and setting the R_{inner} into R_1 and $R_2 \to \infty$, one gets

$$L_{\mathrm{disc}} = \frac{GM\dot{M}}{2R_{\mathrm{inner}}} = \tfrac{1}{2}L_{\mathrm{acc}}. \tag{1.37}$$

Since the accretion disc is supposed to be thin, i.e. $z \ll R$, the z-component of the Euler equation (1.7) is reduced to hydrostatic equilibrium and allows to define the accretion disc's scaleheight as

$$H(R) = c_{\mathrm{s}}\sqrt{\frac{R}{GM}}R. \tag{1.38}$$

Now assuming the accretion disc scale height to radius ratio $H/R \ll 1$ the Keplerian velocity is supposed to be supersonic, i.e.

$$c_{\mathrm{s}}(R) \ll \sqrt{\frac{GM}{R}} = R\Omega_{\mathrm{K}}. \tag{1.39}$$

1.2.3 Time-scales of accretion

Shakura and Sunyaev (1973a) introduced the kinematic viscosity operating in a geometrically thin accretion disc to address the intermolecular interactions of the rotating material

$$\nu = \alpha c_{\mathrm{s}} H, \tag{1.40}$$

with α being a phenomenological parameter. In this way, viscosity is parametrized to provide an applicable solution to the real astrophysical problems in the context of standard accretion disc theory. To be consistent with the underlying assumptions, the thin disc scenario allows for the accretion flow with a prescribed value of $\alpha < 1$.

The dynamical timescale describes the accretion disc debris azimuthal motion

$$t_{\text{dynamical}} \sim \frac{R}{v_\varphi}. \tag{1.41}$$

Following the standard thin disc assumption $v_\varphi \gg v_R \gg v_z$, it expected to be short. The hydrodynamical timescale is used to describe the vertical motion of the gas across the accretion disc

$$t_{\text{hydrodynamical}} \sim \frac{H}{c_{\mathrm{s}}} \sim \frac{R}{v_\varphi} \sim t_{\text{dynamical}} \tag{1.42}$$

and as is proportional to the dynamical one. We have arrived to the result, given the additional assumption (see eq. (1.38))

$$H \sim \frac{c_{\mathrm{s}}}{v_\varphi} R. \tag{1.43}$$

We define the timescale for the variability of the disc in the radial direction as follows

$$t_{\text{viscous}} \sim \frac{R^2}{\nu} \sim \frac{1}{\alpha} \frac{R v_\varphi}{H c_{\mathrm{s}}} \frac{R}{v_\varphi} \sim \frac{1}{\alpha} \frac{v_\varphi^2}{c_{\mathrm{s}}^2} t_{\text{dynamical}} \sim \frac{1}{\alpha} \frac{v_\varphi^2}{c_{\mathrm{s}}^2} t_{\text{hydrodynamical}}. \tag{1.44}$$

We further input the kinematic viscosity as see eq. (1.40). Rearranging the terms in eq. (1.44) and keeping in mind the result from eq. (1.42) and (1.43), we deduce the relation between the viscous timescale and the latter two timescales.
The thermal timescale relates to the temperature re-adjustment period necessary to balance out the the energy dissipation in the accretion disc (see eq. 1.35). Now summarizing the results from eq. (1.42) and (1.44) we write the thermal timescale as follows

$$t_{\text{thermal}} \sim \frac{c_{\mathrm{s}}^2}{v_\varphi^2} t_{\text{viscous}} \sim \frac{1}{\alpha} t_{\text{dynamical}} \sim \frac{1}{\alpha} t_{\text{hydrodynamical}}. \tag{1.45}$$

Given the α-prescription for the accretion disc in the standard scenario is $\alpha \lesssim 1$ we write order the most crucial timescales of the accretion disc in the ascending order as

$$t_{\text{dynamical}} \sim t_{\text{hydrodynamical}} \lesssim t_{\text{thermal}} \ll t_{\text{viscous}}. \tag{1.46}$$

Let us note that the characteristic timescale on which a standard accretion disc is expected to vary, i.e., the order of viscous timescale of the outer disc regions, appears to be orders of magnitude longer than the actually observed rapid variability timescales. In another words, the short- timescale, large-amplitude variability poses a problem for the standard disc scenario. Lawrence (2018) and other authors conclude that the role of strong reprocessing and obscuration may operate, along with non-local phenomena (e.g., spiral waves or extended gaps; Karas et al., 2001, and further references cited therein) to resolve these long-standing issues.

1.3 Radiation mechanisms

The astrophysical sources are effectively accessible through the observations. The electromagnetic radiation can tells us physical properties of the source but also help to decipher the conditions for the radiation to be produced as well as the past and future evolution of the radiation source. The mechanisms behind the emission of the electromagnetic radiation depend on various conditions and so does its respective energy band. The following subsections contemplate the most notorious mechanisms behind the radiation coming not only from the central engines of the galactic core but also their surrounding area.

The equations and the notation adopted in our brief outline correspond to the ideas described in the classical monographs by Frank et al. (2002), Kato et al. (2008) and (Meier, 2012).

1.3.1 Thermal emission

We require the accretion disc to be optically thick in vertical (z) direction. By doing so, one can assume the whole accretion disc area to radiate as a black body. The total heat radiated by the blackbody is proportional to the fourth power of temperature. In case of accretion discs the total radiant emission is equal to its dissipation rate (see eq. (1.35)). In that sense we reformulate the Stefan-Boltzmann law as follows

$$\sigma T(R)^4 = D(R), \tag{1.47}$$

where σ is Stephan-Boltzmann constant. The temperature profile of an accretion disc is $R-$dependent and reads as

$$T(R) = \left\{ \frac{3GM\dot{M}}{8\pi R^3 \sigma} \left[1 - \sqrt{\frac{R_{\text{inner}}}{R}} \right] \right\}^{\frac{1}{4}}. \tag{1.48}$$

Further, we write Planck's law as

$$I_\nu = B_\nu[T(R)] = \frac{2h\nu^3}{c^2(e^{h\nu/kT(R)} - 1)}. \tag{1.49}$$

Utilizing the Planck's law (1.49) and inserting the temperature profile of the accretion disc (1.48) we write the formula for the specific flux observed by at the

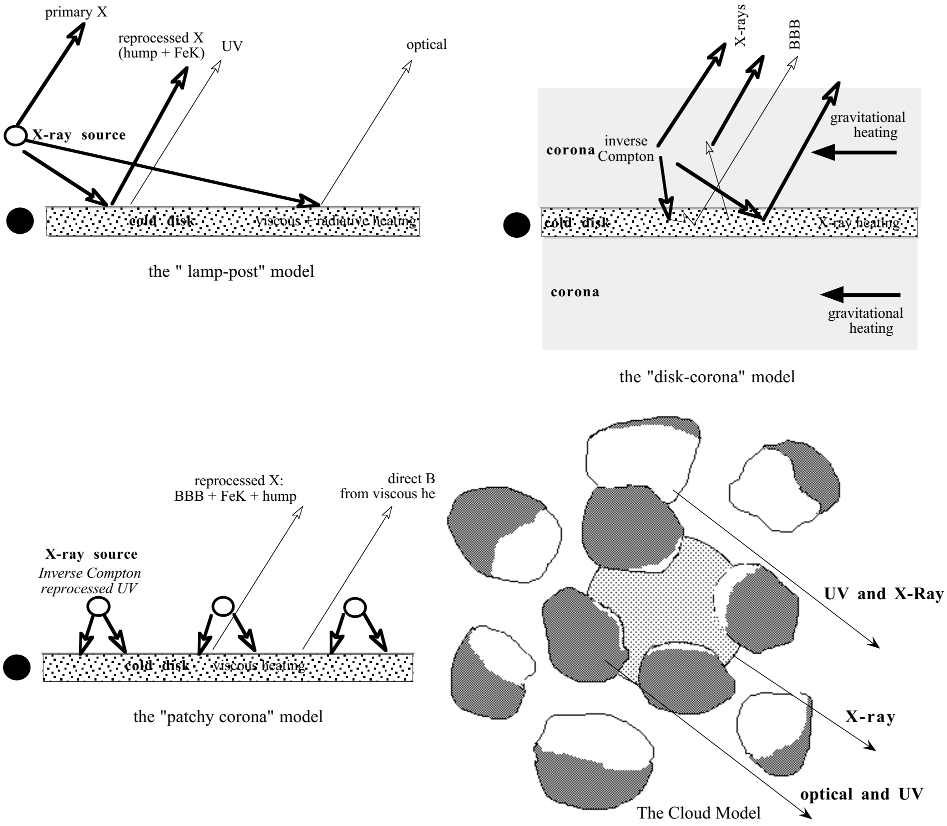

Figure 1.5: Four fiducial geometries have been proposed to explain the origin and properties of UV and X-ray emission from accreting SMBHs. Proceeding from the top-left panel to bottom-right panel, the lamp-post scenario is the frequent simplification to account for the basic properties of an irradiated, cold, equatorial accretion disc. More elaborated schemes consider different variants of the coronal location and size above the disc plane or off-equatorial cloud distribution that adds Comptonization as an important factor contributing to the line formation (Karas et al., 2000). As explained further in the text, our present work considers several versions of the lamp-post scheme combined with the central spherical corona and an equatorial gap caused by a secondary orbiter (Štolc et al., 2023). Image credit: Collin et al. (2001).

distance D, with inclination i as

$$\nu F_\nu = \frac{4\pi h \cos i\, \nu^4}{c^2 D^2} \int_{R_\mathrm{inner}}^{R_\mathrm{outer}} \frac{R\,\mathrm{d}R}{\left(e^{h\nu/kT(R)} - 1\right)}. \tag{1.50}$$

It is convenient to multiply the specific flux (1.50) by $4\pi D^2$ and eliminate the observer's distance. The respective specific luminosity of the accretion disc then yields

$$\nu L_\nu = \frac{16\pi^2 h \cos i\, \nu^4}{c^2} \int_{R_\mathrm{inner}}^{R_\mathrm{outer}} \frac{R\,\mathrm{d}R}{\left(e^{h\nu/kT(R)} - 1\right)}, \tag{1.51}$$

We thus arrive at the formula for the specific luminosity of the source regardless of its distance by integrating the individual contribution of the infinitesimal rings that the accretion disc is split into (see Figure 1.6). We notice the kinematic viscosity does not prevail in the eq. (1.51) as it is a result of both, the steady condition and blackbody assumption. Nevertheless, this approximation allows to illustrate the optical and UV spectral features based on the accretor properties and the surrounding accretion disc.

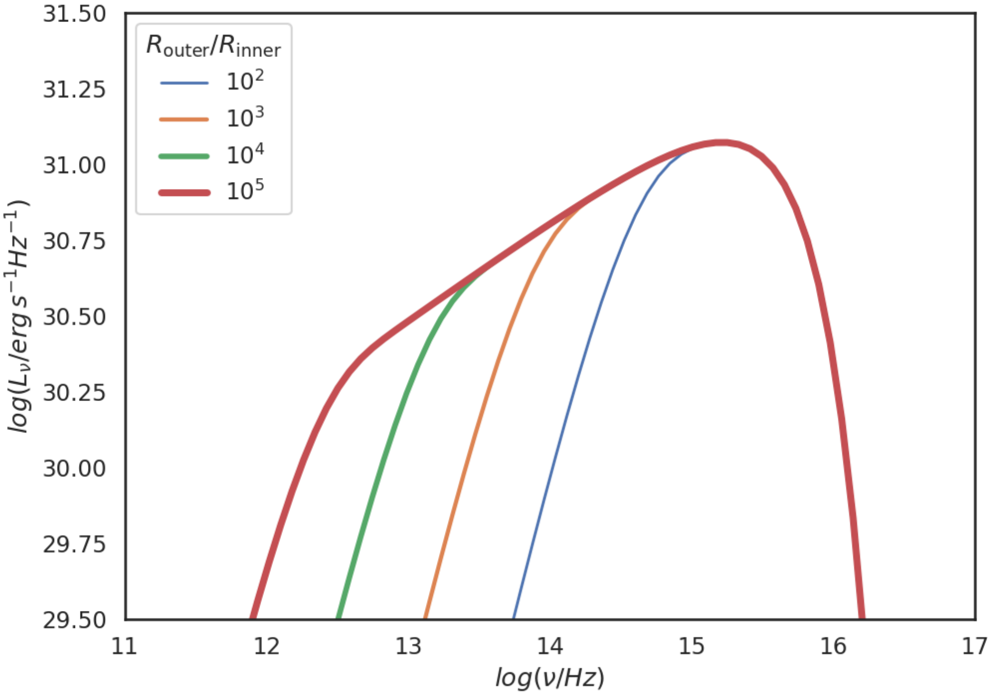

Figure 1.6: The illustration of continuum luminosity profile of the thermal component from an accretion disc. The accretion disc is parametrized by the ratio $R_{\rm outer}/R_{\rm inner}$ corresponding to 10^2, 10^3, 10^4 and 10^5, whereas the $R_{\rm inner}$ is fixed to $6R_{\rm g}$ ($R_{\rm ISCO}$ for the Schwarzschild black hole; and with the mass $10^9 M_\odot$). The plot shows the size of the disc plays a crucial role in the shape of the thermal component profile. A more detailed study can be found in Frank et al. (2002).

1.3.2 Additional major radiation processes

However, the AGNs are not strictly limited to the thermal radiation. Both, the inner and the outer region of the galactic centre and the processes taking place exhibit the spectral features spanning across all energy bands (e.g. see the scenarios and the corresponding systems' geometries for the UV and X-ray emission in Figure 1.5). The major radiation mechanisms, having typically effect on shape and properties of the the high energy spectra, are as follows (e.g. Rossi and Olbert, 1970):

- *Bremsstrahlung emission*, a.k.a. the "braking radiation" is essentially caused by the radiation output of an electron as it gets deflected by an ion (or a slab of ions), along its path. The free electron deflection takes place due to the electromagnetic interaction of charged particles. Depending on the velocity distribution of the scattered/deflected particles, Maxwellian, or power law (relativistic velocities) the Bremsstrahlung is either labeled as thermal or non-thermal, respectively. The Bremsstrahlung is a result of free-free type of interaction, where the electrons are free before and after the interaction takes place.

- *Synchrotron emission* occurs when relativistic charged particles travel along circular-like trajectories in the magnetic field, i.e. the velocity of the moving particle has to be perpendicular to the acceleration. The generalization to helical trajectories depend on the specific structure of the magnetic properties. The charged particles with velocities proportional to their rest mass emit so called cyclotron radiation. In the relativistic regime, the charged particles rotate around the central black hole with the velocity close to the speed of light and each particle creates a beam of light corresponding to a conical structure. Typically, the spectra of the accretion disc have an imprint of the synchrotron radiation.

- The *inverse Compton effect* is based on the Compton scattering. However, whereas during the Compton scattering a photon loses fraction of its energy in favour of the electron, in case of the inverted process the photon is the one gaining the energy from the electron. The minimal requirements for this process are low energy photon and the high-energetic free electrons with the relativistic velocities close to the speed of light. In real astrophysical scenarios, this strictly relativistic phenomenon takes place as the low energy thermal photons of the accretion source are expected to be powered up by the electrons forming the surrounding coronal structure of the system.

- *Emission/absorption lines* are indicators of spontaneous or induced state shifts from excited energy states to the lower states and vice versa. The strength of the lines vary depending on the way they originated. Specifically, in context of the emission lines, the Fe Kα line is the most noticeable and it is located in the X-ray band. Its origin is triggered by the excitation of cold slab of accretion disc material by the high-energetic coronal radiation. The subsequent reflection component corresponding to the de-excitation of the atoms, mostly iron, accounts for the emission at $6.4keV$. The study of general relativistic regime on this particular spectral line properties offers a way to constrict the parameters of the galactic centre, such as mass, inclination or spin of the central black hole.

1.4 Evidence for accreting black holes from the electromagnetic domain

SMBHs are thought to reside at the centres of many galactic nuclei, where they act as “engines” providing the energy to outflowing gas and collimating the jets (Soltan, 1982; Magorrian et al., 1998; Richstone et al., 1998). The analytical solutions to the Einstein’s field equations (1.1) differ based on the central body properties. During the phase of collapse the central body "radiates" away the effects of its parameters, as stated by the No-hair theorem. The charged Reissner-Nordström solution to the Einstein's equations does not prove to be astrophysically relevant (see e.g. Wald, 1972; Zajaček et al., 2018) compared to the effect of the spin in the Kerr (rotating) or Kerr-Newman (rotating and electrically charged) solution. Nevertheless there is a plethora of effects that allow the black holes to be observable, even though indirectly.

Gamma Ray Bursts (GRBs), first observed by Klebesadel et al. (1973), belong to the most dominant effects on the sky. The sudden brightening spans across the whole frequency band, i.e. from radio waves to X-ray. GRBs are attributed to the late stages of stellar evolution leading to either supernova, neutron star or black hole formation, or possible their merger. They last up to hundreds of seconds (Kouveliotou et al., 1993) with a distinguished $2s$ threshold between short and long GRBs.

The astrophysical phenomena on par with the GRBs' energetic output are relativistic jets. These collimated streams of relativistic (Lorentz factor $\Gamma \sim$ a few orders of 10) and ultrarelativistic (Lorentz factor $\Gamma \gtrsim 100$) particles are emitted presumably along the axis of the rotation of the central black hole or neutron star (see e.g. McKinney, 2006, and references therein). Even though the exact mechanism behind the relativistic jets is still unknown it is widely believed the essence of the effect lies withing the extraction of rotational energy from rotating black hole by either Penrose or Blandford-Znajek processes, respectively (Penrose and Floyd, 1971; Blandford and Znajek, 1977); see also (Punsly, 2001).

Once a cold slab of the orbiting material in the accretion disc is immersed in highly energetic corona, one can expect it to develop a partially ionized skin or even become fully ionized. De-excitation then leads to the presence of spectral features, where Fe Kα is particularly prominent in the observed spectra. Various models have been devised to study the effect of broadening and skewness of the spectral lines (Fabian et al., 1989; Kojima, 1991; Laor, 1991) before the actual very first observation took place at 1995 by Tanaka et al. (1995). The advanced methods of data fitting allow us to determine the parameters of the black hole, namely, mass and spin under the conditions of the strong gravity regime (Dovčiak et al., 2004; Reynolds, 2021). Nevertheless, the first interferometric images of SMBH vicinity were analyzed and published via the joined team effort of Event Horizon Telescope (EHT) for M87 galaxy (in 2019 and 2022) and Sagittarius A* (in 2022), respectively (Event Horizon Telescope Collaboration, et al., 2019b, 2022). The glowing disc-like structure clearly points out the accretion disc is rotating around a SMBH located at its centre (see Figure 1.2).

Stars travelling can due to the stochastic perturbations in their motion end up in the galactic centre being bound to the central SMBH. The passage through the point of closest approach to the black hole can be lethal for the star as once it reached the tidal radius, the gravitational pull of the central body become stronger than the star self-gravity (Hills, 1975; Luminet and Marck, 1985; Rees, 1988). Hence it becomes stretched and is tidally disrupted. Tidal disruption events (TDEs) can cause sudden rebrightening in the otherwise quiescent galaxies (see e.g. Komossa, 2015, and references therein). They can also be connected to the sudden downward changes in their activity, as material depletion of the inner region of the accretion disc due to the possible tidal radius (Ricci et al., 2020). Tidal disruption does not exclusively concern the stars but basically any celestial object reaching tidal radius, e.g. dust enshrouded objects such as G2 (Zajaček et al., 2014).

Rapid stellar movements in the central region of the Milky Way also help to uncovered the presence of the SMBH Sagittarius A* (Eckart and Genzel, 1996; Genzel et al., 1997; Ghez et al., 1998). The detailed orbital analysis of these stellar objects, called S-stars, is probing the effects of the general relativity as these stars have the SMBH located at its periapsis as well as helps to constrain its parameters, such as its mass and the distance (e.g Parsa et al., 2017).

Galactic mergers represent a special grade of observable events of two or multiple merging black holes located at their centre (e.g. Volonteri et al., 2003). They are violent interactions driven mainly by the gravity and can be distinguished differently. The two recoiling SMBHs are prone to generate gravitational waves, effects of which can be estimated within the linearized version of GR and properly computed numerically, and can be detected via laser-based detectors (Gertsenshtein, 1961), namely, LIGO and Virgo ground-based interferometers (Abadie et al., 2012). Complementary, these events also significantly influence the spectral features such as optical and UV and manifest themselves as dips clearly visible in the electromagnetic spectra (e.g. Gültekin and Miller, 2012; Štolc et al., 2023). Final stages of the recoiling SMBHs can be also attributed to the changes in the signal from TDEs, which are seen as periodical drops in the luminosity (e.g. Liu et al., 2014). Finally, once merged the newborn galaxies often serve as a fruitful testbed for the observations focusing on the star-forming/star-burst regions (e.g. de Grijs and González Delgado, 2005).

Generally, mass is the key parameter of cosmic black holes. It is assumed to be positive, nevertheless, within General Relativity the value of the mass is not constrained *a priori* from the theory. It appears that two families of black holes have developed during the cosmic evolution (Karas and Matt, 2007; Sicilia et al., 2022): (i) stellar-mass black holes which originate by gravitational collapse of evolved stars (Mirabel, 2017), and (ii) SMBHs that are typically found in cores of galaxies with mass in the range $\sim 10^5$–$10^{10} M_\odot$ (Volonteri et al., 2021). Black holes are thought to grow by gradual accretion, merging, or direct infall of the cosmic material; it appears that the history of the black hole is then reflected in its spin evolution, which is constrained by the theoretical arguments between zero (non-rotating) and extreme (maximally co-rotating or counter-rotating) values. Long-standing speculations have been emerging with respect to the possibility of low-massive (primordial) black holes below the minimum mass for stellar collapse, and IMBHs of about $\sim 10^2$–$10^5 M_\odot$ (Greene et al., 2020).

Albeit not directly observed, the black holes influence not only the structure of the inner region of the galactic centre but also the spectral features of radiation in all energy bands. The spectral properties such as polarization of the radiation help to infer the parameters of the inner regions of the black hole; to study the effects Lense-Thirring precession; with the help of reverberation mapping, studying the time lag of the observed radiation, one can also infer the inner regions parameters, etc.

2. Accretion discs with gaps

2.1 Gap formation

A secondary body, a star or a compact object, orbiting around the supermassive dark mass and embedded within an accretion disc plane proceeds in a gaseous and dusty resistive environment over its entire trajectory. The environment of is gradually accreted and redistributed. In this way a gap in the disc flow may be opened. It depends on parameters of specific system whether the perturber is able to open a permanent gap or, on the contrary, if the gap closes in time shorter then orbital period of the secondary body. Syer et al. (1991) estimated the parameters that govern the stellar motion inside a thin accretion disc. They adopt the standard thin accretion disc scheme with the Newtonian potential of the central body, and they look for conditions to open a gap in the disc. Indeed, the occurrence of the gap depends, besides other parameters, on the ratio of the gap width to the geometrical vertical height of the disc flow. The gap can persist if the width of the gap exceeds the thickness, thus depending on the viscosity (α-parameter).

Due to stochastic perturbations in the stellar motions the stars can end up being gravitationally bound to the central object. The initial parameters of the star are the trajectory type, i.e. the eccentricity, the argument of the pericentre and the inclination with respect to the central black hole orbital plane (see the system sketch in Figure 2.1). In this simple scenario the SMBH is surrounded by the accretion disc. A gravitationally bound (giant) star or an (intermediate-mass) black hole is thus positioned on an elliptical orbit and is inevitably intersecting the accretion disc twice per revolution. These repetitive passages, complemented by the accretion disc's drag and the central supermassive body gravitational pull cause the initial values of the orbital elements to evolve (Šubr and Karas, 1999). The inclination of the star will gradually approach zero (i.e. aligned with the disc plane), while the trajectory becomes circularized at the grinding radius. An interesting analogy has been explored in the context of proto-planet–disc interaction in highly inclined extra-solar systems (Rein, 2012). Once in the orbital plane of the central object the fate of the perturber is governed by the ratio of its radius of influence versus the accretion disc scale-height. From this point the orbiter gradually loses the angular momentum and spirals down to the central object. The mechanisms of energy loss can be realized via density waves, gap formation, or gravitational waves emission (e.g. Artymowicz, 1994; Karas and Šubr, 2001). These can be estimated computationally and eventually detected as changes in the observed spectra in the different electromagnetic energy bands.

As the star loses its angular momentum and closes in on the central body there is a possibility it will get tidally disrupted when reaching the terminal distance corresponding to tidal radius. One can study the effects of tidal disruptions (or partial tidal disruptions) on the star specifically in the X-ray domain (Guolo et al., 2024). Nevertheless, the tidal disruption of the star that is spiralling down to the central body, prevents us to see its effects on the the star might be tidally disrupted and can therefore not reach closer distance to the central body. Also the gap width created by the start may or may not have an effect in the optical/UV spectra because of its insignificant size.

It is thus tempting to adopt an alternative mechanism of gap creation. For starters, one replaces the stellar body by a more massive objects that eventually form gaps of adequate size. We therefore propose the perturber to be a secondary black hole, that was brought to the orbital plane of the primary in the similar mechanism as stated above and depicted in Figure 2.1. The standard effects in the spectral energy distribution (SED) will then be altered accordingly (e.g. Gültekin and Miller, 2012; Štolc et al., 2023).

However, the presence of the secondary body is not an exclusive way to change the spectral features of the observed source. In cases of small relative accretion rate the effect of advection can become a dominant regulation mechanism of the accretion disc. Located precisely in the inner regions of the accretion disc this can be interchangeable with the presence of a perturber. The inner region structure and therefore spectral feature changes can be a direct result of tidal disruption as well. Observations and the respective models show a sudden change in the coronal radiation that is suspected to be caused by the depletion of the inner region of the accretion disc starting from the tidal radius downwards (Ricci et al., 2020).

In our study we focus on the SED and its specific profiles assuming different perturbers in the system, namely:

- advection component, i.e. the inner region filled with hot plasma that changes the optical thickness;
- secondary component, a SMBH, expected to have favoured effects leading to the gap formation;
- combination of both components.

On our way to study the proposed scenarios we also introduce a possible fourth option when introducing the dust component in the system. The dust component that has ultimately the effect of intrinsic reddening in the spectra will be further discussed in the upcoming subsections as well.

The presence of the perturbers in the context of the SED has to be incorporated in the eq. (1.51. Hence we write for the luminosity following

$$\nu L_\nu(\nu) = \frac{16\pi^2 h\nu^4 \cos i}{f_{\mathrm{col}}^4 c^2} \left(\int_{R_{\mathrm{in}}}^{R_{\mathrm{out}}} - \sum_{i=1}^{\mathrm{N}} \int_{R_{\mathrm{gap-in\,,i}}}^{R_{\mathrm{gap-out\,,i}}} \right) \frac{R\, dR}{e^x - 1}. \tag{2.1}$$

The major difference between the eq. (1.51) and (2.1) is in the second term, which is subtracting the radiation effect on the scale of the gap regions created by the perturbers (here marked by the inner and outer gap radius for the i-th gap $R_{\mathrm{gap-in\,,i}}$ and $R_{\mathrm{gap-out\,,i}}$, respectively). The mentioned second term is specific to the secondary component scenario, if and only if the gap is opened. The advection, possibly replaced by the dust component scenario, is implemented in the lower integration boundary R_{in} of eq. (2.1), i.e. the inner edge of the disc is just being shifted further away from the central object ($R > R_{\mathrm{ISCO}}$).

Finally, let us mention an interesting configuration that has been considered by Metzger et al. (2022) in the context of Quasi-Periodic Eruptions, namely, the possibility of modulation due to the Roche-lobe overflowing material from an orbiting star that interacts with a secondary perturber moving closer to the SMBH in the retro-grade direction. The authors discuss both the magnitude of signal modulation as well as the resulting time-scales.

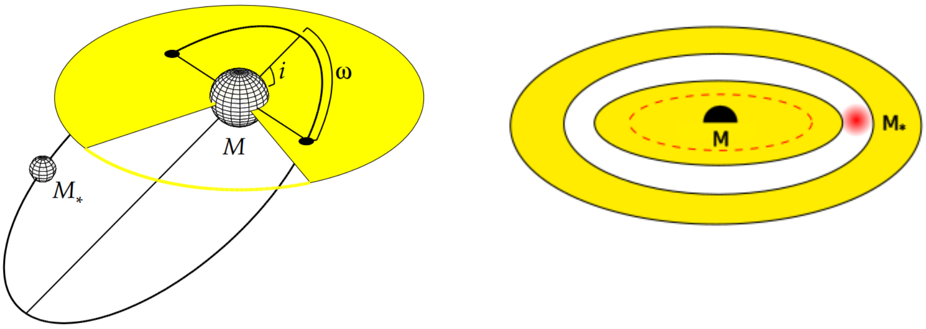

Figure 2.1: *Left panel:* The schematic drawing shows the initial system setup with a satellite body of mass $M_\star$ orbiting the central body of mass M. The central body lies at the centre of the elliptical trajectory of the orbiter, with the inclination i and the argument of pericentre ω. The accretion disc medium is highlighted by the yellow color. The image has been adapted from Šubr and Karas (1999). *Right panel:* On the other hand, at subsequent stages of the orbit evolution, the trajectory becomes inclined into the disc plane. Then it may or may not open a gap and produce specific spectral signatures in the emerging continuum and spectral lines, which reflect the parameters of the system including the central black hole and the secondary orbiting perturber. In case of secondary perturber being a star, the red dashed line marks the terminal radius below which the star gets tidally disrupted.

2.2 Tidal effects on stars and interstellar medium

Stars on eccentric orbits, which get eventually circularized, are in general slowly spiralling down onto the compact object. There is a significant distance threshold once the star reaches distance where it is no longer able to retain its structure (using self-gravity) in contrast with the tidal forces of the central body. This terminal distance is called tidal radius and is defined as (Hills, 1975; Luminet and Marck, 1985; Rees, 1988)

$$R_{\mathrm{tidal}} \approx \left(\frac{M_{\mathrm{SMBH}}}{M_*}\right)^{\frac{1}{3}} R_*, \tag{2.2}$$

with M_* and R_* being the mass and radius of the star, and M_{SMBH} the mass of the SMBH. Equation (2.2) shows the tidal radius scales as $M_{\mathrm{BH}}^{\frac{1}{3}}$, whereas the position of the event horizon given by the eq. (1.3) scales with M_{SMBH}. Hence for really massive compact object we can expect the star to reach event horizon prior to the tidal radius and therefore skip the tidal disruption part and be directly engulfed by the central body. Apparently there has to be a limit mass for the central body to prevent that from happening which is defined as (e.g. Stone, 2015)

$$M_{\rm Hills} = 1.1 \times 10^8 M_\odot \left(\frac{R_*}{R_\odot}\right)^{\frac{3}{2}} \left(\frac{M_*}{M_\odot}\right)^{-\frac{1}{2}}, \tag{2.3}$$

with $M_\odot$ and $R_\odot$ being the mass and radius of the sun. The formula clearly states that each star with a mass M_* and radius R_* uniquely narrows down the mass range for the central object in order to be tidally disrupted.

Coughlin and Nixon (2022) have argued that the precise value of tidal disruption events can have a large impact on their observational signatures. The distance of the closest approach to SMBH at which the star becomes fully disrupted should be in fact identified by equating the tidal field of the SMBH to the maximum self-gravitational field *within the star*, which depends on the radial density profile and the core density $\rho_{\rm core}$ (presumably much higher than the surface density of the star ρ_*). This leads to the introduction of the core radius into the problem, $R_{\rm c} = R_*(\rho_{\rm core}/\rho_*)^{-1/3}$, and hence the approximate radius of core disruption reads

$$R_{\rm tidal,core} = \left(\frac{M_{\rm SMBH}}{\rho_{\rm core}}\right)^{\frac{1}{3}}, \tag{2.4}$$

which comes out smaller than just plain $R_{\rm tidal}$. In consequence, the details of astrophysically realistic TDE depend on the type of the disrupted star and its internal structure (Bandopadhyay et al., 2024).

The TDEs prove to be very promising detectors for the activity in otherwise inactive galactic regions (see Komossa, 2015, and references therein). The major signs in favour for tidal disruption involve the bolometric luminosities $\approx t^{-\frac{5}{3}}$. These can, however, serve as a standalone tool for the detection of recoilling black holes (Liu et al., 2014) as the standard $t^{-\frac{5}{3}}$ can get periodically broken due to the orbiting secondary black hole. Furthermore, the spectra of TDEs tend to harden with time caused by the corona created due to the infalling material (e.g. Sazonov and et al., 2021). On the other hand the tidal disruption can cause a possible destruction of corona as well, when the disrupted material speeds up the accretion so fast it leads to the inner region's material depletion (e.g. Ricci et al., 2020).

In context of our proposed scenarios the tidal disruption can be used as a progenitor stage in case of the secondary component present (star). It can also open up the gap in inner region, such as observed by Ricci et al. (2020), that can be associated with the advection scenario setup or intrinsic reddening component.

2.3 The inner region and ADAF component

The innermost regions of the disc depends on the character of the central body, i.e. its mass, spin, charge (see Section 1). The prominent feature in influencing the geometry of the accretion disc lies in the spin parameter. The standard innermost stable circular orbit (ISCO) is located at $6R_{\rm g}$. However, this limit value for the inner radius of the orbiting matter can shift inwards or outwards depending on the value of spin $a > 0$ or $a < 0$, respectively (Bardeen et al., 1972). Although not exclusively, the accretion regimes of the observed sources do influence the inner region geometry as well.

The advection driven accretion flow (ADAF) is a result of drop in the accretion rate which causes the source's luminosity to be weaker (Narayan and McClintock, 2008). The initial idea of a flow proceeding in such manner dates back to the works by Ichimaru (1977), Narayan and Yi (1994) and Abramowicz et al. (1995). Most of the material energy is not released and the central body swallows it as it is. That is a direct result of the viscous processes acting faster than the cooling of the surrounding material. Therefore the systems suspected to be in ADAF regime are sometimes called radiatively inefficient accretion flows (RIAF;see e.g. Yuan and Narayan, 2014, for a recent overview).

The stream of hot diluted plasma, forming the ADAF region is optically thin. The specific constrains on the size of the ADAF are influenced by many factors, especially relative accretion rate. Nevertheless, the geometry of the ADAF region can in principle follow the toroidal structure, sharing the the axial symmetry of the surrounding accretion disc. The boundary conditions at the edge of the disc, particularly the torque condition can alter the radiation profile. Such condition, however, needs additional parametrization (Zdziarski et al., 2022). For the simplification we assume the ADAF region to be cut off at the edge of the disc as follows

$$R_{\mathrm{in}} = R_{\mathrm{ADAF}}. \tag{2.5}$$

The strong ADAF principle states that whenever the situation allows it the accretion flows in that particular regime at a particular radius R (Abramowicz et al., 1995; Honma, 1996; Kato and Nakamura, 1998). The semi-empiric formula allowing to formulate the extent of the ADAF inner region is as follows

$$R_{\mathrm{ADAF}} = 4\alpha_{0.1}^{4}\dot{m}^{-2}R_{\mathrm{g}}, \tag{2.6}$$

where $\alpha_{0.1}$ is the viscous parameter (see eq. 1.40) normalized to 0.1.

Now assuming the strong ADAF principle, the low accreting sources allow for the ADAF region to grown into large sizes based on the eq. (2.6), as illustrated in Figure 2.2. The temperature of the material translates into the radiation beyond the optical/UV band. The ADAF contribution to the accretion disc's thermal radiation can be approximated by the UV/X-ray relation as (e.g. Netzer, 2019, and references therein)

$$\log L_{\nu(2keV)} = 0.62 \log L_{\nu(2500\mathring{A})} + 7.77, \tag{2.7}$$

where both $L_{\nu(2500\mathring{A})}$ and $L_{\nu(2keV)}$ are the luminosities calculated at the at $2500\mathring{A}$ (corresponding to $\approx 5eV$) and $2keV$, respectively

Given the assumption the ADAF region layer is not radiatively participating in the optical/UV band, one can interpret the missing contribution of the inner region as a central cavity, hence the inner gap.

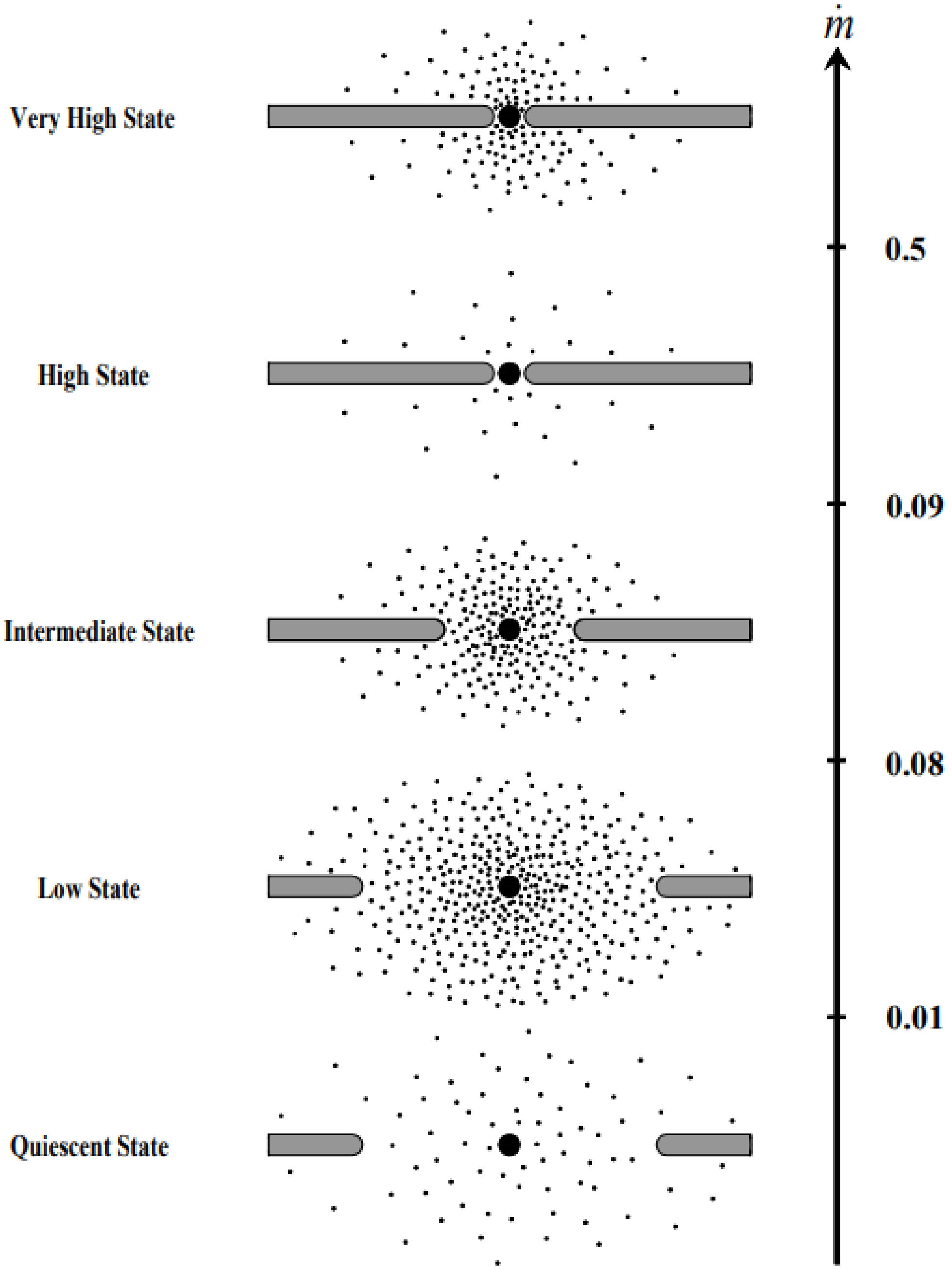

Figure 2.2: Phenomenology of different states of accreting black holes and the corresponding accretion rate $\dot{m}$ (relative to the Eddington rate). The hot, diluted phase (captured by dots) encircles a section of the equatorial thin accretion disc. The illustration represents effects on the accretion disc structure surrounding the central object. Moving from the very high accretion to the quiescent state (from top to bottom) we observe the ADAF region (marked by the black dots) changing its structure, increasing in size, and moving its position with respect to the section of the standard accretion disc. Image Credit: Esin et al. (1997).

2.4 The inner region and the dust component

The ADAF scenario and its variations are not exclusively responsible for the changes in the optical/UV. Kara and et. al (2021) argue the dust component consisting mainly of the ionized matter, such as in the case of Mrk18, can cause the decrease in the observed spectra as well. Generally, the extent of the decrease in the resulting observed spectra is strongly dependent on the parameters of the perturbers, mainly its position.

Based on the composition of the dust component, namely the dust being composed of amorphous carbon grains, we adopt the empirical formula for the extinction curve as (Czerny et al., 2004). The reddening effect due to the presence of the dust component causes decrease in the luminosity, hence

$$\frac{A_\lambda}{E(B-V)} \begin{cases} = -1.36 + 13\log\frac{1}{\lambda} & \text{for } 1.5 < \lambda^{-1} < 8.5\ [\mu m^{-1}], \\ = \ 0 & \text{for } \lambda^{-1} < 1.5\ [\mu m^{-1}], \\ = -1.36 + 13\log(8.5) & \text{for } \lambda^{-1} > 8.5\ [\mu m^{-1}], \end{cases} \tag{2.8}$$

with the extinction parameters $E(B-V)$.

Applying the introduced dust component allows to reference the dust-attenuated and the unperturbed luminosity L_ν^{reddened} and L_ν, respectively, in the rest frame of ν in the following way

$$\log \nu L_\nu^{\text{reddened}} = \log \nu L_\nu - 0.4A_\lambda. \tag{2.9}$$

The shape of the extinction curve (see Figure 2.3) alters mainly the higher energy band of the observed spectra, which can be associated with the dust component being located in the inner region of the proposed system. Therefore, the broken form of the extinction curve will have a rather specific effect on the luminosity decrease and remains to be determined if, and under what circumstances, it can be distinguished from the effects caused by other perturbers.

2.5 The outer region and the secondary component

Stochastic perturbations cause stellar motions to be directed to the central region of the galaxy. By doing so the stars will eventually be bound to the central SMBH which can give rise as depicted in Figure 2.1. In this simple scenario the SMBH is surrounded by the accretion disc. The newly gravitationally bound star is on elliptical orbit and is inevitably intersecting the accretion disc. These repetitive passages, complemented by the accretion disc's drag and the the central body gravitational pull cause the initial values of the orbital elements to change (e.g. Šubr and Karas, 1999).

Once in the orbital plane of the central object the fate of the star depends of the R_*/H ratio, where R_* is the effective star radius and H the accretion disc scale-height. The $R_*/H < 1$ the star gets engulfed by the accretion disc's material and will cause density waves travelling across the disc itself. The $R_*/H < 1$ ratio

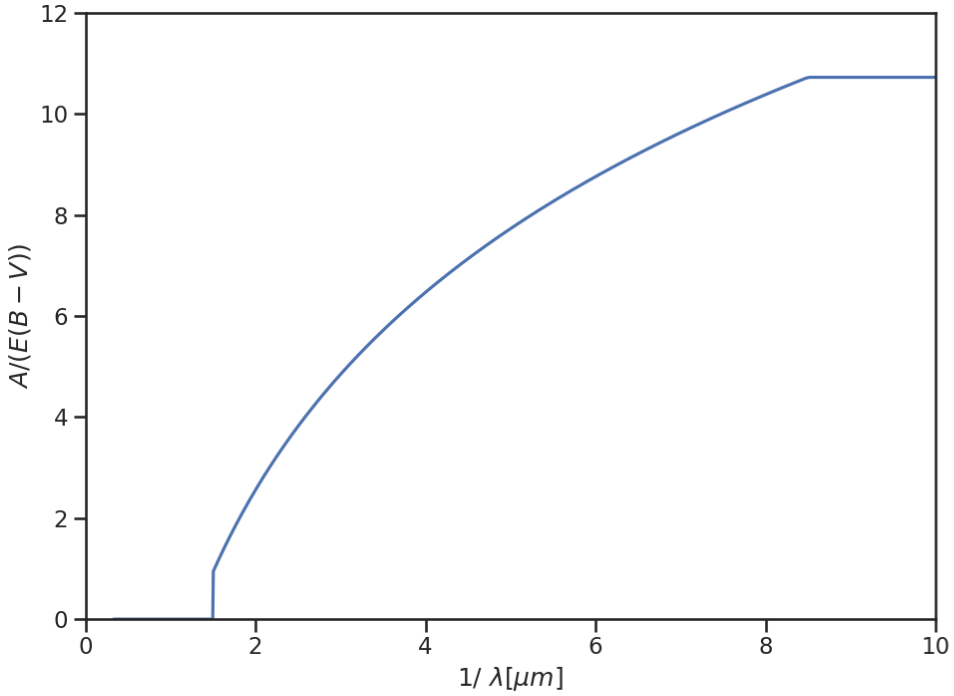

Figure 2.3: The broken quasar extinction curve described by the eq. (2.8) is based on obscuring medium being composed of amorphous carbon grains. The resulting intrinsic reddening of the optical/UV spectra can possibly exhibit somewhat similar features as in the ADAF inner gap scenario.

forces the disc to open up a gap with the respective star located at its centre (Karas and Šubr, 2001). The size of the gap is defined by the gravitational sphere of influence of the perturber; it can be expressed by the Hill radius as

$$\frac{\Delta R}{R_{\mathrm{g}}} \approx \frac{2d}{R_{\mathrm{g}}} \left(\frac{M_2}{3M_1}\right)^{1/3}, \tag{2.10}$$

with ΔR as the gap width, d denoting the distance of the primary and secondary body, M_1 and M_2 as mass of the primary and secondary body, respectively. In order for the gap trail to be stable we require the orbital period to be be substantially shorter than the viscous timescale, i.e.

$$\frac{t_{\mathrm{vis}}}{T_{\mathrm{orbit}}} = \frac{R^2}{H^2}\frac{1}{2\alpha\pi} \gg 1. \tag{2.11}$$

The standard Shakura Sunyaev thin disc framework requires $H/R \ll 1$ and the $\alpha \lesssim 1$. The star will have finished one orbit around the central body before the viscous processes start acting upon the accretion disc material and the gap starts filling up.

Applying the different mass ratios of the primary and the secondary in the eq. (2.10) leads to a clear conclusion that the gap width effect will favour the scenarios with greater mass ratios. Let us assume the mass of the primary being scaled to $10^9 M_\odot$ with the secondary to be a supermassive star of mass $100 M_\odot$. The gap width is approximated as

$$\frac{\Delta R_\star}{R_\mathrm{g}} \approx 0.64 \left(\frac{d}{100 R_\mathrm{g}}\right) \left(\frac{M_\star}{100\, M_\odot}\right)^{1/3} \left(\frac{M_1}{10^9\, M_\odot}\right)^{-1/3} . \tag{2.12}$$

The size of the gap for the distance of the secondary $\sim 100 R_\mathrm{g}$ amounts only for the gap width up to $\sim 0.1 R_\mathrm{g}$. This clearly illustrates that not even a supermassive star in the SMBH setting can open a gap large enough in the accretion disc. The wind-blowing stars as well as pulsar show also negligible effect in terms of not noticeable gap width (see Štolc et al., 2023, and references therein).

We change our approach and assume the character of the secondary component has to be that of a very massive, compact body, i.e a SMBH. In this fashion we set the mass ratio M_1/M_2 to 0.01, with the mass of the primary set to $10^9 M_\odot$ and the mass of the secondary, respectively. The Hill radius given by eq. (2.10) then adjusts to

$$\frac{\Delta R}{R_\mathrm{g}} \approx 29.9 \left(\frac{d}{100 R_\mathrm{g}}\right) \left(\frac{M_2}{10^7\, M_\odot}\right)^{1/3} \left(\frac{M_1}{10^9\, M_\odot}\right)^{-1/3} . \tag{2.13}$$

In this case the primary-to-secondary distance $\sim 100 R_\mathrm{g}$ can open up a gap with the size $\sim 10 R_\mathrm{g}$. The mentioned massive black hole scenario is, however, not an exclusive way how to open up a gap with the large enough width. Moranchel-Basurto et al. (2021) show via magnetohydrodynamic (MHD) simulations that the supernova explosion taking place in the orbital plane of the accretion disc or nearby can cause the material to be swept away. Hence creating a large space ≈ 0.01pc in the accretion disc that can potentially act as a gap.

The merging black holes emit gravitational radiation as they are closing in on each other. To constrain an astrophysically realistic distance of the secondary component from the primary one in the context of time-scale on which the two black holes merge by (Peters, 1964; Shapiro and Teukolsky, 1983) we define the merging timescale in general as

$$t_\mathrm{merge} = 1.24 \times 10^{-5} \left(\frac{a_\mathrm{init}}{R_\mathrm{g}}\right)^4 \left(\frac{M_\mathrm{tot}}{10^9 M_\odot}\right)^{-3} \left(\frac{x_\mathrm{p}}{0.5}\right)^{-1} \left(\frac{x_\mathrm{s}}{0.5}\right)^{-1} yr, \tag{2.14}$$

where a_init is the initial orbit radius of secondary component with respect to the primary one, M_tot the total mass in the system, x_p and x_s the ratio of mass of primary component and secondary component to the total mass in the system respectively. For the purposes of the future chapters let us reformulate the eq. (2.14) to

$$\begin{aligned} t_\mathrm{merge} &= \frac{5c^5}{256 G^3} \frac{a_0^4}{M_1 M_2 (M_1 + M_2)} \\ &= \frac{5c^5}{256 G^3} \frac{a_0^4}{x_\mathrm{p} x_\mathrm{s} M_\mathrm{tot}^3} \\ &\approx 12\,500 \left(\frac{a_0}{80\, R_\mathrm{g}}\right)^4 \left(\frac{x_\mathrm{p}}{1}\right)^{-1} \left(\frac{x_\mathrm{s}}{10^{-2}}\right)^{-1} \left(\frac{M_\mathrm{tot}}{10^9\, M_\odot}\right)^{-3} \mathrm{yr}. \end{aligned} \tag{2.15}$$

We use the results of this formula in the next section, as for the mass ratio M_2/M_1 of 0.01 the merging timescale of $\sim 10^4\,yr$ allows for the primary and secondary distance to be $\sim 100 R_{\rm g}$.

Cosmological simulations indicate that about 16% of all mergers are triple interactions (Kelley et al., 2017). The set-up can be similar to the Hills mechanism of a stellar binary approaching the SMBH on a parabolic orbit. In this case, we would imagine a bound pair of two massive black holes that approach the primary SMBH on a parabolic orbit. The ratio of masses would be $M_{\rm pair}/M_1 \sim 10^{-2}$. For instance, two orbiting black holes with $10^6\,M_\odot$ would approach the primary SMBH with $10^8\,M_\odot$, the binary would break up and two components would orbit the SMBH independently and later on would form gaps in the disc. Alternatively, the approaching bound pair could consist of intermediate-mass black holes with $10^4\,M_\odot$-massive components approaching the less massive primary of $10^6\,M_\odot$. In both situations, the gap width would be $\sim 15\,R_{\rm g}$ if one components orbits at $50 R_{\rm g}$ and $\sim 30\,R_{\rm g}$ of the other components is at $100 R_{\rm g}$. However the simulation of spectral properties of such systems would inevitably have to rely on realistic distances rather than arbitrary one. The issue lies within the fact that the triple merger is essentially three-body problem that requires limitations in order for the solution to be analytical.

Based on the accretion disc structure surrounding the primary the thermal profile of the source changes. As the radiating surface decreases, the blackbody contribution of the disc's rings is eventually attenuated at certain frequencies (e.g. Gültekin and Miller, 2012; Štolc et al., 2023). However, additional assumptions, in addition to those about the mass ratio and the merging timescales, have to be made in order that the merger scenario is stable (see sect. 3.1).

2.6 Central ADAF and secondary SMBH gap

Let us combine the effect of ADAF region that tends to create an apparent central cavity's effect in the optical/UV and we couple its effects with that of the secondary black hole. The secondary component creates a gap further away from the centre, as discussed in the previous subsection, and the width of the gap is in the first approximation given by the Hill radius (see eq. (2.10)).The final full system setup is depicted in Figure 2.4.

The size of the ADAF region is depending on the relative accretion rate and for the low accreting source has the tendency to grow (see eq. (2.6)). The gap width, however, is not changing with the relative accretion rate and while the position of the secondary perturber is fixed at a certain distance d from the primary, for the low enough values of the relative accretion rate the ADAF region overlaps its position.

Corresponding to the Figure 2.4, one can replace the ADAF component by the dust component and study its additional effects as well. The dust component has qualitatively the same effect as the ADAF component. Also it is not changing its size with the relative accretion rate as the deciding factor is the extinction (see eq. (2.8)).

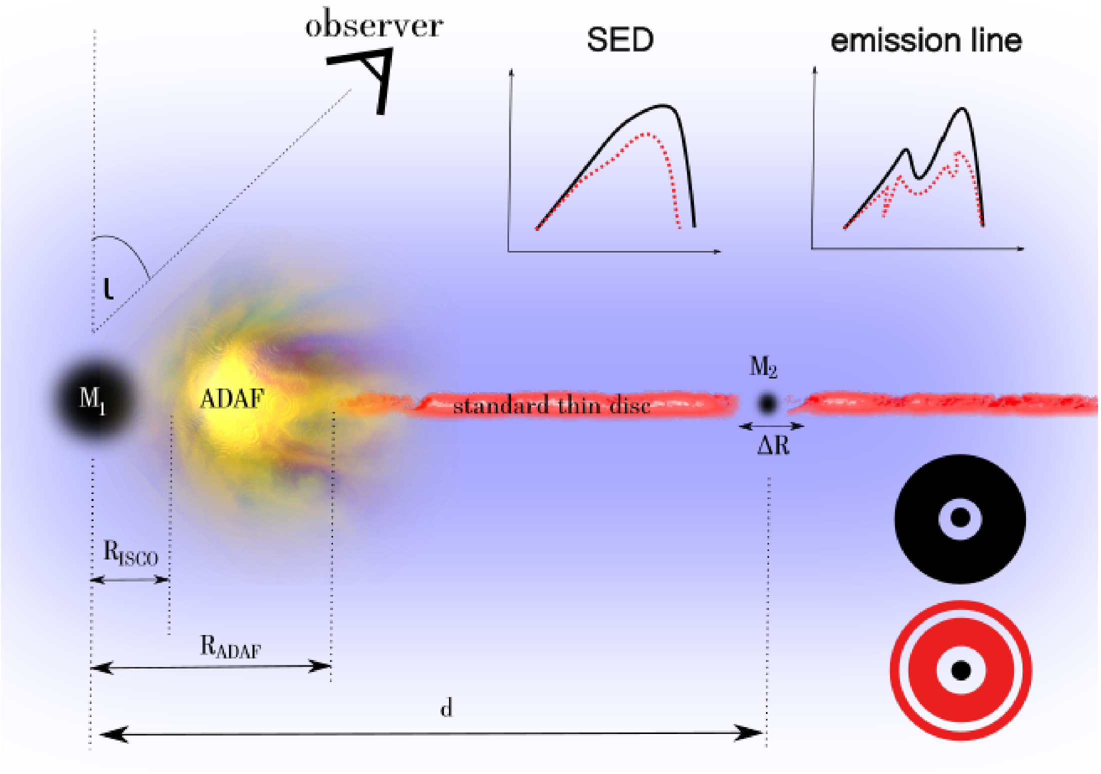

Figure 2.4: Sketch of our system setup showing the red color medium – the accretion disc surrounding the central black hole of mass M_1. The picture shows two potential perturbers: the ADAF region, marked by yellow color, and secondary black hole of mass M_2, alongside their effects on the SED and emission line in comparison to the unperturbed SED, which are marked by the red dotted and black solid lines, respectively. The bottom right corner of the figure illustrates the system setup in the face-on view. Further parameters such as inclination i, R_{ISCO}, R_{ADAF}, d and ΔR serve to illustrate the system geometry, scale and the respective ratio representation; this drawing has been adapted from Štolc et al. (2023).

2.7 Constraints from reflection spectral line

In this subsection we tease new constraints that can be obtained by including the reflection line of iron around 6–7 keV to the analysis on top of general broadband SED profile. This allows us to take advantage of well-resolved feature with a characteristic double-horn profile that can help to measure parameters of the system with better accuracy (e.g. Štolc and Karas, 2019), (Štolc et al., 2020), (McKernan et al., 2013).

We adopt a toy-model where the corona plays a crucial role in the mechanism of the creation of the Kα reflection spectral line of iron superposed on the underlying continuum. High-energetic photons are reflected from a cold slab of gas that builds the accretion disc. We assume the accretion disc to radiate with an intrinsic emissivity of the spectral line as

$$I_\nu(\nu, R) \propto \delta(\nu - \nu_0)\frac{1}{R^p}, \quad \delta(\nu - \nu_0) \approx \lim_{a \to 0} \exp\left[\frac{\nu - \nu_0}{a}\right], \tag{2.16}$$

i.e., the emerging energy is proportional to Dirac δ-distribution.

Here we assume the accretion disc to be immersed in corona from the inner region outwards. The parameter p in eq. (2.16) changes the value with respect to the ratio of the size of the accretion disc and the size of the corona $\frac{R}{R_\mathrm{c}}$ (Fabian et al., 1989). The intrinsic frequency is then $\propto \frac{1}{R^2}$ (parameter p is set to 2) for the ratio $\frac{R}{R_\mathrm{c}} \approx 1$ and $\propto \frac{1}{R^3}$ (parameter p is set to 3) for the ratio $\frac{R}{R_\mathrm{c}} > 1$.

We define the redshift factor as

$$g = \frac{\nu_\mathrm{observed}}{\nu_\mathrm{emitted}}, \tag{2.17}$$

where the ν_observed is the radiation frequency in the infinity, whereas the ν_emitted is the radiation frequency in the close proximity of the radiation source. Assuming the central body is a Schwarzschild black hole we employ the redshift formula in the following form (Pecháček et al., 2005)

$$g(R,\varphi,I) = \frac{\sqrt{R(R-3)}}{R + \sin(\varphi)\sin(I)\sqrt{R - 2 + 4(1+\cos(\varphi)\sin(I))^{-1}}}, \tag{2.18}$$

where R, φ and I stand for the radial coordinate, the azimuthal coordinate and the inclination of the system respectively. The redshift factor in this form involves the effect of gravitational redshift and light-bending that manifest mostly when close to the event horizon.

Due to the axial symmetry of the system the general formula for the observed flux (Hubený and Mihalas, 2014) simplifies to

$$F_\mathrm{observed}(\nu) \propto \int I_\mathrm{emitted}(\nu, R)\, g^3(R,\varphi,I)\,\mathrm{dS}, \tag{2.19}$$

with the infinitesimal surface element dS, and using the eq. (2.17) and the Liouville theorem $\frac{I_\nu}{\nu^3} = \mathit{constant}$.

To capture the effects of multiple-gap scenario in the spectral line simulations we need to subtract the contribution of the reflected radiation from the N gap regions (/surfaces) from the total reflection signal. The eq. (2.19) then translates as

$$\begin{aligned} F_\mathrm{observed}(\nu) \propto \int I_\mathrm{emitted}(\nu, R)\, g^3(R,\varphi,I)\,\mathrm{dS} \\ - \sum_{i=0}^{N} \int_i I_\mathrm{emitted}(\nu, R)\, g^3(R,\varphi,I)\,\mathrm{dS_i}, \end{aligned} \tag{2.20}$$

with the i-th gap, noted by the infinitesimal surface $\mathrm{dS_i}$, respectively.

We restrain our spectral line simulations to the inner regions of the accretion disc, i.e. up to $\sim$100 R_g. The outer regions do not account for a qualitative changes to the spectral line profile compared to the general relativistic effects – gravitational redshift and light-bending that manifest mostly when close to the event horizon. The ADAF scenarios are specifically interesting in this context as the major changes take place exactly in the inner regions of the accretion disc. In case we add the secondary component, specifically the secondary black hole, the distance limit up to 100 R_g, which would essentially correspond to the late stages of galaxy merger.

Focusing on the X-ray bands, specifically on the study of strong emission features similar to the Fe Kα line, high-sensitivity high-spectral-resolution data could provide observers with a promising chance to retrieve the parameters of the inner region, such as the inner and outer gap radii (see eq. (2.20)). Complementary to the set of parameters describing the primary component of the system one could constrain the mass of the perturber, and potentially its position can be also derived following the approach described in Semerák et al. (1999).

3. Results

In this section we present the results of simulations of spectral features such as thermal component, SED, in system with the Shakura–Sunyaev accretion disc surrounding the central body. We further introduce various perturbative terms to the system and study their effects and compare them with the unperturbed system scenario.

In our attempt to simulate astrophysically realistic simulations we introduce three scenarios (seee Figure 3.1):

- The Scenario I involves the central region set up with the the highly ionized matter present, i.e. ADAF region (see subsection 2.3). The central cavity does not contribute to the thermal profile of the accretion disc. Hence, we treat it as a central cavity in the disc.
- The Scenario II involves the secondary component, namely SMBH, causing the gap formation under the circumstances discussed in the subsection 2.5 of the previous section.
- Finally, the Scenario III features the central cavity alongside the secondary black hole component (see subsection 2.6). We simulate the spectral properties of such systems as well and try to set some constraints on the potential observability.

Additionally to the central cavity scenario, we consider the object as to be dust-enshrouded (see subsection 2.4). That provides the spectral features to have the effects of intrinsic reddening, which are qualitatively similar to those cause by the central cavity in the Scenario I.

In the follow up study we focus on the possible determination of the parameters based on the synthetic data. We choose a set of detectors to simulate the data for the given frequency bands. As an alternative we discuss employment of a newly designed observation tool QUVIK that would possibly help with the future observation. We further postulate the conditions of the observations, then focus on the data fitting and finally draw the results. The accuracy corresponds to the 10% and 2% in measured flux, which translates to the magnitude difference Δm 0.1 and 0.02, respectively (see subsection 3.2.2).

Additionally we present the simulation results of the emission line spectral features in the Scenarios I and II, assuming different intensity profiles (see subsection 2.7), draw out simple assumptions and conclude our study.

3.1 Justification of parameters

The main free parameters of the multi-gap model are as follows: inclination angle i, mass of the primary (central) black hole $10^9 M_\odot$, the relative accretion rate of the central object (in our case normalized in Eddington units) $\dot{m}$, the inner radius of the accretion disc marking the start of the ADAF component R_{ADAF} in case of Scenario I, the mass of the secondary black hole M_2, the distance between the

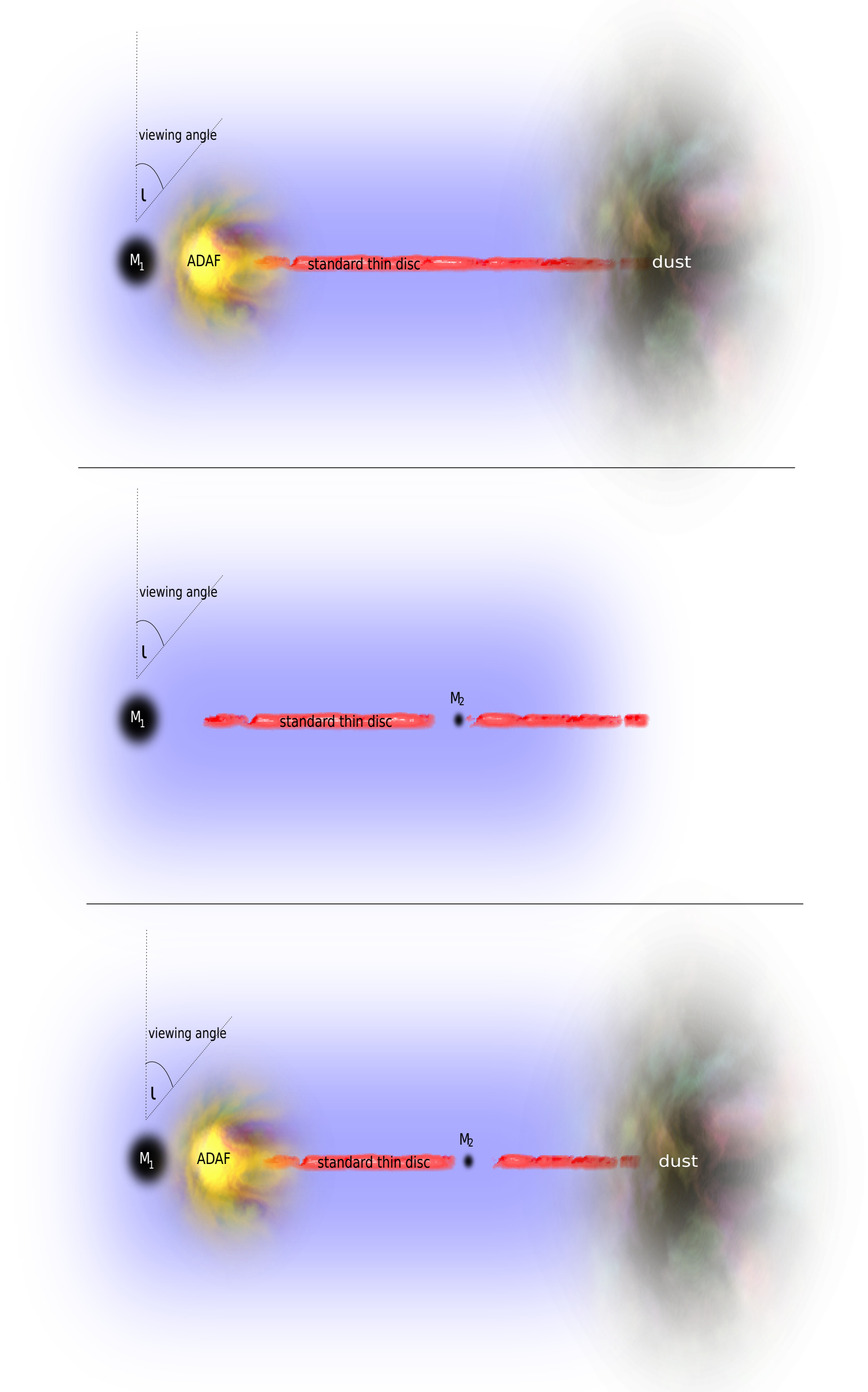

Figure 3.1: The sketch illustrates the system setup for Scenario I with ADAF component (top panel), Scenario II with secondary black hole component (middle panel), and Scenario III with both, ADAF and secondary black hole component (bottom panel). For the altered versions of the Scenario I and Scenario III (top and bottom panel, respectively), we add the dust components replacing the presence of the ADAF component, unless stated otherwise.

primary and the secondary black hole d. The last two additional parameters, M_2 and d, are taken into account for the Scenario II and III. To account for the color correction of the local black body contribution of the accretion disc we use the factor f_{col} in range between 1 and 2 (specifically $f_{\mathrm{col}} = 1.6$). For simplicity of our calculations we keep the size of the accretion disc to be fixed with the inner and outer radius R_{inner} and R_{outer} fixed to 6 and 5000 R_{g}, respectively, unless stated otherwise.

In the Scenario I we contemplate the contribution of the ADAF region to the thermal component of the radiation. Using the eq. (2.7) we calculate the power law emission of the central cavity and deduce its effects to be $\lesssim 1\%$ (for an illustration see Figure 3.2). As a result we neglect the ADAF contribution in the further calculations and effectively treat its presence as a missing part of the accretion disc.

As stated before, in Scenario II we introduce additional parameters. Namely, we assume the mass of the secondary black hole M_2, and the parameter describing the distance between the two bodies. We do not consider the mass of the secondary component $M_2 \approx M_1$ or $M_2 \approx 10^{-1} M_1$. Due to the similar mass range these scenarios would result in both component orbiting the centre of the mass of the system. Furthermore, the MHD simulations show the supermassive black hole binaries with both components of approximately same size (/mass) both tend to show signs of accretion disc structure each (see e.g. Farris et al., 2015, and references therein). For the purpose of a simple toy-model we neglect that kind of scenario as well. We plot the expected changes of the thermal component of the accretion disc for the scenario involving secondary component with different mass ratios (see Figure 3.3). We notice and neglect the mass ratios below 0.01 as they appear to have almost no effect on the spectra, i.e. ratio of the perturbed and unperturbed are well below 10%.

3.2 SED model profiles

We show the simulations of spectral properties given the specific scenario has been adopted in the studied system. We do so in order to benchmark the type effects and their scale after the perturbers have been introduced.

Starting with the Figure 3.4 we present the Scenario I, in which the central region of the accretion disc is essentially not visible in the UV as it is filled with highly ionized matter, hence acting as a central cavity. We plot the expected changes of the spectra varying with the size of the central cavity (see eq. (2.6)) for the relative accretion rate values $\dot{m}$ set to 0.4, 0.6 and 1.0. Simultaneously we present in the same plot the variation of Scenario I, whereas the central cavity is completely replaced by the dust enshrouding of the central body, which is represented by the luminosity decreasing term (see eq. (2.9)). The spectra with the dust component present vary with the extinction parameter $E(B{-}V)$ set to 0, 0.1 and 0.15, respectively. In both cases the perturbed to unperturbed ratios show a clear diminution in flux and specifically in the high frequency bands. However, the shape of the SED varies based on the type of the component affecting the inner region's contribution.

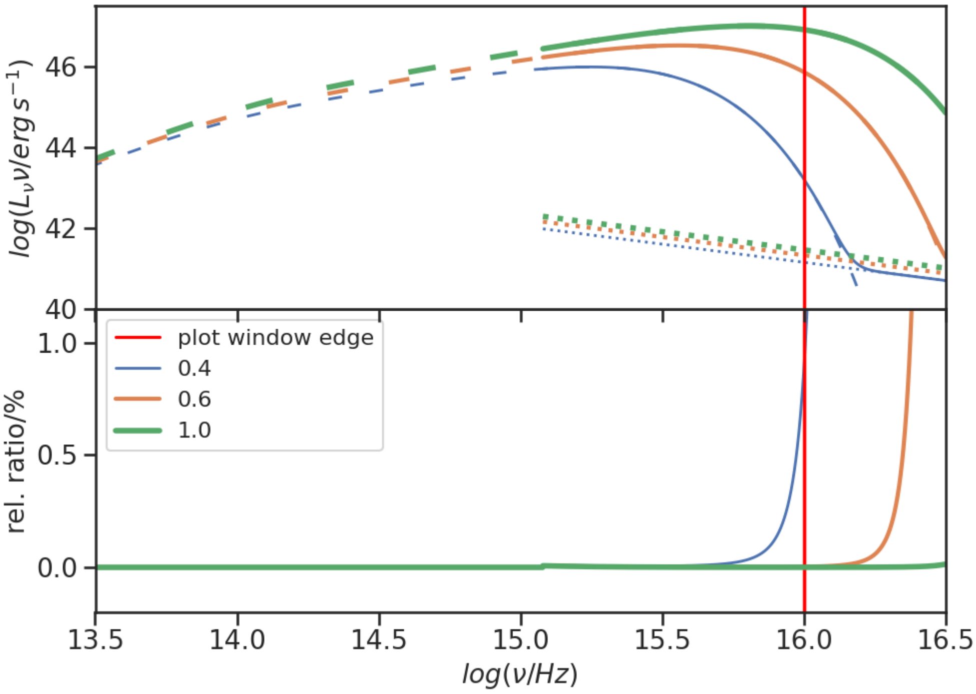

Figure 3.2: The broad band SED from the disc and assuming the varying ADAF plasma emission, caused by the corresponding power law contribution scaled using UV/X-ray relation given by eq. (2.7) with the power law index Γ set to 1.9. The E_{min} was calculated at 2500Å, corresponding to $\approx$ 5 eV. *Top panel:* Solid and dashed lines show SED with and without ADAF contribution, respectively. The dotted lines show the respective ADAF contribution in form of power law. The solid red vertical line marks the upper edge plot window assumed in our simulations. *Bottom panel:* Relative ratio of SED with and without ADAF contribution. *Both panels:* The inclination angle i is set to 35deg. The mass of the primary is set to $10^9 M_\odot$.

In Figure 3.5 we illustrate the effect of the Scenario II, namely introducing the secondary black hole component in the system. First we present the shots of the thermal component profile given different distance of primary from secondary d set to 200, 400 and 800 R_{g}, which according to the eq. (2.10) translates to the gap widths 60, 120 and 240 R_{g}. In the same plot we continue to decouple the effect of the varying accretion rate $\dot{m}$ set to 0.1, 0.4 and 1.0 as the distance of the secondary black hole is being fixed to the value of 400 R_{g} with the corresponding gap width 120 R_{g}. We notice the ratio of the perturbed and unperturbed spectra does not cross the value of $\approx$ 12 %, and specifically how it shifts once the secondary black hole, and the opened gap, are located further away from the central body.

The effects of the combination of both, central cavity and secondary black hole component, are shown in Figure 3.6. Now for the Scenario III we show the expected changes in the spectra due to the secondary black hole distance shifting to 200, 400 and 800 R_{g}, all while the relative accretion rate $\dot{m}$ is set to 0.4 and resulting in the central cavity fixed respectively. We also turn the

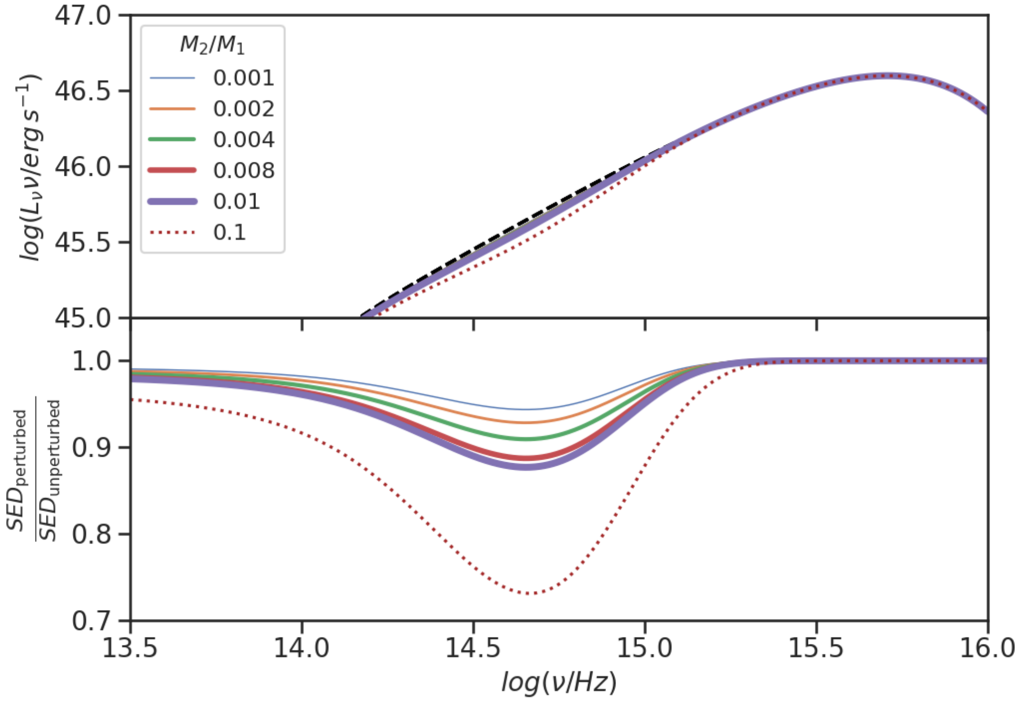

Figure 3.3: *Top panel:* SED simulations for the mass of the secondary component spanning from 10^{-3} (marked by solid colored lines) up to 10^{-1} (marked by a dotted line). Black dashed line marks the unperturbed SED. *Bottom panel:* Ratio of the perturbed to the unperturbed SED. *Both panels:* The inclination angle i is set to 35deg. The mass of the primary is set to $10^9 M_\odot$. The distance d of the secondary from the primary is set to $400 R_\mathrm{g}$.

situation around while fixing the position of the secondary component, i.e the gap width respectively, and we keep varying the relative accretion rate $\dot{m}$ set to 0.1, 0.4 and 1.0 with the expected changes of the spectra varying with the size of the central cavity (see eq. (2.6)). In both cases we observe strong decrease in the flux which is caused by the presence of the central cavity. We confirm the effect of the secondary black hole component on the shape of the spectrum, yet we notice there is a chance the central cavity and the secondary black hole may overlap hinting the effect of the latter negligible.

Finally we replace the central cavity component with the dust component completely and alter the Scenario III. The expected spectral changes in this setup are to be observed in Figure 3.7. Fixing the extinction parameter $E(B-V)$ to 0.1 we plot the spectra for growing gap width as 60, 120 and 240 R_g. The plot also involves the simulated data for the fixed gap width 120 R_g, with varying extinction parameter as 0, 0.1 and 0.15. Similarly as in Figure 3.6 using the perturbed/unperturbed ratios we notice the effects of the gap to prevail, especially if the gap is getting bigger. However, fixing the gap width and changing the dust component's extinction may possibly result in the overlapping of the two effects.

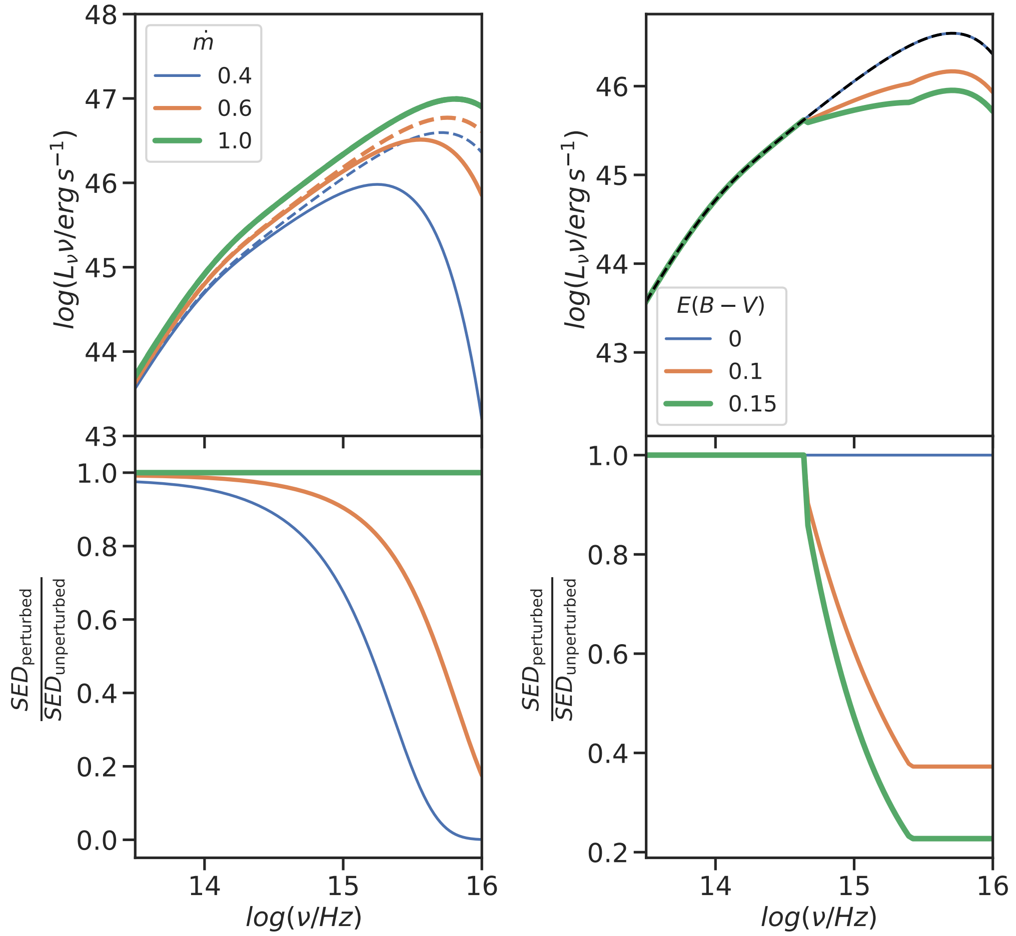

Figure 3.4: *Left panel:* SED simulated corresponding to the model with varying relative accretion rate, assuming strong ADAF principle. Colored dashed lines mark the respective unperturbed SEDs. *Right panel:* SED simulated corresponding to the model with dust component present, varying with the extinction $E(B-V)$. The fixed parameters are as follows: the relative accretion rate $\dot{m}$ set to 0.4. Black dashed line marks the unperturbed SED. *Both panels:* The inclination angle i is set to 35 deg. The mass ratio of the secondary and primary is set to 10^{-2} with the mass of the primary $10^9 M_\odot$, and the mass of the secondary set to $10^7 M_\odot$.

3.2.1 Available instrumentation

Aiming to recover the initial (assumed) values of the system parameters, we have chosen a suitable set of observation instruments to provide us with the astrophysically realistic and potentially measurable mock data. The list of photometric systems of detectors is as follows: the GALEX (Morrissey and et al., 2007), the Legacy Survey of Space and Time (LSST) (LSST and et al., 2009), SWIFT/UVOT (Poole and et al., 2008) and WISE (Wright and et al., 2010). We only use the effective wavelengths of the detectors and provide the additional

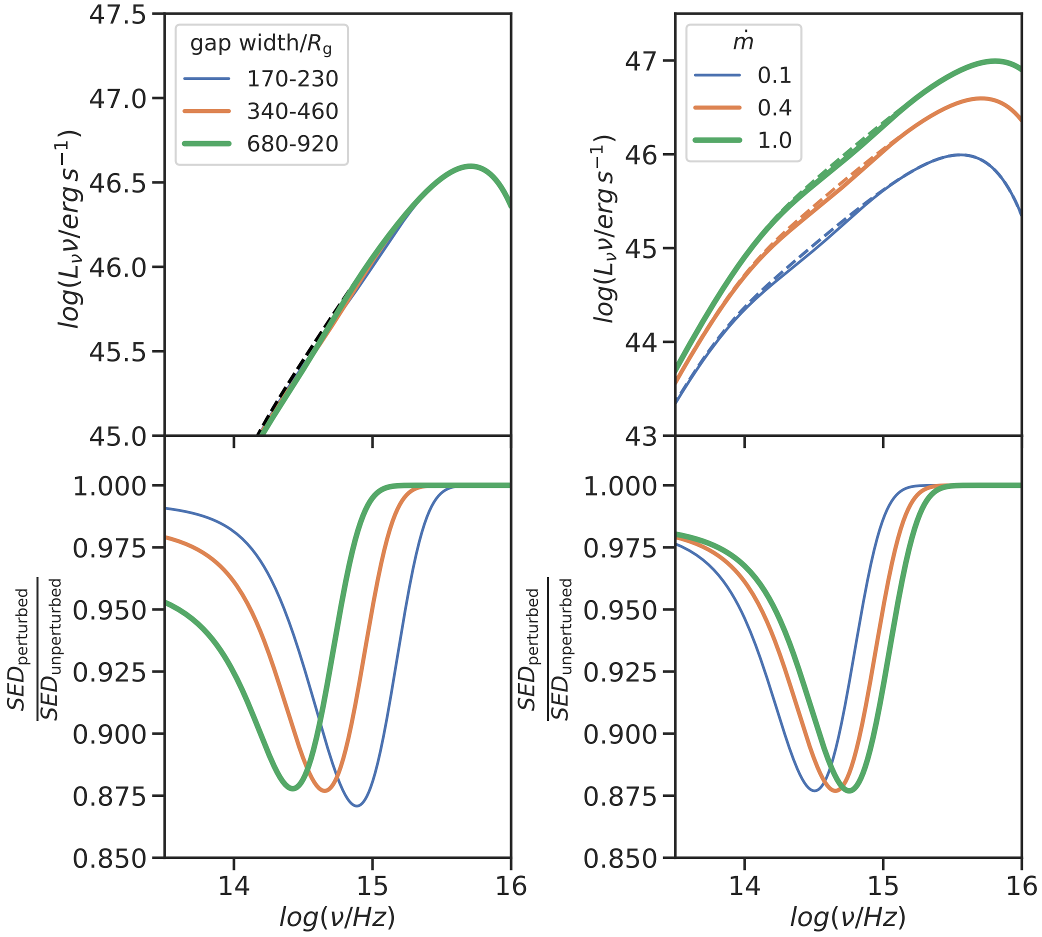

Figure 3.5: *Left panel:* SED simulated corresponding to the model with varying gap width in case of secondary component located in the middle of the gap. The fixed parameters are as follows: the relative accretion rate $\dot{m}$ set to 0.4. Black dashed line marks the unperturbed SED. *Right panel:* SED simulated corresponding to the model with varying relative accretion rate in case of secondary component present. The fixed parameters are as follows: the distance between the primary and secondary body d set to $400R_{\rm g}$, corresponding to the gap width of $120R_{\rm g}$. Colored dashed lines mark the respective unperturbed SEDs. *Both panels:* The inclination angle i is set to 35deg. The mass ratio of the secondary and primary is set to 10^{-2} with the mass of the primary $10^9 M_\odot$, and the mass of the secondary set to $10^7 M_\odot$.

information regarding the specific filter, central wavelength and the full width at half maximum (FWHM) in the Table 3.1.

To justify the application of multiple different observation detectors the observation timescale should cover the objects in such manner that there are no major changes in its radiation. That narrows down the possible systems to the high-accreting sources as they are less susceptible to show changes compared to

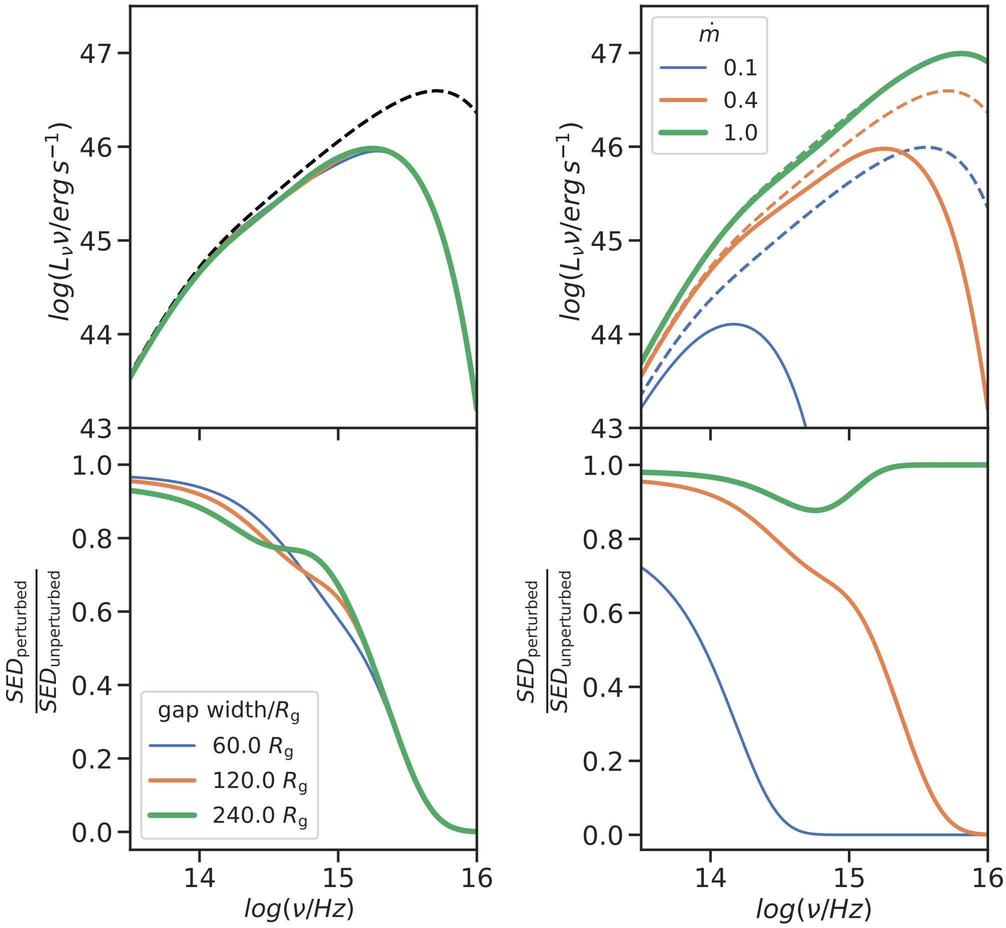

Figure 3.6: Simulated SED corresponding to secondary black hole scenario coupled with the assumption of strong ADAF principle. *Left panel:* The fixed parameters are as follows: the relative accretion rate $\dot{m}$ set to 0.4, the gap width varies with the distance of the secondary component located in the middle of the gap, corresponding to 200, 400 and 800R_g, respectively. Black dashed line marks the unperturbed SED. *Right panel:* The fixed parameters are as follows: the distance between the primary and secondary body set to 400R_g, corresponding to the gap width of 120R_g. Colored dashed lines mark the respective unperturbed SEDs. *Both panels:* The inclination angle i is set to 35deg. The mass ratio of the secondary and primary is set to 10^{-2} with the mass of the primary $10^9 M_\odot$, and the mass of the secondary set to $10^7 M_\odot$.

the low-accreting ones. Specifically, we require the system to be observed in the time interval proportional to the characteristic optical/UV timescale τ_char (Collier and Peterson, 2001). Additionally, the more massive the central object, in our case SMBH, the longer the the period variability timescale gets. A more detailed guess of the temporal condition for the joined observations can be found in Štolc et al. (2023).

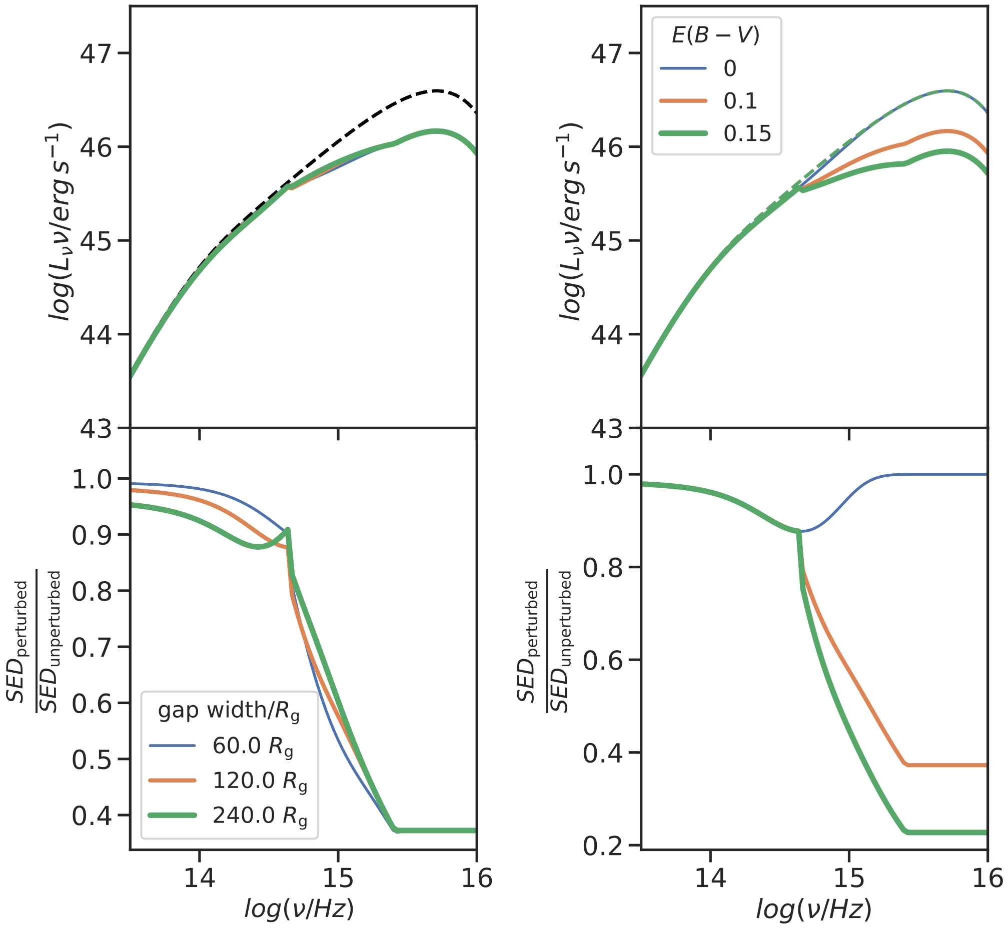

Figure 3.7: Simulated SED corresponding to secondary black hole scenario coupled with the presence of the dust component. *Left panel:* The fixed parameters are as follows: the extinction parameter $E(B-V)$ set to 0.1, the gap width varies with the distance of the secondary component located in the middle of the gap, corresponding to 200, 400 and $800 R_{\rm g}$, respectively. Black dashed line marks the unperturbed SED. *Right panel:* The fixed parameters are as follows: the distance between the primary and secondary body set to $400 R_{\rm g}$, corresponding to the gap width of $120 R_{\rm g}$. Colored dashed lines mark the respective unperturbed SEDs. *Both panels:* The inclination angle i is set to 35deg, the relative accretion rate $\dot{m}$ is set to 0.4. The mass ratio of the secondary and primary is set to 10^{-2} with the mass of the primary $10^9 M_\odot$, and the mass of the secondary set to $10^7 M_\odot$.

Although our simulations are exclusively for the set of detectors listed in Table 3.1, we do not neglect the possible implementation of UVEX detector, as well as AstroSat/UVIT that would provide event grater sensitivity given the magnitude changes of the source (see e.g. Dewangan et al., 2021). We further discuss the possible implementation of additional detectors for the potential future applications (see subsection 3.2.3). All in all, to provide the quality observation across the optical/UV band does not only require a set of instruments but also the cor-

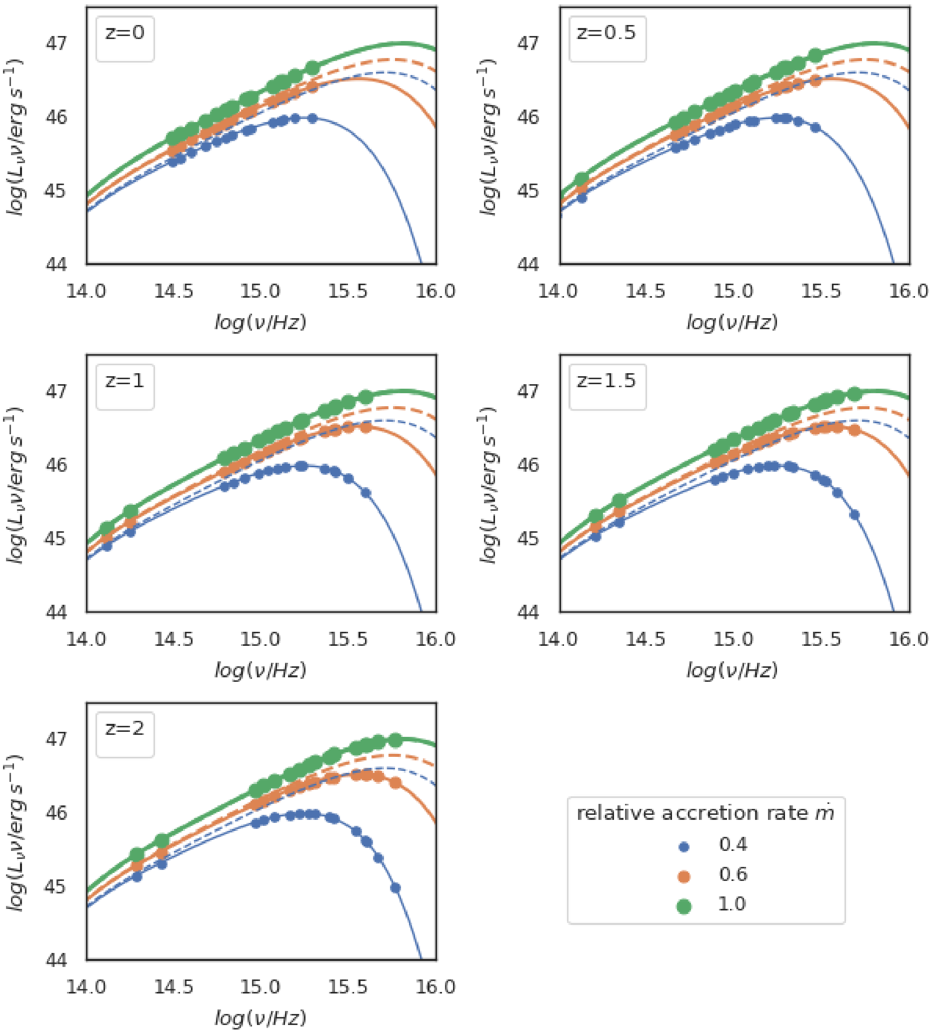

Figure 3.8: Simulated SED corresponding to the model with varying relative accretion rate, assuming strong ADAF principle and for different values of redshift in range of 0 to 2. In each panel the changing positions of points mark chosen instruments in the Photometry table 3.1 for given redshift, whereas the solid and dashed lines mark the identical theoretical prediction for perturbed and unperturbed full SED model, respectively.

responding operational timescales of the responsible detectors to receive viable results based on the future observations.

In the following tables 3.2 - 3.5 we present the fit results of our simulations. We note, we do not take into account the Balmer contribution as well as the additional contribution due to BLR emission lines. We focus on the high-accreting sources with the relative accretion rate $\dot{m}$ between 0.4 and 0.6. The mock data we work with were generated assuming the additional errors up to 2% and 10% in the measured flux, respectively. The errors are Gaussian-distributed. To check for

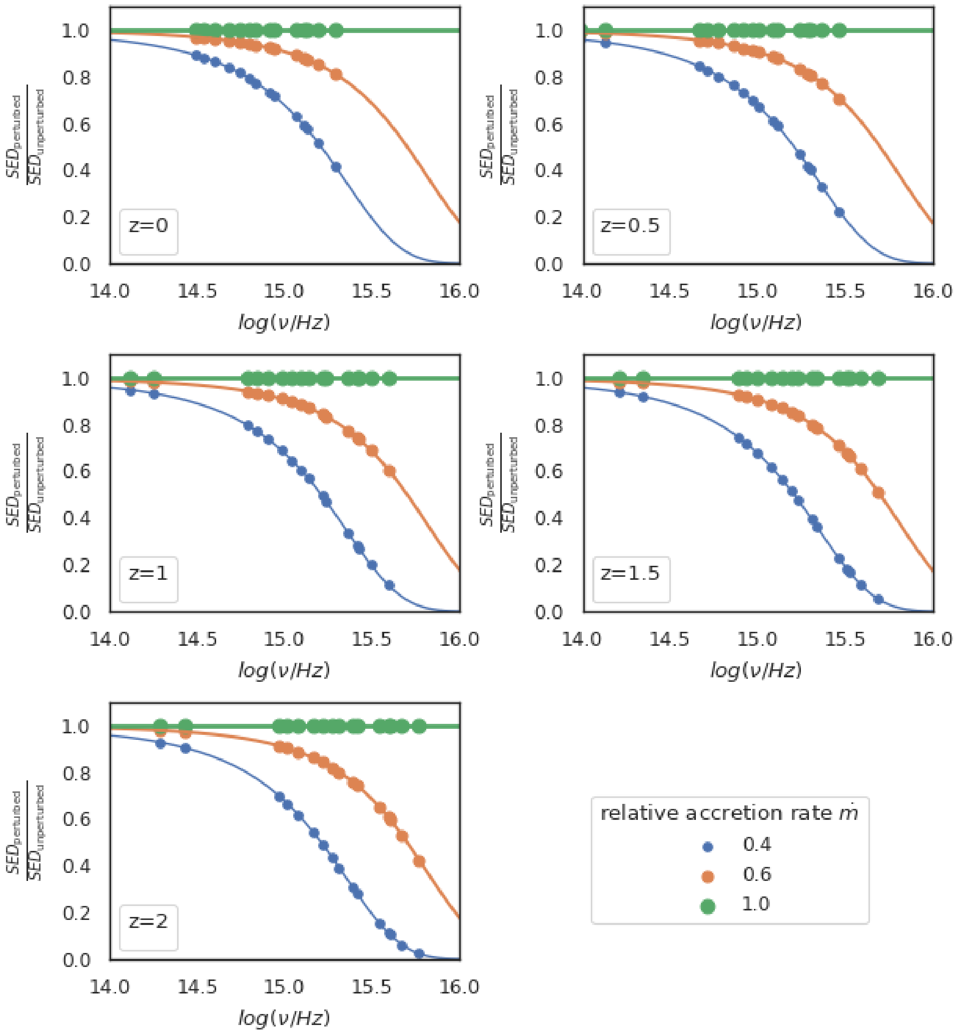

Figure 3.9: Ratios of perturbed and unperturbed SED with varying relative accretion rate, assuming strong ADAF principle and for different values of redshift in range of 0 to 2 (see Figure 3.8). In each panel the changing positions of points correspond to the ratios of chosen instruments in the Photometry table 3.1 for given redshift, whereas the solid lines mark the identical theoretical prediction for the ratios of the perturbed and unperturbed full SED models.

the correspondence between the assumed simulation values and the fit results we therefore use the goodness of fit method χ^2_ν. In our case, the reduced χ-squared method, defined as $\chi^2_\nu = \chi^2/(N-\nu)$, handles in each batch of our mock data consisting of N, namely 16 luminosity points (see Table 3.1, and latter 3.6) on the log scale, with the corresponding number of free parameters ν for the given applied model.

To account for the necessity of the perturbed models and show their real applicability we compare the perturbed and unperturbed version for each presented

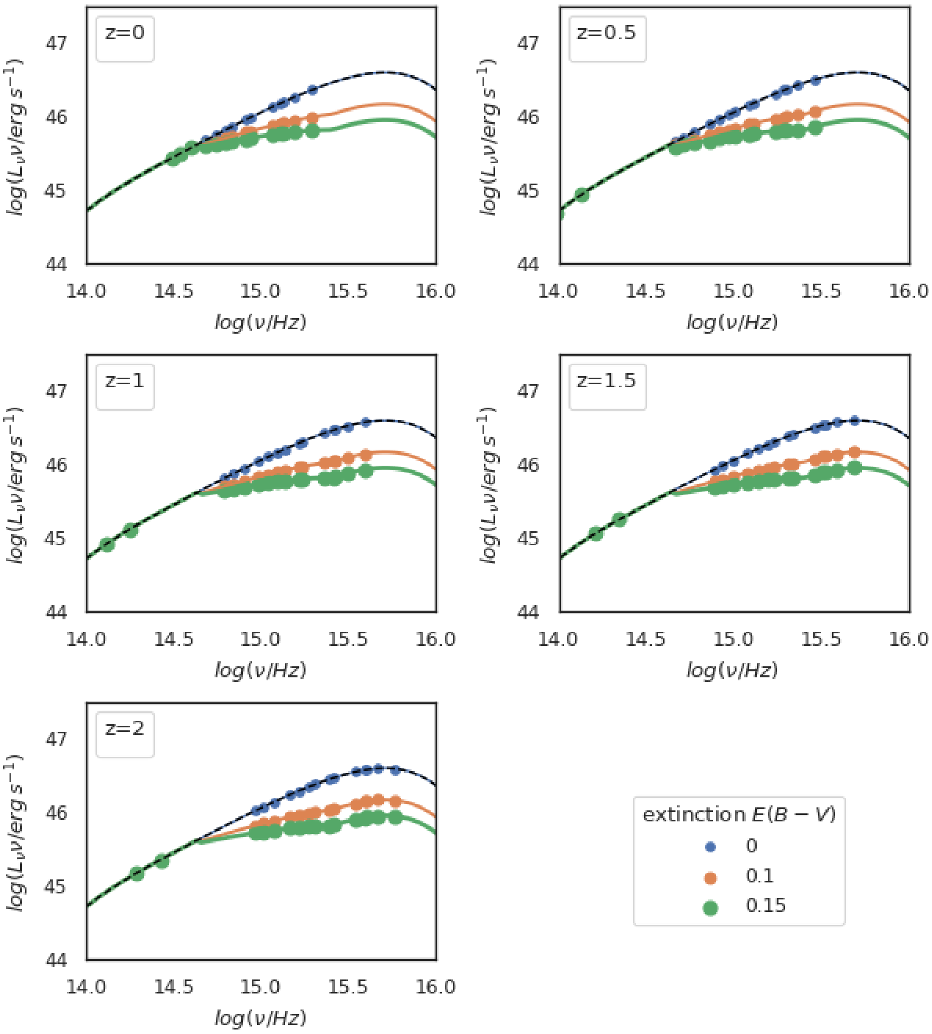

Figure 3.10: Simulated SED corresponding to the model with varying extinction parameter, and for different values of redshift in range of 0 to 2. In each panel the changing positions of points mark chosen instruments in the Photometry table 3.1 for given redshift, whereas the solid and dashed lines mark the identical theoretical prediction for perturbed and unperturbed full SED model, respectively.

scenario. For the comparison we additionally use both, the Akaike (Akaike, 1973) and Bayesian Information (Schwarz, 1978) criterion AIC and BIC, , respectively. The ΔAIC and ΔBIC between the perturbed and unperturbed cases either point out to ambiguous or favour the better fitting model, assuming altered amount of parameters. Specifically, higher Δ-values of the AIC and BIC criteria tend to indicate the additional parameter of the model has been chosen correctly et vice versa.

The introduced models corresponding to Scenario I, its variation with the dust component, Scenario II and Scenario III, all involve a number of parameters. Our

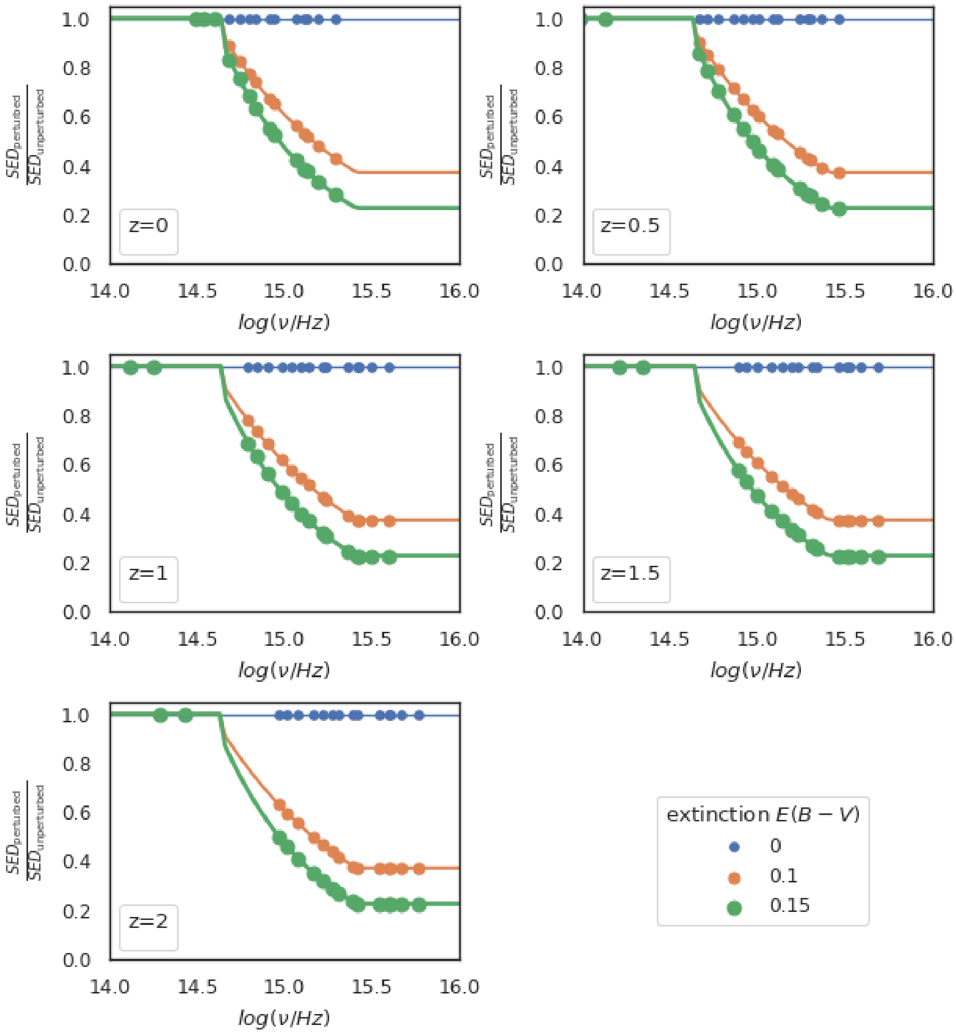

Figure 3.11: Ratios of perturbed and unperturbed SED with varying extinction parameter, and for different values of redshift in range of 0 to 2 (see Figure 3.8). In each panel the changing positions of points correspond to the ratios of chosen instruments in the Photometry table 3.1 for given redshift, whereas the solid lines mark the identical theoretical prediction for the ratios of the perturbed and unperturbed full SED models.

key task is to narrow down this number. First, we fix the mass of the central object M_1. The spectral line properties can potentially unravel the value of such parameters (see e.g. Vestergaard and Peterson, 2006). The next fixed parameter throughout out our study is the inclination angle i, as in reality there are a number of independent methods to deduce the respective value such as spectral line fitting, polarimetry, etc. For simplicity of our calculations we keep the size of the accretion disc to be fixed with the inner and outer radius $R_{\rm inner}$ and $R_{\rm outer}$ fixed to 6 and 5000 $R_{\rm g}$, respectively, unless stated otherwise.

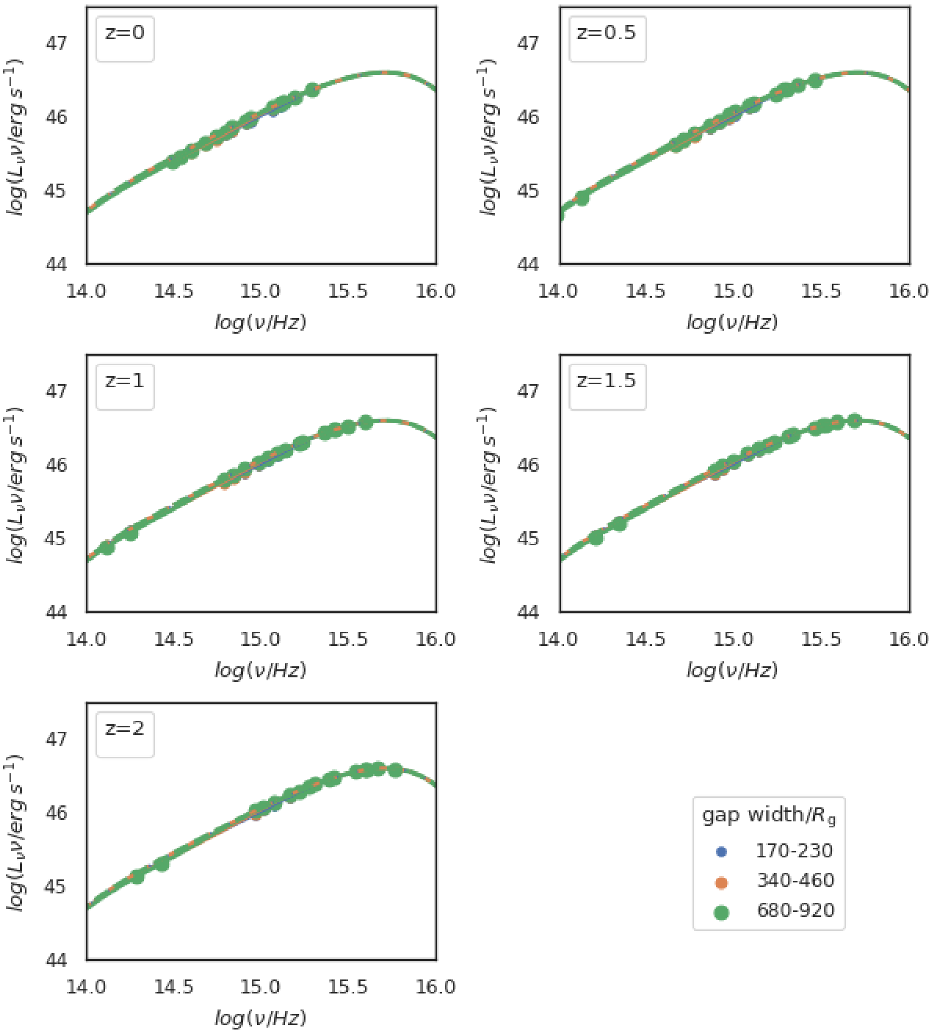

Figure 3.12: Simulated SED corresponding to the model with varying gap width corresponding to the secondary's distance 200, 400 and 800 R_g, respectively, and for different values of redshift in range of 0 to 2. In each panel the changing positions of points mark chosen instruments in the Photometry table 3.1 for given redshift, whereas the solid and dashed lines mark the identical theoretical prediction for perturbed and unperturbed full SED model, respectively.

Now, in Scenario I we introduce the strong ADAF principle and assume the highly ionized matter of the central region essentially behaves like a gap in the optical/UV. The size of the region is parametrized by the eq. (2.6). However, for fitting in this scenario we presume no entanglement between the relative accretion rate and the size of the ADAF region and treat the parameters as independent. We present the results of the data fitting of the mock data assuming the 10% errors in the measured flux in Table 3.2. We present the results for different values of the redshift of the observed source, z set to 0, 0.5, 1, 1.5 and 2, and find

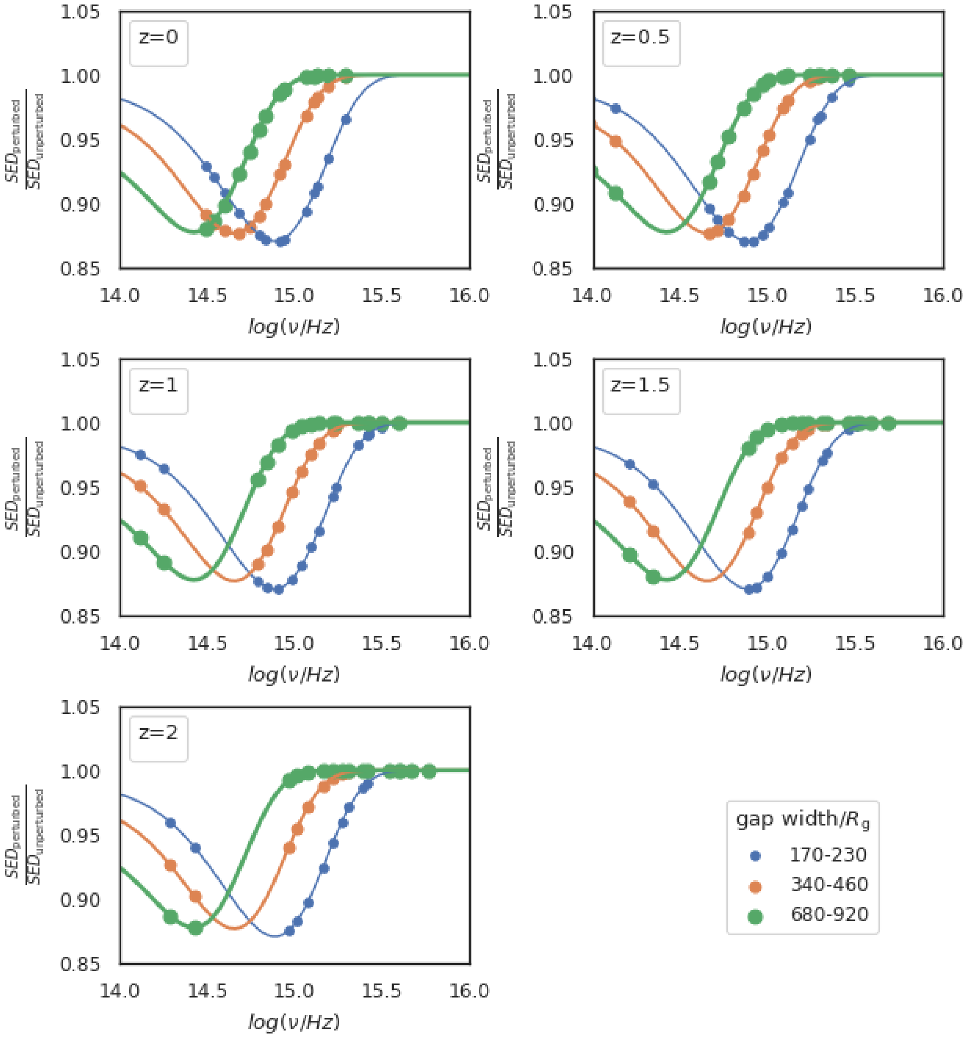

Figure 3.13: Ratios of perturbed and unperturbed SED with varying gap width corresponding to the secondary's distance 200, 400 and 800 R_g, respectively, and for different values of redshift in range of 0 to 2 (see Figure 3.8). In each panel the changing positions of points correspond to the ratios of chosen instruments in the Photometry table 3.1 for given redshift, whereas the solid lines mark the identical theoretical prediction for the ratios of the perturbed and unperturbed full SED models.

the model is fitting the data reasonably well independent on the redshift based on the fit values of the studied parameters $\dot{m}$, $R_{\rm ADAF}$ and on the χ^2_ν test. In Figure 3.8 and 3.9, showing the simulations of perturbed and unperturbed SEDs in Scenario I (strong ADAF assumption adopted) together with the set of our mock data points, we notice the mock data of either redshift value capture the essence of the spectra accordingly. Hence the redshift does not play a role in the determination of better conditions for the fitting procedure.

Once we introduce the dust component in the system, we have to account for the change by involving additional parameter – extinction $E(B-V)$. In this altered scenario we still take into account strong ADAF assumption as well and we do not bound the relative accretion rate $\dot{m}$ and the size of the ADAF region R_{ADAF}. Consequently we then fit our mock data with the three parameter model with the 10% errors in the measured flux. We do so for different values of redshift, namely 0, 0.5, 1, 1.5 and 2. The fit results can be found in Table 3.3 and show that the model is fitting the data reasonably. We also notice that the results get more accurate depending on the redshift of the source (based on the χ^2_ν test). The major result for this scenario is that the we are capable to disentangle the effect of both ADAF region and the dust component at the same time – in this case the higher the redshift, the better results. In Figure 3.11 and 3.11 we show the simulations of perturbed and unperturbed SEDs in case of only dust component present together with the set of our mock data points. Similarly as in case of Scenario I we notice the mock data of either redshift value capture the perturbed SED effect very well. However, the higher values of redshift, the better the discontinuity introduced by the dust component is covered by the mock data itself. Hence the redshift does play a role in the determination of better conditions for the fitting procedure to some minor extent.

Finally we fit our mock data corresponding to the Scenario II that involves the secondary black hole component. The set of free parameters for this particular scenario involves the relative accretion rate $\dot{m}$, the inner and outer gap radius R_{inner} and R_{outer}, respectively. In Table 3.4, when the fitting the data with the errors op to 10% in measured flux we see that thawing/freezing the gap parameters does not have almost any effect on the results. The χ^2_ν, as well as the ΔAIC and ΔBIC are ambiguous and one cannot determine the better fitting model. The situation is different once we assume the 2% errors in our mock data and the perturbed model is clearly favoured over the unperturbed one as we can observe via χ^2_ν, as well as the ΔAIC and ΔBIC values (see Table 3.5). We also notice the slight effect of the redshift of the source that indicates the bigger the redshift the worse the fit results. That is to be expected as the bigger gaps tend to be located further away, hence the flux decrease is shifting to the lower energy bands that are not covered by the mock data. In Figure 3.12 and 3.13 we show the simulations of perturbed and unperturbed SEDs with the secondary component present together with the set of our mock data points. Unlike in previous cases (Scenario I and its altered version with the dust component), in case of Scenario II we notice the mock data to cover the perturbed SED effect less and less effectively as the value of redshift grows. Hence the fit results for the Scenario II tend to worsen as the redshift value increases.

We have also tried to infer the initial secondary black hole parameters in Scenario II – its distance from the primary d and its mass M_2 based on the fit results. If 10% errors are assumed there is almost no chance to constrain the given parameters (see the inferred values' columns in Table 3.4). However, if we lower the errors to 2% the parameters can be determined more accurately (see the inferred values' columns in Table 3.5). In order to calculate the given parameters as well as their errors we used the error transfer relation and its corresponding forms for the respective parameters (see subsection 3.2.2).

Instrument	Filter	Central Wavelength (Å)	FWHM/bandpass (Å)
GALEX	FUV	1538.6	1344 – 1786
	NUV	2315.7	1771 – 2831
LSST	u	3671	3200 - 4000
	g	4827	4000 - 5520
	r	6223	5520 - 6910
	i	7546	6910 - 8180
	z	8691	8180 - 9220
	y	9712	9500 - 10800
SWIFT	uvw2	1928	657
	uvm2	2246	498
	uvw1	2600	693
	u	3465	785
	b	4392	975
	v	5468	769
WISE	w1	33680	28000 - 38000
	w2	46180	41000 - 51000

Table 3.1: Photometry table listing the initial set of observational instruments alongside their respective parameters such as the filter, the central wavelength and the FWHM.

3.2.2 Inferred values of the model parameters

Using the fit results based on our synthetic data we attempted to test the model prediction and retrieve the initial set of parameters of the distance d and the mass of the pertuber M_2 in Scenario II. These parameters, however, needed to be calculated based on the fit results as well as the respective error terms. Hence, we utilized the propagation of uncertainty, which, is generally a multivariate problem resulting in the following formula

$$\sigma_y = \sqrt{\sum_{i=1}^{n} \left(\frac{\partial f(x_i, ..., x_n)}{\partial x_i} \right)^2 \sigma_{x_i}^2}, \tag{3.1}$$

where $f(x)$ is the studied quantity parametrized by the x_i, for $i = 1, ..., n$. The distance between the primary and secondary component is given by the mean of the inner and outer gap radius $R_{\text{gap in}}$ and $R_{\text{gap out}}$. Consequently, given the error transfer eq. (3.1), we write for the error term of distance of the secondary component following

$$d = \frac{R_{\text{gap in}} + R_{\text{gap out}}}{2}, \tag{3.2}$$

$$\sigma_d = \frac{1}{2} \sqrt{\sigma_{R_{\text{gap in}}}^2 + \sigma_{R_{\text{gap out}}}^2}. \tag{3.3}$$

The gap width ΔR can be in first approximation given as the difference between the outer and inner gap radii $R_{\text{gap out}}$ and $R_{\text{gap in}}$, with its respective error term

assumed values		fit values		
$\dot{m}$	R_{ADAF} (R_{g})	$\dot{m}$	R_{ADAF} (R_{g})	χ^2_ν
z=0				
0.4	11	0.41 ± 0.03	11 ± 3	1.2
0.4	25	0.41 ± 0.03	25 ± 3	1.7
z=0.5				
0.4	11	0.43 ± 0.03	12 ± 2	1.3
0.4	25	0.42 ± 0.03	25 ± 2	1.2
z=1				
0.4	11	0.39 ± 0.03	11 ± 1	1.6
0.4	25	0.43 ± 0.02	26 ± 1	1
z=1.5				
0.4	11	0.45 ± 0.03	13 ± 1	1.2
0.4	25	0.38 ± 0.02	24 ± 1	1.3
z=2				
0.4	11	0.40 ± 0.02	11 ± 1	1.1
0.4	25	0.40 ± 0.02	25 ± 1	1.1

Table 3.2: Fitting results of data simulated for model involving ADAF component (Scenario I). The errors correspond to 10% in the measured flux. Each row for the particular mock data shows the assumed values of the simulation and fitting results obtained for a given redshift z of the source. The fixed parameters are as follows: M_1 set to $10^9 M_\odot$, i set to 35 deg, the gap width set to 0 R_{g} and R_{outer} set to 5000 R_{g}. We judge and compare the quality of the fit using the reduced chi-square test value χ^2_ν.

as

$$\Delta R = R_{\mathrm{gap\,out}} - R_{\mathrm{gap\,in}}, \tag{3.4}$$

$$\sigma_{\Delta R} = \sqrt{\sigma^2_{R_{\mathrm{gap\,out}}} + \sigma^2_{R_{\mathrm{gap\,in}}}}. \tag{3.5}$$

To infer the mass of the secondary component we use the eq. (2.10). The respective error term for the quantity is therefore

$$M_2 = 3M_1 \left(\frac{\Delta R}{2d}\right)^3, \tag{3.6}$$

$$\sigma_{M_2} = \sqrt{\left(3M_1 \frac{3\Delta R^2}{8d^3}\right)^2 \sigma^2_{\Delta R} + \left(3M_1 \frac{\Delta R^3}{8} \frac{-3}{d^4}\right)^2 \sigma^2_d}. \tag{3.7}$$

To translate our choice of errors in the measured flux to the difference of the magnitude of the source we start from the flux-magnitude relation and write

$$m_1 = -2.5 \log(F_1) + const. \tag{3.8}$$

After a slight change in the value of the measure flux corresponding to the factor p, namely as $F_2 = (1 \pm p)F_1$, we write

$$m_2 = -2.5 \log(F_2) + const. \tag{3.9}$$

assumed values			fit values			
$E(B-V)$	$\dot{m}$	$R_{\rm ADAF}$ ($R_{\rm g}$)	$E(B-V)$	$\dot{m}$	$R_{\rm ADAF}$ ($R_{\rm g}$)	χ^2_ν
z=0						
0.15	0.4	11	0.18 ± 0.04	0.45 ± 0.05	6 ± 10	1.3
0.15	0.4	25	0.16 ± 0.03	0.41 ± 0.03	21 ± 8	1.1
z=0.5						
0.15	0.4	11	0.17 ± 0.02	0.42 ± 0.03	8 ± 4	1.2
0.15	0.4	25	0.16 ± 0.02	0.42 ± 0.03	24 ± 3	1.1
z=1						
0.15	0.4	11	0.14 ± 0.02	0.37 ± 0.04	12 ± 2	1.4
0.15	0.4	25	0.15 ± 0.02	0.38 ± 0.03	25 ± 1	1.1
z=1.5						
0.15	0.4	11	0.14 ± 0.01	0.36 ± 0.04	10 ± 1	1.2
0.15	0.4	25	0.17 ± 0.01	0.44 ± 0.04	25 ± 1	1.1
z=2						
0.15	0.4	11	0.16 ± 0.01	0.44 ± 0.04	11 ± 1	1.1
0.15	0.4	25	0.13 ± 0.01	0.33 ± 0.03	24 ± 1	1.2

Table 3.3: Fitting results of data simulated for dust model component (altered Scenario I). The errors correspond to 10% in the measured flux. Each row for the particular mock data shows the assumed values of the simulation and fitting results obtained for a given redshift z of the source. The fixed parameters are as follows: M_1 to set $10^9 M_\odot$, i set to 35 deg, the gap width set to 0 $R_{\rm g}$ and $R_{\rm outer}$ set to 5000 $R_{\rm g}$. We judge and compare the quality of the fit using the reduced chi-square test value χ^2_ν.

The difference in magnitude is essentially equal to the difference of the flux in log-scale, and therefore we quantify the error terms in the flux via the magnitude by the following relation as

$$\Delta m = m_2 - m_1 = -2.5 \log(1 \pm p) \approx -2.5 \times 0.42 \ln(1 \pm p) \approx \mp p, \tag{3.10}$$

simplifying the $\log \approx 0.42 \ln$ and using the Maclaurin series expansion for the $\ln(1 \pm p)$.

3.2.3 QUVIK mission incorporation

We will now describe the outlook of the upcoming new instruments that are relevant in the context of spectra modelling presented in this thesis. In particular, we have focused on the upcoming mission QUVIK, which is supposed to be the first Czech space telescope and expected to be launched in 2028. The satellite development is led by the Czech Aerospace Research Centre with the science program from various academic institutions (Werner and et al., 2022; Werner et al., 2024). Because of immediate relevance to the subject of this thesis, we have explored what predictions and constraints to the planned observational strategy

assumed values			fit values								inferred values	
$\dot{m}$	$R_{\rm gap\,in}$ ($R_{\rm g}$)	$R_{\rm gap\,out}$ ($R_{\rm g}$)	$\dot{m}$	$R_{\rm gap\,in}$ ($R_{\rm g}$)	$R_{\rm gap\,out}$ ($R_{\rm g}$)	χ^2_ν	AIC	BIC	$\Delta\ AIC$	$\Delta\ BIC$	d ($R_{\rm g}$)	M_2 ($10^7 M_\odot$)
z=0												
0.4	170	230	0.43 ± 0.05	166 ± 55	254 ± 75	1.5	9.3	11.6	–	–	210 ± 47	2.76 ± 8.94
0.4	170	170	0.36 ± 0.02	–	–	1.6	8.3	9.1	–1	–2.5	–	–
0.4	340	460	0.41 ± 0.04	292 ± 106	453 ± 148	1.4	8.4	10.7	–	–	373 ± 91	3.03 ± 10.51
0.4	340	340	0.35 ± 0.02	–	–	1.8	10.5	11.2	2.1	0.5	–	–
0.4	680	920	0.38 ± 0.02	767 ± 327	1080 ± 507	1.3	6.7	9	–	–	923 ± 302	1.46 ± 8.57
0.4	680	680	0.35 ± 0.01	–	–	1.4	6.5	7.3	–0.2	–1.7	–	–
z=0.5												
0.4	170	230	0.45 ± 0.04	133 ± 32	234 ± 48	1.2	5.4	7.7	–	–	184 ± 29	6.26 ± 11.12
0.4	170	170	0.36 ± 0.02	–	–	2	11.9	12.7	6.5	5	–	–
0.4	340	460	0.42 ± 0.03	367 ± 124	600 ± 248	1.5	9.4	11.7	–	–	484 ± 139	4.20 ± 15.41
0.4	340	340	0.38 ± 0.02	–	–	2	12.1	12.9	2.7	1.2	–	–
0.4	680	920	0.42 ± 0.02	586 ± 269	813 ± 424	1.3	7.2	9.5	–	–	700 ± 251	1.28 ± 8.62
0.4	680	680	0.40 ± 0.02	–	–	1.4	5.8	6.6	–1.4	–2.9	–	–
z=1												
0.4	170	230	0.43 ± 0.03	127 ± 31	229 ± 55	1.4	7.9	10.2	–	–	178 ± 32	7.06 ± 13.63
0.4	170	170	0.36 ± 0.02	–	–	2.6	16.3	17.1	8.4	6.9	–	–
0.4	340	460	0.39 ± 0.02	332 ± 171	443 ± 270	1.1	4.6	7	–	–	388 ± 160	0.88 ±7.69
0.4	340	340	0.37 ± 0.01	–	–	1.2	3.5	4.2	–0.6	–2.8	–	–
0.4	680	920	0.42 ± 0.02	875 ± 700	1436 ± 963	1.2	5.2	7.5	–	–	1156 ± 595	4.29 ± 28.12
0.4	680	680	0.41 ± 0.02	–	–	1.6	8.5	9.2	3.3	2.7	–	–

Table continued on the next page.

assumed values			fit values								inferred values	
$\dot{m}$	$R_{\mathrm{gap\,in}}$ (R_{g})	$R_{\mathrm{gap\,out}}$ (R_{g})	$\dot{m}$	$R_{\mathrm{gap\,in}}$ (R_{g})	$R_{\mathrm{gap\,out}}$ (R_{g})	χ^2_ν	AIC	BIC	Δ AIC	Δ BIC	d (R_{g})	M_2 ($10^7 M_\odot$)
z=1.5												
0.4	170	230	0.43 ± 0.02	118 ± 34	193 ± 59	1.3	6.6	8.9	–	–	156 ± 34	4.21 ± 11.79
0.4	170	170	0.37 ± 0.02	–	–	2.1	12.9	13.7	6.3	4.8	–	–
0.4	340	460	0.40 ± 0.02	325 ± 137	448 ± 220	1.1	3.6	6	–	–	387 ± 130	1.21 ± 7.74
0.4	340	340	0.39 ± 0.01	–	–	1.1	2.4	3.2	–1.2	–2.8	–	–
0.4	680	920	0.41 ± 0.02	569 ± 287	1160 ± 462	1.1	3.9	6.2	–	–	865 ± 272	11.98 ± 34.96
0.4	680	680	0.39 ± 0.02	–	–	2.1	13.2	14	9.3	7.8	–	–
z=2												
0.4	170	230	0.38 ± 0.02	86 ± 88	100 ± 101	1.6	9.7	12	–	–	93 ± 67	0.13 ± 3.69
0.4	170	170	0.36 ± 0.01	–	–	1.4	6.7	7.5	–3	–4.5	–	–
0.4	340	460	0.40 ± 0.02	276 ± 73	497 ± 137	1.2	5.3	7.6	–	–	387 ± 78	7.01 ± 15.37
0.4	340	340	0.38 ± 0.01	–	–	1.6	8	8.8	2.7	1.2	–	–
0.4	680	920	0.39 ± 0.02	322 ± 126	505 ± 189	1.2	6.2	8.5	–	–	414 ± 114	3.25 ± 12.40
0.4	680	680	0.38 ± 0.01	–	–	1.4	6.3	7.1	0.1	–1.4	–	–

Table 3.4: Fitting results of data simulated for the secondary black hole component (Scenario II). The errors correspond to 10% in the measured flux. For the particular mock data each row shows the assumed values of the simulation and the corresponding fitting results obtained for a given redshift z of the source. The fixed parameters are as follows: M_1 set to $10^9 M_\odot$, i set to 35 deg, R_{inner} set to $6R_{\mathrm{g}}$ and R_{outer} to 5000 R_{g}, unless stated otherwise. We judge and compare the quality of the fit using the reduced chi-square test value χ^2_ν, Akaike AIC and Bayesian Information Criteria BIC in the corresponding columns. We also provide the calculated values of the inferred parameters d and M_2 of the perturber and their error terms when possible.

assumed values			fit values								inferred values	
$\dot{m}$	$R_{\mathrm{gap\,in}}$ (R_{g})	$R_{\mathrm{gap\,out}}$ (R_{g})	$\dot{m}$	$R_{\mathrm{gap\,in}}$ (R_{g})	$R_{\mathrm{gap\,out}}$ (R_{g})	χ^2_ν	AIC	BIC	Δ AIC	Δ BIC	d (R_{g})	M_2 ($10^7 M_\odot$)
z=0												
0.4	170	230	0.40 ± 0.01	161 ± 14	220 ± 18	1.4	7.6	9.9	–	–	191 ± 11	1.12 ± 1.31
0.4	170	170	0.35 ± 0.01	–	–	4.4	24.5	25.3	16.9	15.4	–	–
0.4	340	460	0.40 ± 0.01	342 ± 43	449 ± 53	1.4	8.5	10.8	–	–	396 ± 34	0.75 ± 1.44
0.4	340	340	0.36 ± 0.01	–	–	6.3	30.4	31.2	21.9	20.4	–	–
0.4	680	920	0.39 ± 0.01	658 ± 97	834 ± 130	1.5	8.9	11.2	–	–	746 ± 81	0.49 ± 1.37
0.4	680	680	0.37 ± 0.01	–	–	4.9	26.3	27.1	17.4	15.9	–	–
z=0.5												
0.4	170	230	0.41 ± 0.01	157 ± 12	222 ± 15	1	2.7	5	–	–	190 ± 10	1.52 ± 1.36
0.4	170	170	0.36 ± 0.01	–	–	9.2	36.5	37.3	33.8	32.3	–	–
0.4	340	460	0.367 ± 0.004	343 ± 32	472 ± 49	1	3.3	5.6	–	–	408 ± 29	1.19 ± 1.64
0.4	340	340	0.37 ± 0.01	–	–	9.3	36.6	37.4	33.3	31.8	–	–
0.4	680	920	0.398 ± 0.004	754 ± 95	982 ± 125	1.3	7.3	9.7	–	–	868 ± 79	0.68 ± 1.42
0.4	680	680	0.39 ± 0.01	–	–	3.9	22.6	23.3	15.3	13.6	–	–
z=1												
0.4	170	230	0.397 ± 0.005	182 ± 18	245 ± 26	1.2	5	7.3	–	–	214 ± 16	0.97 ± 1.47
0.4	170	170	0.37 ± 0.01	–	–	8.4	35.1	35.8	30.1	28.5	–	–
0.4	340	460	0.393 ± 0.005	383 ± 65	488 ± 94	2	13.8	16.1	–	–	436 ± 57	0.53 ± 1.73
0.4	340	340	0.38 ± 0.01	–	–	4.3	24.4	25.1	10.6	9	–	–
0.4	680	920	0.404 ± 0.004	690 ± 99	1024 ± 126	1.6	10.6	12.9	–	–	857 ± 80	2.22 ± 3.26
0.4	680	680	0.39 ± 0.01	–	–	7.9	34	34.8	23.4	21.9	–	–

Table continued on the next page.

assumed values			fit values								inferred values	
$\dot{m}$	$R_{\mathrm{gap\,in}}$ (R_{g})	$R_{\mathrm{gap\,out}}$ (R_{g})	$\dot{m}$	$R_{\mathrm{gap\,in}}$ (R_{g})	$R_{\mathrm{gap\,out}}$ (R_{g})	χ^2_ν	AIC	BIC	Δ AIC	Δ BIC	d (R_{g})	M_2 $(10^7 M_\odot)$
z=1.5												
0.4	170	230	0.396 ± 0.004	180 ± 17	247 ± 27	1.2	5	7.3	–	–	214 ± 16	1.16 ± 1.68
0.4	170	170	0.37 ± 0.01	–	–	8.6	35.5	36.2	30.5	28.9	–	–
0.4	340	460	0.398 ± 0.004	365 ± 52	469 ± 72	1.6	10.1	12.4	–	–	417 ± 44	0.58 ± 1.50
0.4	340	340	0.388 ± 0.005	–	–	3.6	21.3	22.1	11.2	9.7	–	–
0.4	680	920	0.397 ± 0.003	664 ± 178	880 ± 211	1.3	6.9	9.2	–	–	772 ± 138	0.82 ± 3.18
0.4	680	680	0.39 ± 0.01	–	–	4.7	25.7	26.4	18.8	17.2	–	–
z=2												
0.4	170	230	0.394 ± 0.004	152 ± 16	202 ± 25	1.2	5.1	7.4	–	–	177 ± 15	0.85 ± 1.52
0.4	170	170	0.37 ± 0.01	–	–	7	32.2	33	27.1	25.6	–	–
0.4	340	460	0.394 ± 0.004	344 ± 59	412 ± 71	1.1	3.5	5.8	–	–	378 ± 46	2.19 ± 0.90
0.4	340	340	0.388 ± 0.003	–	–	2	12.1	12.9	8.6	7.1	–	–
0.4	680	920	0.398 ± 0.003	771 ± 493	962 ± 600	1.3	7	9.3	–	–	867 ± 388	4.15 ± 4.93
0.4	680	680	0.394 ± 0.005	–	–	3.7	22	22.7	15	13.4	–	–

Table 3.5: Fitting results of data simulated for the secondary black hole model component (Scenario II). The errors correspond to 2% in the measured flux. For the particular mock data each row shows the assumed values of the simulation and the corresponding fitting results obtained for a given redshift z of the source. The fixed parameters are as follows: M_1 set to $10^9 M_\odot$, i set to 35 deg, R_{inner} set to $6R_{\mathrm{g}}$ and R_{outer} set to 5000 R_{g}, unless stated otherwise. We judge and compare the quality of the fit using the reduced chi-square test value χ^2_ν, Akaike AIC and Bayesian Information Criteria BIC in the corresponding columns. We also provide the calculated values of the inferred parameters d and M_2 of the perturber and their error terms when possible.

can be achieved in the context of AGN with “gappy” accretion discs.[1]

The telescope in itself is an agile, small-sized instrument with the limiting observing magnitude up to ≈ 22, given the S/N ratio ≈ 5. The major utilization of the QUVIK telescope would be pointing towards the optical/UV observations corresponding to 150 and 300 nm, FUV and NUV filters, respectively.

The QUVIK mission is supposed to be primarily used as an instrument for follow up observations of kilonovae observations and serve as a valuable tool for the gravitational wave detectors in the spectral domain (see Werner and et al., 2023). Nevertheless, the detector’s UV band coverage is expected to provide observational data on the stellar systems, as well as the dust enshrouding of the objects, hot spots, etc. (see Krtička and et al., 2023). Finally, the mission will inevitably be helpful when focusing on the galactic centre. With the help of reverberation mapping the QUVIK can be of help with the temporal analysis and complementary to other waveband observation. Moreover, the instrument will be efficient in the study of jetted TDEs and more exotic changing-look sources, or gappy accretion disc scenarios as well.

In the White Paper introduction article Zajaček et al. (2024) we show possible QUVIK mission application in the area of gappy accretion disc study. The study specifically focuses on systems corresponding to the Scenarios I, altered Scenario I and Scenario II. The physical conditions of the system remain unchanged, i.e. see subsection 3.1. Essentially we only replace the FUV and NUV filters of the GALEX observation instrument with the QUVIK’s (for comparison see Tables 3.1and 3.6, respectively). Although with different geometrical scaling we arrive at the qualitative same results for the simulations/fitting in Scenario I, altered Scenario I and Scenario II, both for errors 2% and 10%. In short, the Scenario I and altered Scenario I results do not discriminate between the changes in the errors in measured flux as opposed to the Scenario II results that require higher precision observations. For completeness we show in the Appendix A the fit results for the simulations involving the change from GALEX to QUVIK for the Scenario I, its altered version and the Scenario II for both errors 2% and 10%, unless stated otherwise (see Tables A.1 - A.4, respectively). Given the fact we only changed two of the 16 points of our mock data (change from GALEX to QUVIK) the fit results do not show any major qualitative difference and are effectively consistent with the finding mentioned in the subsection 3.2.1.

As mentioned in the the subsection 3.1, the current detector AstroSat/UVIT is capable of providing data with better S/N ratio as well. Another alternative would be the UVEX3 detector, which is comparing to GALEX detector approximately two orders of magnitude more sensitive and is essentially covering the same energy range. The ULTRASAT telescope, planned to be launched in the 2026, belongs to the family of small sized detectors such as QUVIK, and will be focusing on the optical as well as near- and far-UV observations Ben-Ami and et al. (2022). In the frame of the simultaneous observations the mentioned detectors complemented by their parameters and observational abilities pose a viable option to map the gappy systems in the near future.

---

[1] Here the abbreviation in somewhat technical jargon refers exactly to the case of disc-type accretion flow that is interrupted by forming azimuthal gaps at certain specific radii that have been cleared due to the influence of perturbers or by other means.

Instrument	Filter	Central Wavelength (Å)
QUVIK	FUV	1500
	NUV	3000
LSST	u	3671
	g	4827
	r	6223
	i	7546
	z	8691
	y	9712
SWIFT	uvw2	1928
	uvm2	2246
	uvw1	2600
	u	3465
	b	4392
	v	5468
WISE	w1	33680
	w2	46180

Table 3.6: Photometry table listing the alternative set of observational instruments (compared to Table 3.1), alongside their respective parameters such as the filter and the central wavelength.

3.3 Spectral line profiles

Complementary to the simulations of the thermal component of the system we focus on the spectral line profile feature assuming both Scenario I and III. In both scenarios there is a central cavity present, which is a direct result of the central region filled with the highly ionized matter. That is the ADAF region which can be in this context treated as a corona. The highly ionized coronal radiation irradiates the cold slab material of the accretion disc, the radiation gets reprocessed and results in the emission line, whereas the strongest spectral emission line observed is the Fe Kα line. Depending on the geometry of corona, the reflected radiation follows its respective profile as a function of R (see subsection 2.7).

In Figure 3.14 we show the effects of the central cavity present in the Scenario I and keep varying its size, which is depending on the relative accretion rate $\dot{m}$ set to 0.4, 0.6 and 1.0 as per eq. (2.6). The spectral line profiles for both initial intensities of reflected radiation, $\approx 1/R^2$ and $\approx 1/R^3$, show major flux decrease as the size of the central cavity grows.

Adding the secondary black hole component to the mix, we show the spectral line profile simulations for Scenario III in Figure 3.15. For simplicity, we fix the secondary black hole component located at the distance of 50 R_{g}, corresponding to the gap opening of $15R_{\mathrm{g}}$, and we keep varying the size of the central cavity with the relative accretion rate $\dot{m}$ set to 0.4, 0.6 and 1.0 via eq. (2.6). The different initial intensities of reflected radiation show qualitatively the same features. We notice a clear decrease of flux in the perturbed scenarios due to the missing central region contribution. Also a distinctive feature arises and that is the double amount of peaks caused by the presence of the secondary body "splitting" the disc in two subdiscs.

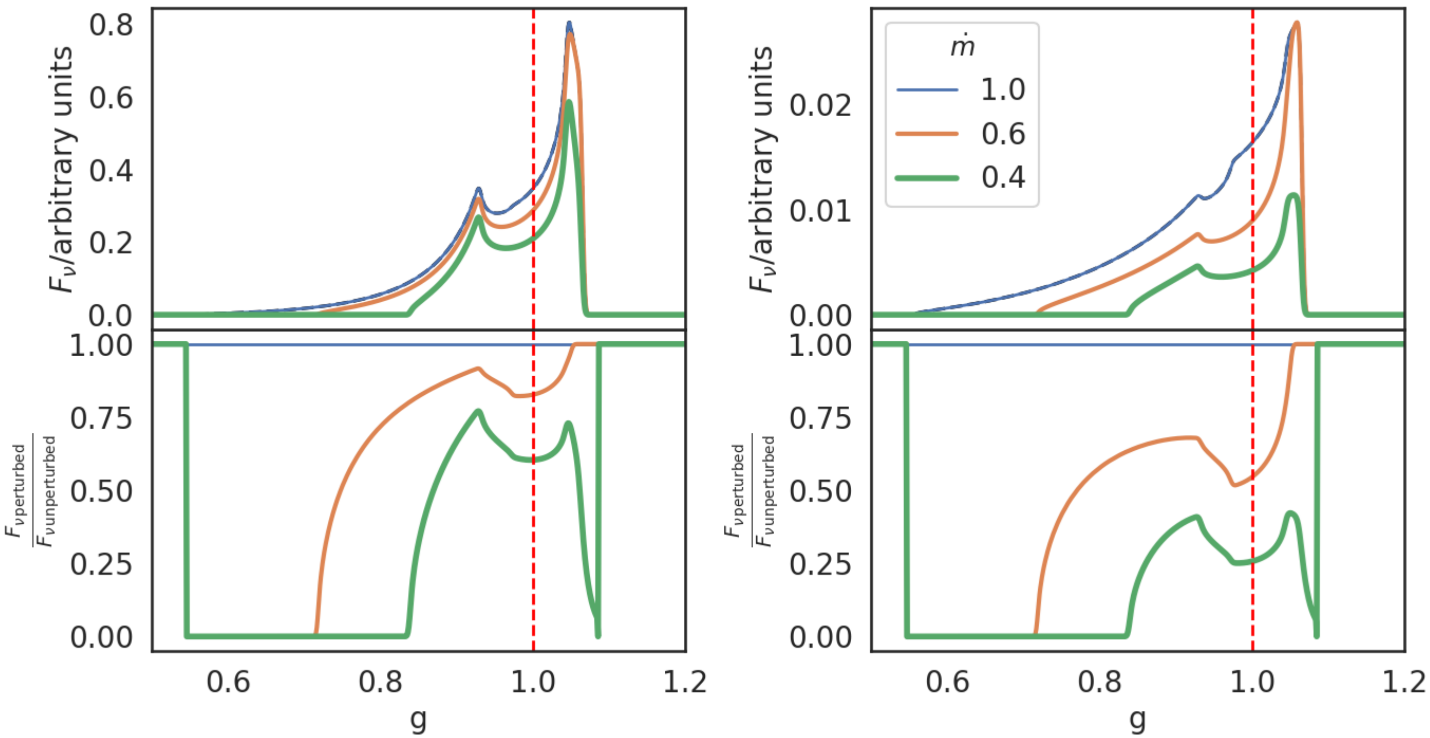

Figure 3.14: Theoretical spectral line profiles (background continuum subtracted) for two different forms of the initial emissivity with the reflected radiation as $\approx 1/R^2$ (*left panel*) and $\approx 1/R^3$ (*right panel*), corresponding to the model with varying relative accretion rate, and assuming strong ADAF principle (Scenario I). The energy units are scaled to the rest energy of 6.4 keV iron Fe Kα emission line. The solid blue thin line marks the unperturbed scenario, whereas the other solid colored lines mark the respective perturbed cases. The bottom row shows the ratio between the perturbed vs. unperturbed model, as described further in the text. The fixed parameters are as follows: the inclination angle i is set to 35deg.

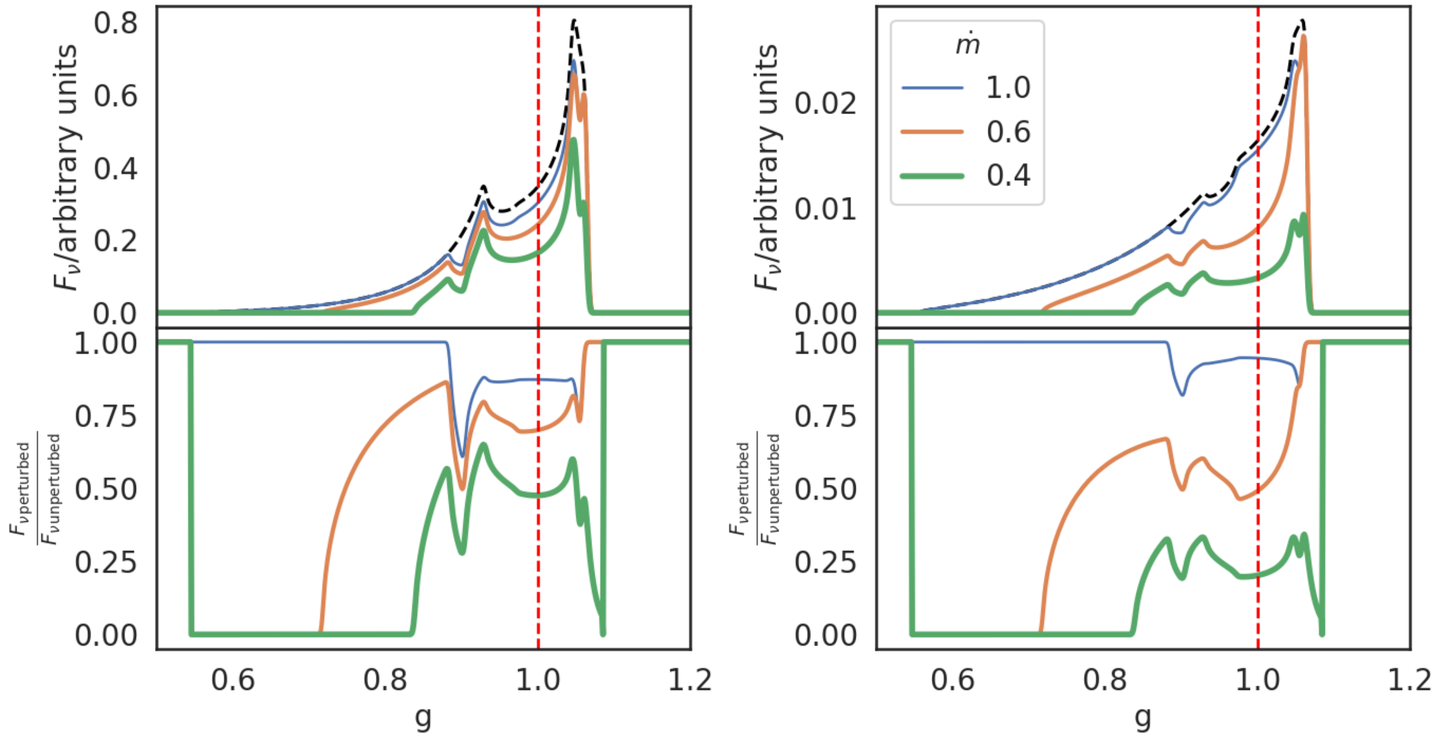

Figure 3.15: Theoretical spectral line profiles for two different initial emissivity with the reflected radiation as $\approx 1/R^2$ (*left panel*) and $\approx 1/R^3$ (*right panel*), corresponding to secondary black hole scenario coupled with varying relative accretion rate under the assumption of strong ADAF principle (Scenario III). The energy units are scaled to the rest energy of 6.4 keV iron Fe Kα emission line. The black dashed line marks the unperturbed scenario, whereas the other solid colored lines mark the respective perturbed cases. The bottom row shows the ratio between the perturbed vs. unperturbed model, as described further in the text. The fixed parameters are as follows: the inclination angle i is set to 35deg, the distance between the primary and the secondary body is set to $50R_{\rm g}$, corresponding to the gap width of $15R_{\rm g}$. The mass ratio of the secondary and primary is set to 10^{-2} with the mass of the primary $10^9 M_{\odot}$, and the mass of the secondary set to $10^7 M_{\odot}$.

4. Discussion

We have studied the effects of the following perturbative terms within the standard Shakura-Sunyaev thin disc scenario, and its ramification in the inner region (see Figure 3.1):

- The Scenario I involves the central region set up with the the highly ionized matter present, i.e. ADAF region (see subsection 2.3);
- The Scenario II involves the secondary component, namely SMBH, causing the gap formation under the circumstances discussed (subsection 2.5);
- Finally, the Scenario III features the central cavity alongside the secondary black hole component (see subsection 2.6).

Further we propose the altered version of the Scenario I by introducing the dust component enshrouding the whole system (see subsection 2.4). Therefore providing the spectral features to have the effects of intrinsic reddening. The caused effects are qualitatively similar to those caused by the central cavity in the Scenario I.

The study specifically focused on the spectral properties of thermal component of the observed radiation as well as the radiation from the X-ray radiation band. Now in the following subsections let us discuss the effects and their implications for both energy bands in more detail as well as layout the limitations of the systems given the respective scenarios (see the subsequent subsections 4.1, 4.2 and 4.3, respectively).

4.1 SED profiles

We have thoroughly studied the SED profiles assuming presence of different perturbers in the standard AGN system, mostly involving SMBH and the accretion disc around it. Let us discuss the single scenario one by one and point out the major results and possible implications.

The central cavity scenario, Scenario I, is a direct result of the highly ionized material filling the inner region of the accretion disc. With the power law with Γ-index 1.9 and the X-ray to UV relation (see eq. (2.7)), we have concluded the central cavity contribution is below 1% in the studied energy band and therefore the ADAF region does not radiatively contribute to the thermal component radiation of the disc itself (see Figure 3.2). The strong ADAF assumption, which is given by the eq. (2.6), intertwines the relative accretion rate with the size of the ADAF region, in our notion the central cavity region. Therefore once we simulate the system with that component present and keep changing the relative accretion rate $\dot{m}$ the accretion disc will be shrinking from the inside out (see left panel in Figure 3.4). Once we abandon the strong ADAF assumption we show the drastic flux decrease caused by the missing contribution of the inner region can be detected via 2 independent parameters, namely the relative accretion rate $\dot{m}$ and the size of the ADAF region. The Table 3.2 summarizes the fit results for the mock data corresponding to the Scenario I, adopting 10% errors in measured flux. The change of the fit results is almost negligible once the redshift of the source is incremented. However, we can see in Figures 3.2 and 3.9 that the higher redshift does better cover the central cavity effect.

The additional dust component in Scenario I is incorporated by the use of eq. (2.9). In this scenario we decouple the relative accretion rate $\dot{m}$ and the size of the ADAF region as well and add additional parameter extinction $E(B-V)$ devised by Czerny et al. (see 2004). We see the simple discontinuous effect of extinction (see Figure 2.3) translates into a very distinctive effect in the spectrum at specific wavelengths (see right panel in Figure 3.4). Fitting the mock data with 10% errors in the measure flux we clearly see that the central cavity and dust component effect can be decoupled. We observe that the higher redshift cases tend to cover the affected region more effectively and therefore the fit results are better for the higher adopted redshift values (see both SED plots and their perturbed/unperturbed ratios in Figures 3.10 and 3.11, respectively).

The Scenario II involves the secondary black hole and is essentially the case illustrating the galaxy merger scenario and its effects inflicted onto the thermal radiation (e.g. as in Gültekin and Miller, 2012). We have addressed the system stability in the previous sections (see subsection 3.1) and we have chosen the mass ratio secondary/primary to be equal to 0.01. Mass ratio such as this does not tamper with the system stability and is effectively providing big enough gap formation based on the flux decrease in the spectra. The gap width is essentially changing based on the distance of the primary and secondary as prescribed by the eq. (2.10). Based on Figure 3.5 we notice the decrease given via ratio perturbed/unperturbed is reaching maximum of $\approx$ 12%. We further notice the bigger the gap the more it is shifted to the lower energies as in the fixed mass ratio the gap with bigger size tends to form further away from the primary. Similarly as for the Scenario I and its altered version, we have attempted to fit the mock data for this setup to try to obtain the assumed values of the input parameters.

Furthermore, we attempted to fit the generated mock data in two different ways – with the gap parameters thawed and frozen for the system assuming the gap is either present or not, respectively. We see that for the assumed errors of 10% in measured flux the perturbed and unperturbed scenarios are almost indistinguishable, i.e. the fitting procedure can not based on the data and the given errors decipher which model is preferred (based on the reduced χ^2_ν test).

To compare between the perturbed and unperturbed models we have also utilized the ΔAIC and ΔBIC parameters. The results seem to ambiguous and the inferred values for the mass of the secondary and its distance of the primary show values with overestimated errors. Therefore we have lowered the assumed errors to 2% and we notice based on all three comparison methods χ^2_ν, ΔAIC and ΔBIC that the perturbed model is favoured and the inferred values of the parameters are far better restricted than for the 10% errors. This realization is not surprising given the flux decrease after the gap introduction is $\approx$ 12% and the errors of 10% simply shield the effect making it not visible for the fitting procedure. The 2% errors, however, allow the spectra to retain the perturbed shape, hence the better fit results and inferred values of input parameters. We see the redshift of the source plays a crucial role as for the wider gaps the high redshift cases are not captured by the mock data (see both the plots and the ratios in Figure 3.12 and 3.13, respectively).

Finally, let us address the simulations pertaining the combination of central cavity and secondary black hole component. We observe the effect of the secondary component is rather negligible (see left panel in Figure 3.6). Especially, if we keep the gap fixed, we notice the change of the central cavity size and the corresponding flux decrease can cause effective shielding of the secondary black hole effect (see right panel in Figure 3.6). The secondary black hole component is effectively causing $\approx 12\%$ flux decrease. We also attempted to replace the central cavity with the dust component. The spectra do not qualitatively differ in this case except for the slight changes in the shape. We again observe the secondary black hole effect is overlapped by the drastic flux decrease due to the dust component present. Specifically, the bigger the extinction, the lower the chance for the spectra to fully manifest the gap effect (for comparison see both panels in Figure 3.7, respectively). The dust component effect on the spectra is, however, more distinctive due to the discontinuity introduced by the extinction parameter (see eq. (2.8)).

The Scenario II, Scenario III and its altered version both essentially illustrate the galactic merger scenario. To study such system and its spectral properties we have chosen the parameters M_2 and the distance of the secondary d so that the merging timescale is $\gtrsim 10^4\,yr$ (see subsection 2.5).

4.2 Spectral line profiles

The additional spectral line profile study has been conducted for the following Scenarios II and III. To cover the radiative properties in the strong gravity regime we focus on the accretion disc's inner region up to $\sim 100\ R_{\mathrm{g}}$. This means that once we introduce the secondary black hole component, we essentially study the late stage galaxy merger scenario with the merging timescale $\lesssim 10^4\,yr$.

As both scenarios involve the central cavity caused by the ADAF component we observe noticeable flux decrease (see Figure 3.14 and 3.15). We have implemented two different initial intensities of the reflected radiation based on the geometry of corona in respect to the accretion disc (R/R_{c} ratio). Besides the different shape of the spectral line there are no additional qualitative changes for the $\approx 1/R^2$ and $\approx 1/R^3$ intensities (for R/R_{c} ratio ≈ 1 and > 1, respectively).

Introducing the gap inducing component we notice the spectral line profile to exhibit the doubled amount of peaks (see Figure 3.15). That is a direct results of the superposed radiation of the subdisc from the gap downwards and upwards, respectively. Specifically, for N gaps one can expect the spectral line profile to show $2(N+1)$ peaks (see e.g. Štolc et al., 2020, and references therein). That is in agreement with the simulations made previously by Sochora et al. (2011) and McKernan et al. (2013). The slight flux decrease caused by the secondary component is effectively shielded by the central cavity effect. The reason for that is that the missing reflection medium of the gap region by the secondary component is of negligible size compared to that of ADAF region. Nevertheless, the spectral line profile properties could potentially enable to perform analysis of such systems, unless the size of the ADAF region is not greater than or equal to the secondary component's distance from primary.

4.3 Limitations of the proposed system setups

The use of ADAF component is a bit tricky as there are more parameters that need to be addressed such as thermal conduction and magnetic field, which consequently lead to different relations than used in eq. (2.6). Also, there are observation, such as NGC 3147 with the relative accretion rate of $\dot{m} = 10^{-4}$, which do not exhibit the ADAF component as predicted via the eq. (2.6), but instead there is a standard disc present (Bianchi et al., 2019). We also use the no-torque condition setting the $R_{\rm inner}$ of the disc equal to the $R_{\rm ADAF}$ directly, unless stated otherwise (scenarios without ADAF component present), keeping the set of proposed parameters intact. We show the additional dust component can lead to plus one parameter in the model. However, the results are promising and show possible disentanglement in the simulated spectra. Consequently, we contemplate the possibility to differentiate between the Scenario I and its altered version and the possible tidal disruption scenario having qualitatively similar effect of flux decrease due to the inner disc depletion (e.g. Ricci et al., 2020). For that to happen the model parameters would need to be adjusted accordingly as well.

Another simplification is the analytical approach to calculate both the SED and the spectral line profile line profiles. The MHD approach would allow to formulate the geometry boundaries of the disc more accurately, i.e. indicate both black holes to have their own mini disc surrounding it (e.g. Farris et al., 2015). Furthermore, the MHD simulations would allow for the the potential study of even more exotic cases such as supernovae immersed in the orbital plane of the accretion disc. That kind of simulations would indicate the expected size of the gap generated by such event in the order of 0.01pc (see e.g. Moranchel-Basurto et al., 2021).

As we have already mentioned the study of spectral properties in the introduced system is prone to several simplifications. The major initial limitation is the zero angular momentum state of the central body. In the case of the study of the SED spectra, the zero and nonzero spin hold essentially the same information as the gap formation is essentially happening above $\approx 100 R_{\rm g}$. The rotation effect would make itself the most visible in the case of the spectral line profile study, conducted below $\approx 100 R_{\rm g}$, as the strong gravity regime would require to use of adjusted formulation of the redshift factor incorporating spin compared to eq. (2.18).

Last but not least there is a accretion disc's stability issue given the specific system setup. The accretion disc tends to get unstable when we move from gappy scenario to ring-like scenario. In the gappy scenario the majority of the surface is covered by the accretion disc's material and assuming the orbital period of the perturber to be less than the viscous timescale of the disc the scenario is stable. On the contrary, whereas in the ring-like scenario is the accretion disc effectively replaced by the set of concentric rings. Each ring's material is essentially diffusing via eq. (1.28) and the ring-like structure will dissolve (e.g.

Frank et al., 2002). Moreover, the ring-like scenario necessitates with the presence of multiple perturbers which cannot be solved analytically only approximately, e.g. 3-body problem and its special case solutions.

The final limitation of the proposed scenarios is the observability issue as shown for the Scenario I, its altered version and Scenario II. In our research we have developed the approach to infer the system parameters based on the mock data from a list of detectors (see Tables 3.1 and 3.6). The simultaneous action of the detectors is conducted for the optical/UV and is essentially prone to spectral variabilities over the observational timescale. Nevertheless, we propose a rather crude simplification by stating the observed objects show no major signs of radiation changes during the time of joined observation cycle (see more in subsection 3.2.1).

5. Conclusions and future prospects

Black holes have been introduced as one of the predictions of the Theory of General Relativity in the regime of the strong gravitational field. To the great surprise of many scientists, it turned out that this elegant mathematical solution of the equations of theoretical physics has been most likely discovered by astronomers in numerous objects in the Universe. They are surrounded by a gaseous environment, often in the form of accretion flows which they can convert into very efficient outflows and collimated jets, where a fraction of captured material is returned to the cosmic environment together with spectacular signatures in the form of electromagnetic and gravitational radiation.

Electromagnetic radiation originating from inner regions of accretion discs around black holes, either in stellar-mass black hole binaries or in active galactic nuclei (AGNs), provides wealth of information about matter in extreme conditions close to the event horizon. Multi-temperature thermal continuum emission of an accretion disc combined with the induced spectral feature and non-thermal radiation of the surrounding corona produce the final signal propagating through the regions of strong gravity towards a distant observer. Parameters of the models are thus imprinted in the Spectral Energy Distribution (SED), which gives us chance to determine the geometry of the system and the state of the cosmic environment near black holes.

In this thesis, we explored the expected spectral signatures of a non-standard SED corresponding to the black-hole accretion disc with a central cavity, dust component and/or a gap caused by a secondary perturber. The latter is thought to represent an intermediate-mass black hole. Assuming the radiation signal originating from inner regions of an accretion disc near a black hole, we examined the possibility to detect minor deviations of the spectral shape with respect to an unperturbed model, thus revealing the presence of the orbiter. We considered the perturber mass of the order of $10^7\ M_\odot$, so that a gap can open within the accretion disc, and we took into account a possibility of a truncated accretion flow that terminates well above the ISCO. In the present work we neglected a number of potential complications that should be taken into account in future astrophysically more realistic models, such as the effect of self-gravity of the accretion disc and its non-negligible vertical height.

The main results of the presented thesis were focused on the SED profile that can be expected and observationally identified in the multi-wavelength continuum profile, ranging from ultraviolet over optical up to X-ray domain. We have focused on the case of black-hole accretion disc with an emissivity profile modified by non-standard radial dependence. In particular, we described the theoretical basis for the formation of gaps in the accretion disc caused by the action of a secondary perturber orbiting the central supermassive black hole (SMBH). The resulting spectral features reach beyond the expectation of the standard (Shakura-Sunyaev) multi-blackbody spectrum superposed with a simple (power law) component due to corona. We have explored, in a rather fine detail, the predicted deviations from the unperturbed baseline model that will be detectable with the upcoming space satellite experiments, such as recently approved QUVIK (Quick Ultra-Violet Kilonovae surveyor) in the UV band.

Let us point out that the synergy of X-ray and UV spectral domains appears to be particularly promising in the context of future applications of our results from the thesis. Very recent discoveries of Quasi-Periodic Eruptions (QPEs; Miniutti et al., 2019), an enigmatic and as yet unexplained phenomenon of repetitive X-ray signal from nuclei of some active galaxies, can be tentatively understood in terms of secondary orbiting bodies transiting across and accretion disc and modulating the emerging signal (Suková et al., 2021; Linial and Metzger, 2023). It is quite likely that the family of galactic nuclei with quasi-periodic behaviour may be rather diverse. A related phenomenon of Quasi-Periodic Outflows (QPOuts; Pasham et al., 2024b) has been very recently described as an intermediate-mass black hole interacting with a magnetized accretion flow (Suková et al., 2023). A broader class of Repeating Nuclear Transients (RNTs) could be interpreted in terms of partial Tidal Disruption Events (TDEs; Liu et al., 2023; Miniutti et al., 2023a,b). However, the question about the true origin of these objects still remains open (Pasham et al., 2024a).

It has been proposed that some of these quasi-periodicities could be detected via the upcoming UV satellites that are currently at different stages of development (Zajaček et al., 2024). Combining the X-ray and UV domains will help us to constrain the physical mechanisms operating in these new classes of objects (Linial and Metzger, 2024). However, an inevitably forming population of orbiters aligned with the accretion flow has not been duly explored with this scenario and it urgently needs to be modelled and its consequences understood. Consequences for future detection of Extreme-Mass Ratio Inspirals (EMRIs) and related events seen in the gravitational-wave domain also emerge as an exciting new direction (Arcodia et al., 2024; Guolo et al., 2024; Zhou et al., 2024; Chakraborty et al., 2024). There is no doubt about a huge potential of further development of the ideas that have been just outlined in our thesis.

Finally, in the future work we intend to superpose the above-described perturbed SED broadband continuum profiles with the most prominent spectral-line features that can be expected especially in the X-ray domain. In this context, the iron line complex between 6–7 keV appears as a promising additional feature that may help to constrain the model parameters with significantly greater precision than just continuum SED. So far we have only very briefly touched the effect of the iron line emission around the rest-frame energy of 6.4 keV that belongs among the most frequently studied emission feature originating from the innermost (relativistic) regions of the accretion flow. A combination of broad-band spectral profiles and well defined emission lines will provide valuable constraints of the model parameters that cannot be inferred from continuum. We have shown the anticipated effects that we expect to be relevant in the context of upcoming X-ray observations, such as the ATHENA in its recently updated formulation. A more detailed study of the source will be required specifically in terms of adding more parameters to the models, such as spin of the central object in terms of full regime of General Relativity, and different inclination angles for the inner and outer sub-disc due to Bardeen-Petterson effect.

Bibliography

Abadie, J., Abbott, B. P., Abbott, R., and et al. (2012). Search for gravitational waves from low mass compact binary coalescence in LIGO's sixth science run and Virgo's science runs 2 and 3, keywords = 04.30.Db, 04.80.Cc, Wave generation and sources, Experimental tests of gravitational theories, General Relativity and Quantum Cosmology. *Physical Review D*, 85(8):082002.

Abramowicz, M. A., Chen, X., Kato, S., Lasota, J.-P., and Regev, O. (1995). Thermal Equilibria of Accretion Disks. *Astrophysical Journal, Letters*, 438:L37.

Abramowicz, M. A., Czerny, B., Lasota, J. P., and Szuszkiewicz, E. (1988). Slim Accretion Disks. *The Astrophysical Journal*, 332:646.

Akaike, H. (1973). *Information Theory and an Extension of the Maximum Likelihood Principle*, pages 199–213. Springer New York, New York, NY.

Albright, G. E. and Richards, M. T. (1996). Doppler Tomography of Accretion Disks in Algol Binaries. *The Astrophysical Journal Letters*, 459:L99.

Antonucci, R. (1993). Unified models for active galactic nuclei and quasars. *ARA&A*, 31:473–521.

Arcodia, R., Liu, Z., Merloni, A., Malyali, A., Rau, A., Chakraborty, J., Goodwin, A., Buckley, D., Brink, J., Gromadzki, M., Arzoumanian, Z., Buchner, J., Kara, E., Nandra, K., Ponti, G., Salvato, M., Anderson, G., Baldini, P., Grotova, I., Krumpe, M., Maitra, C., Miller-Jones, J. C. A., and Ramos-Ceja, M. E. (2024). The more the merrier: SRG/eROSITA discovers two further galaxies showing X-ray quasi-periodic eruptions. *arXiv e-prints*, page arXiv:2401.17275.

Artymowicz, P. (1994). Orbital Evolution of Bodies Crossing Disks Due to Density and Bending Wave Excitation. *ApJ*, 423:581.

Balbus, S. A. and Hawley, J. F. (1991). A Powerful Local Shear Instability in Weakly Magnetized Disks. I. Linear Analysis. *The Astrophysical Journal*, 376:214.

Balbus, S. A. and Mummery, A. (2018). The evolution of Kerr discs and late-time tidal disruption event light curves. *Monthly Notices of the Royal Astronomical Society*, 481(3):3348–3356.

Bambi, C. (2017). *Black Holes: A Laboratory for Testing Strong Gravity.* Springer.

Bandopadhyay, A., Fancher, J., Athian, A., Indelicato, V., Kapalanga, S., Kumah, A., Paradiso, D. A., Todd, M., Coughlin, E. R., and Nixon, C. J. (2024). The Peak of the Fallback Rate from Tidal Disruption Events: Dependence on Stellar Type. *ApJL*, 961(1):L2.

Bardeen, J. M., Carter, B., and Hawking, S. W. (1973). The four laws of black hole mechanics. *Communications in Mathematical Physics*, 31(2):161–170.

Bardeen, J. M., Press, W. H., and Teukolsky, S. A. (1972). Rotating Black Holes: Locally Nonrotating Frames, Energy Extraction, and Scalar Synchrotron Radiation. *Astrophysical Journal*, 178:347–370.

Ben-Ami, S. and et al. (2022). The scientific payload of the Ultraviolet Transient Astronomy Satellite (ULTRASAT). In den Herder, J.-W. A., Nikzad, S., and Nakazawa, K., editors, *Space Telescopes and Instrumentation 2022: Ultraviolet to Gamma Ray*, volume 12181 of *Society of Photo-Optical Instrumentation Engineers (SPIE) Conference Series*, page 1218105.

Bianchi, S., Antonucci, R., Capetti, A., Chiaberge, M., Laor, A., Bassani, L., Carrera, F. J., La Franca, F., Marinucci, A., Matt, G., Middei, R., and Panessa, F. (2019). HST unveils a compact mildly relativistic broad-line region in the candidate true type 2 NGC 3147. *Monthly Notices of the RAS*, 488(1):L1–L5.

Blandford, R. D. and Znajek, R. L. (1977). Electromagnetic extraction of energy from Kerr black holes. *Monthly Notices of the Royal Astronomical Society*, 179:433–456.

Bondi, H. (1952). On spherically symmetrical accretion. *Monthly Notices of the Royal Astronomical Society*, 112:195.

Chakrabarti, S. K. (1990). *Theory of Transonic Astrophysical Flows*. World Scientific Publishing Company.

Chakraborty, J., Arcodia, R., Kara, E., Miniutti, G., Giustini, M., Tetarenko, A. J., Rhodes, L., Franchini, A., Bonetti, M., Burdge, K. B., Goodwin, A. J., Maccarone, T. J., Merloni, A., Ponti, G., Remillard, R. A., and Saxton, R. D. (2024). Testing EMRI models for Quasi-Periodic Eruptions with 3.5 years of monitoring eRO-QPE1. *arXiv e-prints*, page arXiv:2402.08722.

Collier, S. and Peterson, B. M. (2001). Characteristic Ultraviolet/Optical Timescales in Active Galactic Nuclei. *Astrophysical Journal*, 555(2):775–785.

Collin, S., Abrassart, A., Czerny, B., Dumont, A. M., and Mouchet, M. (2001). Accretion and emission processes in AGN: the UV-X connection. In Rocca-Volmerange, B. and Sol, H., editors, *EAS Publications Series*, volume 1 of *EAS Publications Series*, pages 35–51.

Coughlin, E. R. and Nixon, C. J. (2022). A simple and accurate prescription for the tidal disruption radius of a star and the peak accretion rate in tidal disruption events. *MNRAS*, 517(1):L26–L30.

Cunningham, C. (1976). Returning radiation in accretion disks around black holes. *The Astrophysical Journal*, 208:534–549.

Czerny, B. (2019). Slim Accretion Disks: Theory and Observational Consequences. *Universe*, 5(5):131.

Czerny, B., Li, J., Loska, Z., and Szczerba, R. (2004). Extinction due to amorphous carbon grains in red quasars from the Sloan Digital Sky Survey. *Monthly Notices of the RAS*, 348(3):L54–L57.

Czerny, B., Różańska, A., Janiuk, A., and Życki, P. T. (2000). Disk/corona model: The transition to ADAF. *New Astronomy Review*, 44(7-9):439–441.

De Angelis, A. and Pimenta, M. (2018). *Introduction to Particle and Astroparticle Physics*. Springer.

de Grijs, R. and González Delgado, R. M. (2005). *Starbursts: From 30 Doradus to Lyman Break Galaxies*, volume 329. Springer.

Della Monica, R. and de Martino, I. (2023). Bounding the mass of ultralight bosonic dark matter particles with the motion of the S2 star around Sgr A*. *Physical Review D*, 108(10):L101303.

Dermer, C. D. and Menon, G. (2009). *High Energy Radiation from Black Holes. Gamma Rays, Cosmic Rays, and Neutrinos*. Princeton Series in Astrophysics.

Dewangan, G. C., Tripathi, P., Papadakis, I. E., and Singh, K. P. (2021). AstroSat/UVIT observations of IC 4329A: constraining the accretion disc inner radius. *Monthly Notices of the RAS*, 504(3):4015–4023.

Done, C., Gierliński, M., and Kubota, A. (2007). Modelling the behaviour of accretion flows in X-ray binaries. Everything you always wanted to know about accretion but were afraid to ask. *The Astronomy and Astrophysics Review*, 15(1):1–66.

Dovčiak, M., Karas, V., and Yaqoob, T. (2004). An Extended Scheme for Fitting X-Ray Data with Accretion Disk Spectra in the Strong Gravity Regime. *The Astrophysical Journal Supplement*, 153(1):205–221.

Eardley, D. M. and Press, W. H. (1975). Astrophysical processes near black holes. *Annual Reviews of Astromy and Astrophysics*, 13:381–422.

Eckart, A. and Genzel, R. (1996). Observations of stellar proper motions near the Galactic Centre. *Nature*, 383(6599):415–417.

Eckart, A., Schödel, R., and Straubmeier, C. (2005). *The black hole at the center of the Milky Way*. Imperial College Press.

Einstein, A. (1915). Die Feldgleichungen der Gravitation. *Sitzungsberichte der Königlich Preussischen Akademie der Wissenschaften*, pages 844–847.

Elvis, M. (2000). A Structure for Quasars. *The Astrophysical Journal*, 545(1):63–76.

Esin, A. A., McClintock, J. E., and Narayan, R. (1997). Advection-Dominated Accretion and the Spectral States of Black Hole X-Ray Binaries: Application to Nova Muscae 1991. *The Astrophysical Journal*, 489(2):865–889.

Event Horizon Telescope Collaboration, et al. (2019a). First M87 Event Horizon Telescope Results. I. The Shadow of the Supermassive Black Hole. *The Astrophysical Journal Letters*, 875(1):L1.

Event Horizon Telescope Collaboration, et al. (2019b). First M87 Event Horizon Telescope Results. V. Physical Origin of the Asymmetric Ring. *The Astrophysical Journal Letters*, 875(1):L5.

Event Horizon Telescope Collaboration, et al. (2022). First Sagittarius A* Event Horizon Telescope Results. I. The Shadow of the Supermassive Black Hole in the Center of the Milky Way. *The Astrophysical Journal Letters*, 930(2):L12.

Fabian, A. C., Rees, M. J., Stella, L., and White, N. E. (1989). X-ray fluorescence from the inner disc in Cygnus X-1. *Monthly Notices of the Royal Astronomical Society*, 238:729–736.

Farris, B. D., Duffell, P., MacFadyen, A. I., and Haiman, Z. (2015). Characteristic signatures in the thermal emission from accreting binary black holes. *Monthly Notices of the RAS*, 446:L36–L40.

Fishbone, L. G. and Moncrief, V. (1976). Relativistic fluid disks in orbit around Kerr black holes. *The Astrophysical Journal*, 207:962–976.

Frank, J., King, A., and Raine, D. J. (2002). *Accretion Power in Astrophysics: Third Edition*. Cambridge University Press.

Fukue, J. (1992). Self-Irradiated Accretion Disks. *Publications of the ASJ*, 44:663–667.

Galeev, A. A., Rosner, R., and Vaiana, G. S. (1979). Structured coronae of accretion disks. *The Astrophysical Journal*, 229:318–326.

Genzel, R., Eckart, A., Ott, T., and Eisenhauer, F. (1997). On the nature of the dark mass in the centre of the Milky Way. *Monthly Notices of the RAS*, 291(1):219–234.

Gertsenshtein, M. E. (1961). Wave resonance of light and gravitational waves. *Journal of Experimental and Theoretical Physics*, 41:113–114.

Ghez, A. M., Klein, B. L., Morris, M., and Becklin, E. E. (1998). High Proper-Motion Stars in the Vicinity of Sagittarius A*: Evidence for a Supermassive Black Hole at the Center of Our Galaxy. *Astrophysical Journal*, 509(2):678–686.

Greene, J. E., Strader, J., and Ho, L. C. (2020). Intermediate-Mass Black Holes. *ARA&A*, 58:257–312.

Guan, L., Tang, X., Tian, J., and Wu, J. (2022). The principle and state-of-art approach for black hole detection. *Journal of Physics: Conference Series*, 2364:012053.

Gültekin, K. and Miller, J. M. (2012). Observable Consequences of Merger-driven Gaps and Holes in Black Hole Accretion Disks. *Astrophysical Journal*, 761(2):90.

Guolo, M., Pasham, D. R., Zajaček, M., Coughlin, E. R., Gezari, S., Suková, P., Wevers, T., Witzany, V., Tombesi, F., van Velzen, S., Alexander, K. D., Yao, Y., Arcodia, R., Karas, V., Miller-Jones, J. C. A., Remillard, R., Gendreau, K., and Ferrara, E. C. (2024). X-ray eruptions every 22 days from the nucleus of a nearby galaxy. *Nature Astronomy*.

Hagen, S. and Done, C. (2023). Estimating black hole spin from AGN SED fitting: the impact of general-relativistic ray tracing. *Monthly Notices of the Royal Astronomical Society*, 525(3):3455–3467.

Hazard, C., Mackey, M. B., and Shimmins, A. J. (1963). Investigation of the Radio Source 3C 273 By The Method of Lunar Occultations. *Nature*, 197(4872):1037–1039.

Hills, J. G. (1975). Possible power source of Seyfert galaxies and QSOs. *Nature*, 254(5498):295–298.

Honma, F. (1996). Global Structure of Bimodal Accretion Disks around a Black Hole. *Publications of the ASJ*, 48:77–87.

Hoyle, F. and Lyttleton, R. A. (1941). On the accretion theory of stellar evolution. *Monthly Notices of the Royal Astronomical Society*, 101:227.

Hubený, I. and Mihalas, D. (2014). *Theory of Stellar Atmospheres*. Princeton, NJ: Princeton University Press.

Ichimaru, S. (1977). Bimodal behavior of accretion disks: theory and application to Cygnus X-1 transitions. *Astrophysical Journal*, 214:840–855.

Kara, E. and et. al (2021). AGN STORM 2. I. First results: A Change in the Weather of Mrk 817. *Astrophysical Journal*, 922(2):151.

Karas, V. (2006). Theoretical aspects of relativistic spectral features. *Astronomische Nachrichten*, 327(10):961–968.

Karas, V., Czerny, B., Abrassart, A., and Abramowicz, M. A. (2000). A cloud model of active galactic nuclei: the iron Kα line diagnostics. *Monthly Notices of the Royal Astronomical Society*, 318(2):547–560.

Karas, V. and Kraus, P. (1996). Doppler Tomography of Relativistic Accretion Disks. *Publications of the ASJ*, 48:771–775.

Karas, V., Martocchia, A., and Subr, L. (2001). Variable Line Profiles Due to Non-Axisymmetric Patterns in an Accretion Disc around a Rotating Black Hole. *PASJ*, 53(2):189–199.

Karas, V. and Matt, G. (2007). *Black Holes from Stars to Galaxies – Across the Range of Masses*, volume 238. Cambridge: Cambridge University Press.

Karas, V., Vokrouhlicky, D., and Polnarev, A. G. (1992). In the vicinity of a rotating black hole : a fast numerical code for computing observational effects. *Monthly Notices of the Royal Astronomical Society*, 259:569–575.

Karas, V. and Šubr, L. (2001). Orbital decay of satellites crossing an accretion disc. *Astronomy and Astrophysics*, 376:686–696.

Kato, S., Fukue, J., and Mineshige, S. (2008). *Black-Hole Accretion Disks: Towards a New Paradigm.* Kyoto University Press.

Kato, S. and Nakamura, K. E. (1998). Transition Radius from Cooling-Dominated to Advection-Dominated Regimes in Two Temperature Disks. *Publications of the ASJ*, 50:559–566.

Kelley, L. Z., Blecha, L., and Hernquist, L. (2017). Massive black hole binary mergers in dynamical galactic environments. *Monthly Notices of the RAS*, 464(3):3131–3157.

Kerr, R. P. (1963). Gravitational Field of a Spinning Mass as an Example of Algebraically Special Metrics. *Physical Review Letters*, 11(5):237–238.

Klebesadel, R. W., Strong, I. B., and Olson, R. A. (1973). Observations of Gamma-Ray Bursts of Cosmic Origin. *The Astrophysical Journal Letters*, 182:L85.

Kojima, Y. (1991). The effects of black hole rotation on line profiles from accretion discs. *Monthly Notices of the Royal Astronomical Society*, 250:629–632.

Komossa, S. (2015). Tidal disruption of stars by supermassive black holes: Status of observations. *Journal of High Energy Astrophysics*, 7:148–157.

Kouveliotou, C., Meegan, C. A., Fishman, G. J., Bhat, N. P., Briggs, M. S., Koshut, T. M., Paciesas, W. S., and Pendleton, G. N. (1993). Identification of Two Classes of Gamma-Ray Bursts. *The Astrophysical Journal Letters*, 413:L101.

Krolik, J. H. (1999). *Active galactic nuclei : from the central black hole to the galactic environment.* Princeton University Press.

Krtička, J. and et al. (2023). Science with a small two-band UV-photometry mission II: Observations of stars and stellar systems. *arXiv e-prints*, page arXiv:2306.15081.

Kuncic, Z., Celotti, A., and Rees, M. J. (1997). Dense, thin clouds and reprocessed radiation in the central regions of active galactic nuclei. *Monthly Notices of the Royal Astronomical Society*, 284(3):717–730.

Lančová, D., Abarca, D., Kluźniak, W., Wielgus, M., Sądowski, A., Narayan, R., Schee, J., Török, G., and Abramowicz, M. (2019). Puffy Accretion Disks: Sub-Eddington, Optically Thick, and Stable. *The Astrophysical Journal Letters*, 884(2):L37.

Laor, A. (1991). Line Profiles from a Disk around a Rotating Black Hole. *The Astrophysical Journal*, 376:90.

Lawrence, A. (2018). Quasar viscosity crisis. *Nature Astronomy*, 2:102–103.

Linial, I. and Metzger, B. D. (2023). EMRI + TDE = QPE: Periodic X-Ray Flares from Star-Disk Collisions in Galactic Nuclei. *ApJ*, 957(1):34.

Linial, I. and Metzger, B. D. (2024). Ultraviolet Quasiperiodic Eruptions from Star–Disk Collisions in Galactic Nuclei. *ApJL*, 963(1):L1.

Liu, F. K., Li, S., and Komossa, S. (2014). A Milliparsec Supermassive Black Hole Binary Candidate in the Galaxy SDSS J120136.02+300305.5. *Astrophysical Journal*, 786(2):103.

Liu, Z., Malyali, A., Krumpe, M., Homan, D., Goodwin, A. J., Grotova, I., Kawka, A., Rau, A., Merloni, A., Anderson, G. E., Miller-Jones, J. C. A., Markowitz, A. G., Ciroi, S., Di Mille, F., Schramm, M., Tang, S., Buckley, D. A. H., Gromadzki, M., Jin, C., and Buchner, J. (2023). Deciphering the extreme X-ray variability of the nuclear transient eRASSt J045650.3−203750. A likely repeating partial tidal disruption event. *A&A*, 669:A75.

Loska, Z., Czerny, B., and Szczerba, R. (2004). Irradiation of accretion discs in active galactic nuclei due to the presence of a warm absorber. *Monthly Notices of the Royal Astronomical Society*, 355(4):1080–1090.

LSST, S. C. and et al. (2009). LSST Science Book, Version 2.0. *arXiv e-prints*, page arXiv:0912.0201.

Luminet, J. P. and Marck, J. A. (1985). Tidal squeezing of stars by Schwarzschild black holes. *Monthly Notices of the RAS*, 212:57–75.

Lynden-Bell, D. (1969). Galactic Nuclei as Collapsed Old Quasars. *Nature*, 223(5207):690–694.

Maggiore, M. (2018). *Gravitational Waves: Volume 2: Astrophysics and Cosmology.* Oxford University Press.

Magorrian, J., Tremaine, S., Richstone, D., Bender, R., Bower, G., Dressler, A., Faber, S. M., Gebhardt, K., Green, R., Grillmair, C., Kormendy, J., and Lauer, T. (1998). The Demography of Massive Dark Objects in Galaxy Centers. *Astronomical Journal*, 115:2285–2305.

Marsh, T. R. and Horne, K. (1988). Images of accretion discs - II. Doppler tomography. *Monthly Notices of the Royal Astronomical Society*, 235:269–286.

Matt, G., Perola, G. C., Piro, L., and Stella, L. (1992). Iron K-alpha line from X-ray illuminated relativistic disks. *Astronomy and Astrophysics*, 257:63–68.

McKernan, B., Ford, K. E. S., Kocsis, B., and Haiman, Z. (2013). Ripple effects and oscillations in the broad Fe Kα line as a probe of massive black hole mergers. *Monthly Notices of the Royal Astronomical Society*, 432(2):1468–1482.

McKinney, J. C. (2006). General relativistic magnetohydrodynamic simulations of the jet formation and large-scale propagation from black hole accretion systems. *Monthly Notices of the RAS*, 368(4):1561–1582.

Meier, D. L. (2012). *Black Hole Astrophysics: The Engine Paradigm.* Springer.

Melia, F. (2007). *The Galactic Supermassive Black Hole.* Princeton University Press.

Metzger, B. D., Stone, N. C., and Gilbaum, S. (2022). Interacting Stellar EMRIs as Sources of Quasi-periodic Eruptions in Galactic Nuclei. *Astrophysical Journal*, 926(1):101.

Miller, M. C. and Miller, J. M. (2015). The masses and spins of neutron stars and stellar-mass black holes. *Physics Reports*, 548:1–34.

Miniutti, G. and Fabian, A. C. (2004). A light bending model for the X-ray temporal and spectral properties of accreting black holes. *Monthly Notices of the Royal Astronomical Society*, 349(4):1435–1448.

Miniutti, G., Giustini, M., Arcodia, R., Saxton, R. D., Chakraborty, J., Read, A. M., and Kara, E. (2023a). Alive and kicking: A new QPE phase in GSN 069 revealing a quiescent luminosity threshold for QPEs. *A&A*, 674:L1.

Miniutti, G., Giustini, M., Arcodia, R., Saxton, R. D., Read, A. M., Bianchi, S., and Alexander, K. D. (2023b). Repeating tidal disruptions in GSN 069: Long-term evolution and constraints on quasi-periodic eruptions' models. *A&A*, 670:A93.

Miniutti, G., Saxton, R. D., Giustini, M., Alexander, K. D., Fender, R. P., Heywood, I., Monageng, I., Coriat, M., Tzioumis, A. K., Read, A. M., Knigge, C., Gandhi, P., Pretorius, M. L., and Agís-González, B. (2019). Nine-hour X-ray quasi-periodic eruptions from a low-mass black hole galactic nucleus. *Nature*, 573(7774):381–384.

Mirabel, F. (2017). The formation of stellar black holes. *New Astronomy Reviews*, 78:1–15.

Misner, C. W., Thorne, K. S., and Wheeler, J. A. (1973). *Gravitation*. San Francisco: W.H. Freeman and Co.

Moranchel-Basurto, A., Sánchez-Salcedo, F. J., Chametla, R. O., and Velázquez, P. F. (2021). Supernova Explosions in Accretion Disks in Active Galactic Nuclei: Three-dimensional Models. *Astrophysical Journal*, 906(1):15.

Morrissey, P. and et al. (2007). The Calibration and Data Products of GALEX. *Astrophysical Journal, Supplement*, 173(2):682–697.

Narayan, R., Igumenshchev, I. V., and Abramowicz, M. A. (2003). Magnetically Arrested Disk: an Energetically Efficient Accretion Flow. *Publications of the ASJ*, 55:L69–L72.

Narayan, R. and McClintock, J. E. (2008). Advection-dominated accretion and the black hole event horizon. *New Astronomy Reviews*, 51(10-12):733–751.

Narayan, R. and Yi, I. (1994). Advection-dominated Accretion: A Self-similar Solution. *ApJL*, 428:L13.

Netzer, H. (2019). Bolometric correction factors for active galactic nuclei. *Monthly Notices of the RAS*, 488(4):5185–5191.

Newman, E. T., Couch, E., Chinnapared, K., Exton, A., Prakash, A., and Torrence, R. (1965). Metric of a Rotating, Charged Mass. *Journal of Mathematical Physics*, 6(6):918–919.

Nordström, G. (1918). On the Energy of the Gravitation field in Einstein's Theory. *Koninklijke Nederlandse Akademie van Wetenschappen Proceedings Series B Physical Sciences*, 20:1238–1245.

Parsa, M., Eckart, A., Shahzamanian, B., Karas, V., Zajaček, M., Zensus, J. A., and Straubmeier, C. (2017). Investigating the Relativistic Motion of the Stars Near the Supermassive Black Hole in the Galactic Center. *The Astrophysical Journal*, 845(1):22.

Pasham, D. R., Coughlin, E. R., Zajacek, M., Linial, I., Sukova, P., Nixon, C. J., Janiuk, A., Sniegowska, M., Witzany, V., Karas, V., Krumpe, M., Altamirano, D., Wevers, T., and Arcodia, R. (2024a). Alive but Barely Kicking: News from 3+ years of Swift and XMM-Newton X-ray Monitoring of Quasi-Periodic Eruptions from eRO-QPE1. *ApJL, accepted; arXiv e-prints*, page arXiv:2402.09690.

Pasham, D. R., Tombesi, F., Sukova, P., Zajacek, M., Rakshit, S., Coughlin, E., Kosec, P., Karas, V., Masterson, M., Mummery, A., Holoien, T. W. S., Guolo, M., Hinkle, J., Ripperda, B., Witzany, V., Shappee, B., Kara, E., Horesh, A., van Velzen, S., Sfaradi, I., Kaplan, D. L., Burger, N., Murphy, T., Remillard, R., Steiner, J. F., Wevers, T., Arcodia, R., Buchner, J., Merloni, A., Malyali, A., Fabian, A., Fausnaugh, M., Daylan, T., Altamirano, D., Payne, A., and Ferrara, E. C. (2024b). A Case for a Binary Black Hole System Revealed via Quasi-Periodic Outflows. *arXiv e-prints*, page arXiv:2402.10140.

Pecháček, T., Dovčiak, M., and Karas, V. (2005). The relativistic shift of spectral lines from black-hole accretion discs. In Hledík, S. and Stuchlík, Z., editors, *RAGtime 6/7: Workshops on black holes and neutron stars*, pages 137–141.

Penrose, R. and Floyd, R. M. (1971). Extraction of Rotational Energy from a Black Hole. *Nature Physical Science*, 229(6):177–179.

Peters, P. C. (1964). Gravitational Radiation and the Motion of Two Point Masses. *Physical Review*, 136(4B):1224–1232.

Poole, T. S. and et al. (2008). Photometric calibration of the Swift ultraviolet/optical telescope. *Monthly Notices of the RAS*, 383(2):627–645.

Poutanen, J., Veledina, A., and Zdziarski, A. A. (2018). Doughnut strikes sandwich: the geometry of hot medium in accreting black hole X-ray binaries. *Astronomy and Astrophysics*, 614:A79.

Pringle, J. E. (1981). Accretion discs in astrophysics. *Annual Reviews of Astronomy and Astrophysics*, 19:137–162.

Pringle, J. E. and Rees, M. J. (1972). Accretion Disc Models for Compact X-Ray Sources. *Astronomy and Astrophysics*, 21:1.

Punsly, B. (2001). *Black hole gravitohydromagnetics.* Springer.

Raine, D. and Thomas, E. (2009). *BLACK HOLES: An Introduction*. Imperial College Press.

Rees, M. J. (1988). Tidal disruption of stars by black holes of 10^6-10^8 solar masses in nearby galaxies. *Nature*, 333(6173):523–528.

Rein, H. (2012). Planet-disc interaction in highly inclined systems. *MNRAS*, 422(4):3611–3616.

Reissner, H. (1916). Über die Eigengravitation des elektrischen Feldes nach der Einsteinschen Theorie. *Annalen der Physik*, 355(9):106–120.

Reynolds, C. S. (2021). Observational Constraints on Black Hole Spin. *ARA&A*, 59:117–154.

Ricci, C., Kara, E., Loewenstein, M., Trakhtenbrot, B., Arcavi, I., Remillard, R., Fabian, A. C., Gendreau, K. C., Arzoumanian, Z., Li, R., Ho, L. C., MacLeod, C. L., Cackett, E., Altamirano, D., Gandhi, P., Kosec, P., Pasham, D., Steiner, J., and Chan, C. H. (2020). The Destruction and Recreation of the X-Ray Corona in a Changing-look Active Galactic Nucleus. *The Astrophysical Journal Letters*, 898(1):L1.

Richstone, D., Ajhar, E. A., Bender, R., Bower, G., Dressler, A., Faber, S. M., Filippenko, A. V., Gebhardt, K., Green, R., Ho, L. C., Kormendy, J., Lauer, T. R., Magorrian, J., and Tremaine, S. (1998). Supermassive black holes and the evolution of galaxies. *Nature*, 385(6701):A14.

Rossi, B. and Olbert, S. (1970). *Introduction to the physics of space*. McGraw-Hill Inc., US.

Sanbuichi, K., Yamada, T. T., and Fukue, J. (1993). Self-Irradiated Accretion Disks around Schwarzschild Black Holes. *Publications of the ASJ*, 45:443–448.

Sazonov, S. and et al. (2021). First tidal disruption events discovered by srg/erosita: X-ray/optical properties and x-ray luminosity function at z<0.6. *Monthly Notices of the Royal Astronomical Society*, 508(3):3820–3847.

Schmidt, M. (1963). 3C 273 : A Star-Like Object with Large Red-Shift. *Nature*, 197(4872):1040.

Schnittman, J. D. (2006). *Radiation Transport Around Kerr Black Holes*. PhD thesis, -.

Schwarz, G. (1978). Estimating the Dimension of a Model. *Annals of Statistics*, 6(2):461–464.

Schwarzschild, K. (1916). On the Gravitational Field of a Mass Point According to Einstein's Theory. *Abh. Konigl. Preuss. Akad. Wissenschaften Jahre 1906,92, Berlin,1907*, 1916:189–196.

Semerák, O., Karas, V., and de Felice, F. (1999). Parameters of Black Holes in Sources with Periodic Variability. *PASJ*, 51:571.

Shakura, N. I. and Sunyaev, R. A. (1973a). Black holes in binary systems. Observational appearance. *Astronomy and Astrophysics*, 24:337–355.

Shakura, N. I. and Sunyaev, R. A. (1973b). Reprint of 1973A&A....24..337S. Black holes in binary systems. Observational appearance. *Astronomy and Astrophysics*, 500:33–51.

Shapiro, S. L. and Teukolsky, S. A. (1983). *Black Holes, White Dwarfs, and Neutron Stars: the Physics of Compact Objects.* New York: Wiley.

Sicilia, A., Lapi, A., Boco, L., Shankar, F., Alexander, D. M., Allevato, V., Villforth, C., Massardi, M., Spera, M., Bressan, A., and Danese, L. (2022). The Black Hole Mass Function across Cosmic Time. II. Heavy Seeds and (Super)Massive Black Holes. *ApJ*, 934(1):66.

Sochora, V., Karas, V., Svoboda, J., and Dovčiak, M. (2011). Black hole accretion rings revealed by future X-ray spectroscopy. *Monthly Notices of the Royal Astronomical Society*, 418(1):276–283.

Soltan, A. (1982). Masses of quasars. *Monthly Notices of the RAS*, 200:115–122.

Stone, N. C. (2015). *The Tidal Disruption of Stars by Supermassive Black Holes: An Analytic Approach.* Springer.

Suková, P., Zajaček, M., and Karas, V. (2023). MAD UFOs: Magnetically Arrested Discs with persistent Ultra-Fast Outflows. *arXiv e-prints*, page arXiv:2312.04149.

Suková, P., Zajaček, M., Witzany, V., and Karas, V. (2021). Stellar Transits across a Magnetized Accretion Torus as a Mechanism for Plasmoid Ejection. *ApJ*, 917(1):43.

Svensson, R. and Zdziarski, A. A. (1994). Black Hole Accretion Disks with Coronae. *The Astrophysical Journal*, 436:599.

Syer, D., Clarke, C. J., and Rees, M. J. (1991). Star-disc interactions near a massive black hole. *Monthly Notices of the RAS*, 250:505–512.

Tanaka, Y., Nandra, K., Fabian, A. C., Inoue, H., Otani, C., Dotani, T., Hayashida, K., Iwasawa, K., Kii, T., Kunieda, H., Makino, F., and Matsuoka, M. (1995). Gravitationally redshifted emission implying an accretion disk and massive black hole in the active galaxy MCG-6-30-15. *Nature*, 375(6533):659–661.

Tiesinga, E., Mohr, P. J., Newell, D. B., and Taylor, B. N. (2021). CODATA recommended values of the fundamental physical constants: 2018. *Reviews of Modern Physics*, 93(2):025010.

Urry, C. M. and Padovani, P. (1995). Unified Schemes for Radio-Loud Active Galactic Nuclei. *Publications of the ASP*, 107:803.

Vestergaard, M. and Peterson, B. M. (2006). Determining Central Black Hole Masses in Distant Active Galaxies and Quasars. II. Improved Optical and UV Scaling Relationships. *Astrophysical Journal*, 641(2):689–709.

Volonteri, M., Haardt, F., and Madau, P. (2003). The Assembly and Merging History of Supermassive Black Holes in Hierarchical Models of Galaxy Formation. *Astrophysical Journal*, 582(2):559–573.

Volonteri, M., Habouzit, M., and Colpi, M. (2021). The origins of massive black holes. *Nature Reviews Physics*, 3(11):732–743.

Štolc, M. and Karas, V. (2019). Tidal disruption events as a site of an evolving relativistic spectral line. *Astronomische Nachrichten*, 340(7):570–576.

Štolc, M., Zajaček, M., Czerny, B., and Karas, V. (2023). Spectral energy distribution profiles from AGN accretion disc in multigap set-up. *Monthly Notices of the Royal Astronomical Society*, 522(2):2869–2884.

Štolc, M., Zajaček, M., and Karas, V. (2020). From gappy to ringed: signatures of an accretion disk radial structure in profiles of the reflection line. *in Blak Holes, Proceedings of RAGtime, edited by Z. Stuchl ík, G. Török, and V. Karas (Silesian University in Opava, Czech Republic)*, 20–22(2):287–297.

Šubr, L. and Karas, V. (1999). An orbiter crossing an accretion disc. *Astronomy and Astrophysics*, 352:452–458.

Wald, R. M. (1972). Electromagnetic Fields and Massive Bodies. *Physical Review D*, 6(6):1476–1479.

Werner, N. and et al. (2022). Quick Ultra-VIolet Kilonova surveyor (QUVIK). In den Herder, J.-W. A., Nikzad, S., and Nakazawa, K., editors, *Space Telescopes and Instrumentation 2022: Ultraviolet to Gamma Ray*, volume 12181 of *Society of Photo-Optical Instrumentation Engineers (SPIE) Conference Series*, page 121810B.

Werner, N. and et al. (2023). Science with a small two-band UV-photometry mission I: Mission description and follow-up observations of stellar transients. *arXiv e-prints*, page arXiv:2306.15080.

Werner, N., Řípa, J., Thöne, C., Münz, F., Kurfürst, P., Jelínek, M., Hroch, F., Benáček, J., Topinka, M., Lukes-Gerakopoulos, G., Zajaček, M., Labaj, M., Prišegen, M., Krtička, J., Merc, J., Pál, A., Pejcha, O., Dániel, V., Jon, J., Šošovička, R., Gromeš, J., Václavík, J., Steiger, L., SegiÅák, J., Behar, E., Tarem, S., Salh, J., Reich, O., Ben-Ami, S., Barschke, M. F., Berge, D., Tohuvavohu, A., Sivanandam, S., Bulla, M., Popov, S., and Chang, H.-K. (2024). Science with a Small Two-Band UV-Photometry Mission I: Mission Description and Follow-up Observations of Stellar Transients. *Space Science Reviews*, 220(1):11.

Wright, E. L. and et al. (2010). The Wide-field Infrared Survey Explorer (WISE): Mission Description and Initial On-orbit Performance. *The Astronomical Journal*, 140(6):1868–1881.

Wu, Y., Baum, S., Freese, K., Visinelli, L., and Yu, H.-B. (2022). Dark stars powered by self-interacting dark matter. *Physical Review D*, 106(4):043028.

Yuan, F. and Narayan, R. (2014). Hot Accretion Flows Around Black Holes. *ARA&A*, 52:529–588.

Zajaček, M., Czerny, B., Jaiswal, V. K., Štolc, M., Karas, V., Pasham, D. R., Śniegowska, M., Witzany, V., Suková, P., Münz, F., Werner, N., Řípa, J., Merc, J., Labaj, M., and Kurfürst, P. (2024). Science with a small two-band UV-photometry mission III: Active Galactic Nuclei and nuclear transients. *Space Sci Rev*, 220(3):29.

Zajaček, M., Karas, V., and Eckart, A. (2014). Dust-enshrouded star near supermassive black hole: predictions for high-eccentricity passages near low-luminosity galactic nuclei. *Astronomy and Astrophysics*, 565:A17.

Zajaček, M., Tursunov, A., Eckart, A., and Britzen, S. (2018). On the charge of the Galactic centre black hole. *Monthly Notices of the Royal Astronomical Society*, 480(4):4408–4423.

Zdziarski, A. A. (1998). Hot accretion discs with thermal Comptonization and advection in luminous black hole sources. *Monthly Notices of the Royal Astronomical Society*, 296(4):L51–l55.

Zdziarski, A. A., You, B., and Szanecki, M. (2022). Corrections to Estimated Accretion Disk Size due to Color Correction, Disk Truncation, and Disk Wind. *Astrophysical Journal, Letters*, 939(1):L2.

Zeldovich, Y. B. and Novikov, I. D. (1971). *Relativistic astrophysics. Vol.1: Stars and relativity.* The University of Chicago Press.

Zhou, C., Huang, L., Guo, K., Li, Y.-P., and Pan, Z. (2024). Probing orbits of stellar mass objects deep in galactic nuclei with quasi-periodic eruptions. *arXiv e-prints*, page arXiv:2401.11190.

List of candidate's publications

The author of the thesis claims the authorship (/co-authorship) of the following articles, categorized in chronologically descending order, labeled as refereed and non-refereed according to the ADS, NASA Astrophysics Data System.

Publications in refereed journals

M. Zajaček, B. Czerny, V. K. Jaiswal, M. Štolc, V. Karas, D. R. Pasham, M. Śniegowska, V. Witzany, P. Suková, F. Münz, N. Werner, J. Řípa, J. Merc, M. Labaj, and P. Kurfürst. Science with a small two-band UV-photometry mission III: Active Galactic Nuclei and nuclear transients. *Space Science Reviews*, 220(3):29, 2024.

M. Štolc, M. Zajaček, B. Czerny, and V. Karas. Spectral energy distribution profiles from AGN accretion disc in multigap set-up. *Monthly Notices of the Royal Astronomical Society*, 522(2):2869–2884, 2023.

M. Štolc and V. Karas. Tidal disruption events as a site of an evolving relativistic spectral line. *Astronomische Nachrichten*, 340(7):570–576, 2019.

Publications in proceedings

V. Karas, K. Klimovičová, D. Lančová, M. Štolc, J. Svoboda, G. Török, M. Matuszková, E. Šrámková, R. Šprňa, and M. Urbanec. Timing of accreting neutron stars with future X-ray instruments: towards new constraints on dense matter equation of state. *Contributions of the Astronomical Observatory Skalnaté Pleso*, vol. 53, no. 4, p. 175-190, 12/2023.

M. Štolc, M. Zajaček, and V. Karas. From gappy to ringed: signatures of an accretion disk radial structure in profiles of the reflection line. in Black Holes. In *Proceedings of RAGtime*, edited by Z. Stuchlík, G. Török, and V. Karas (Silesian University in Opava, Czech Republic), 20–22(2):287–297, 2020.

M. Zajaček, A. Araudo, V. Karas, B. Czerny, A. Eckart, P. Suková, M. Štolc, and V. Witzany. Missing bright red giants in the Galactic center: A fingerprint of its once active state? In *Proceedings of RAGtime*, edited by Z. Stuchlík, G. Török, and V. Karas (Silesian University in Opava, Czech Republic), 20–22(2): 1–18, 2020.

M. Štolc, V. Karas, P. Suková, V. Witzany, and M. Zajaček. Gappy Accretion Disc: Theoretical Profiles of a Relativistic Spectral Line, in *WDS'20 Proceedings of Contributed Papers* — Physics (eds. J. Šafránková and J. Pavlů), Prague, Matfyzpress, pp. 59–64, 2020.

Active participation at conferences and workshops

The author of this thesis has contributed at the following conferences and workshops (chronologically in descending order).

European Astronomical Society Annual Meeting, 2023 (Kraków, PL)
Poster presentation: Modelling SED profile signatures in the context of gappy accretion discs

31st Texas Symposium on Relativistic Astrophysics, 2022 (Prague, CZ); and
24th Relativistic Astrophysics Group Meeting, 2022 (Opava, CZ)
Poster presentation: Interplay between SED and spectral line profiles in the context of gappy accretion discs

Black-hole activity feedback from Bondi-radius to galaxy-cluster scales, 2022 (Brno, CZ)
Oral presentation: Interplay between SED and spectral line profiles in the context of gappy accretion discs

22nd Relativistic Astrophysics Group Meeting, 2020 (Opava, CZ)
Oral presentation: From gappy to ringed: signatures of the accretion disk radial structure in profiles of the reflection line

Week of Doctoral Students, 2020 (Prague, CZ)
Oral presentation: A gappy accretion disc: theoretical profiles of a relativistic spectral line

Meeting of Observational High Energy Astrophysics Group, Shanghai Astronomical Observatory, 2019 (Shanghai, CN)
Oral presentation: Tidal disruption events as a site of an evolving relativistic spectral line

Cologne-Prague student exchange program, 2019 (Cologne, DE)
Oral presentation: Tidal disruption events as a site of an evolving relativistic spectral line

INTEGRAL/BART Workshop, 2019 (Karlovy Vary, CZ)
Oral presentation: Tidal disruption events as a site of an evolving relativistic spectral line

A. Additional tables

For completeness, below we add the Tables A.1, A.2, A.3 and A.4 representing the fit results in Scenario I, the altered Scenario I and the Scenario II, respectively. The mock data were generated using the list of detectors from Table 3.6, whereas we replaced the GALEX's FUV and NUV filters by QUVIK's. The assumed additional instrumental error is up to 2% an 10% in the measured flux, respectively.

We conclude that the fitting based on the implementation of either GALEX or its substitute - QUVIK - show effectively consistent results, with only small changes in the magnitude of the uncertainties of the fit parameters (for reference see the Tables 3.2, 3.3, 3.4 and 3.5). The changes are, however, expected to be caused due to the slight change of the values of central wavelengths for the FUV and NUV filters (for comparison between GALEX and QUVIK see Tables 3.1 and 3.6, respectively).

assumed values		fit values		
$\dot{m}$	R_{ADAF} (R_{g})	$\dot{m}$	R_{ADAF} (R_{g})	χ^2_ν
z=0				
0.4	11	0.42 ± 0.03	13 ± 3	1.3
0.4	25	0.42 ± 0.03	27 ± 3	1.5
z=0.5				
0.4	11	0.37 ± 0.02	9 ± 1	1.2
0.4	25	0.41 ± 0.03	25 ± 2	1.3
z=1				
0.4	11	0.40 ± 0.02	11 ± 1	1.1
0.4	25	0.40 ± 0.03	25 ± 1	1.3
z=1.5				
0.4	11	0.41 ± 0.02	11 ± 1	1.1
0.4	25	0.39 ± 0.03	24 ± 1	1.5
z=2				
0.4	11	0.39 ± 0.02	11 ± 1	1.2
0.4	25	0.38 ± 0.02	25 ± 1	1.1

Table A.1: Best fit results for the Scenario I from the sect. 2.3. The accretion rather has been frozen as indicated in the first column; two values of the inner coronal (ADAF) radius are shown. The remaining fixed parameters are identical to those of the Tab. 3.2 on p. 54.

assumed values			fit values			
$E(B-V)$	$\dot{m}$	R_{ADAF} (R_{g})	$E(B-V)$	$\dot{m}$	R_{ADAF} (R_{g})	χ^2_ν
z=0						
0.15	0.4	11	0.13 ± 0.04	0.37 ± 0.03	12 ± 9	1.5
0.15	0.4	25	0.13 ± 0.03	0.39 ± 0.03	28 ± 8	1.2
z=0.5						
0.15	0.4	11	0.14 ± 0.02	0.41 ± 0.03	11 ± 3	1.2
0.15	0.4	25	0.17 ± 0.02	0.43 ± 0.03	22 ± 3	1.2
z=1						
0.15	0.4	11	0.13 ± 0.01	0.38 ± 0.03	14 ± 1	1
0.15	0.4	25	0.14 ± 0.02	0.39 ± 0.04	25 ± 2	1.3
z=1.5						
0.15	0.4	11	0.15 ± 0.01	0.41 ± 0.04	11 ± 1	1.2
0.15	0.4	25	0.15 ± 0.01	0.41 ± 0.04	25 ± 1	1.1
z=2						
0.15	0.4	11	0.16 ± 0.01	0.43 ± 0.04	11 ± 1	1.2
0.15	0.4	25	0.15 ± 0.01	0.37 ± 0.04	24 ± 1	1.2

Table A.2: Best fit results for the altered Scenario I from the sect. 2.4. The fixed parameters are identical to those of Tab. 3.3 on p. 55.

assumed values			fit values								inferred values	
$\dot{m}$	$R_{\mathrm{gap\,in}}$ (R_{g})	$R_{\mathrm{gap\,out}}$ (R_{g})	$\dot{m}$	$R_{\mathrm{gap\,in}}$ (R_{g})	$R_{\mathrm{gap\,out}}$ (R_{g})	χ^2_ν	AIC	BIC	$\Delta\ AIC$	$\Delta\ BIC$	d (R_{g})	M_2 $(10^7 M_\odot)$
z=0												
0.4	170	230	0.44 ± 0.05	209 ± 67	338 ± 95	1.6	9.8	12.1	–	–	274 ± 58	3.94 ± 10.93
0.4	170	170	0.36 ± 0.02	–	–	1.8	10.7	11.5	0.9	–0.6	–	–
0.4	340	460	0.44 ± 0.03	535 ± 144	965 ± 291	1.5	8.7	11	–	–	750 ± 162	7.07 ± 16.66
0.4	340	340	0.38 ± 0.02	–	–	2.4	14.7	15.5	6	4.5	–	–
0.4	680	920	0.41 ± 0.03	400 ± 147	626 ± 229	1.5	9.7	12	–	–	513 ± 136	3.21 ± 11.86
0.4	680	680	0.36 ± 0.02	–	–	2	11.8	12.6	2.1	0.6	–	–
z=0.5												
0.4	170	230	0.39 ± 0.03	113 ± 63	139 ± 73	1	3.3	5.6	–	–	126 ± 48	0.33 ± 3.69
0.4	170	170	0.36 ± 0.01	–	–	1	0.7	1.5	–2.6	–4.1	–	–
0.4	340	460	0.40 ± 0.03	297 ± 141	416 ± 210	1.4	7.7	10	–	–	357 ± 126	1.40 ± 9.02
0.4	340	340	0.37 ± 0.02	–	–	1.6	8	8.8	0.3	–1.2	–	–
0.4	680	920	0.42 ± 0.02	416 ± 111	698 ± 236	1.1	4.1	6.4	–	–	557 ± 130	4.87 ± 13.93
0.4	680	680	0.38 ± 0.02	–	–	1.6	8.7	9.5	4.6	3.1	–	–
z=1												
0.4	170	230	0.42 ± 0.04	52 ± 22	68 ± 29	1.2	5.2	7.6	–	–	60 ± 18	0.71 ± 4.90
0.4	170	170	0.38 ± 0.01	–	–	1.1	3.2	4	–2	–3.6	–	–
0.4	340	460	0.42 ± 0.03	202 ± 168	247 ± 211	1.5	9.4	11.7	–	–	225 ± 135	0.30 ± 5.46
0.4	340	340	0.40 ± 0.02	–	–	1.5	6.9	7.7	–2.5	–4	–	–
0.4	680	920	0.41 ± 0.02	471 ± 173	761 ± 296	1.6	10.5	12.8	–	–	616 ± 171	3.92 ± 1.43
0.4	680	680	0.39 ± 0.02	–	–	1.8	10.1	10.9	–0.4	–1.9	–	–

Table continued on the next page.

assumed values			fit values								inferred values	
$\dot{m}$	$R_{\mathrm{gap\,in}}$ (R_{g})	$R_{\mathrm{gap\,out}}$ (R_{g})	$\dot{m}$	$R_{\mathrm{gap\,in}}$ (R_{g})	$R_{\mathrm{gap\,out}}$ (R_{g})	χ^2_ν	AIC	BIC	$\Delta\ AIC$	$\Delta\ BIC$	d (R_{g})	M_2 $(10^7 M_\odot)$
z=1.5												
0.4	170	230	0.43 ± 0.02	110 ± 26	183 ± 44	1	2.9	5.2	–	–	147 ± 26	4.64 ± 10.05
0.4	170	170	0.37 ± 0.02	–	–	2	11.8	12.6	8.9	7.4	–	–
0.4	340	460	0.39 ± 0.02	495 ± 260	805 ± 354	1.3	7.4	9.7	–	–	650 ± 220	4.07 ± 17.78
0.4	340	340	0.38 ± 0.01	–	–	1.6	8.3	9.1	0.9	–0.6	–	–
0.4	680	920	0.40 ± 0.02	477 ± 264	799 ± 371	1.8	12.5	14.8	–	–	638 ± 228	4.82 ± 21.10
0.4	680	680	0.39 ± 0.02	–	–	2.1	12.5	13.2	0	–1.6	–	–
z=2												
0.4	170	230	0.40 ± 0.02	187 ± 82	263 ± 144	1.2	6	8.4	–	–	225 ± 83	1.45 ± 9.59
0.4	170	170	0.38 ± 0.01	–	–	1.4	5.8	6.6	–0.2	–1.8	–	–
0.4	340	460	0.39 ± 0.02	166 ± 67	239 ± 119	1.2	5.5	7.8	–	–	203 ± 68	1.76 ± 10.02
0.4	340	340	0.37 ± 0.01	–	–	1.4	6.6	7.3	1.1	–0.5	–	–
0.4	680	920	0.41 ± 0.02	331 ± 103	650 ± 170	1.2	5.5	7.8	–	–	491 ± 99	10.32 ± 20.28
0.4	680	680	0.39 ± 0.02	–	–	1.8	10.6	11.4	5.1	3.6	–	–

Table A.3: Best fit results for the Scenario II from the sect. 2.5. The fixed parameters are identical to those of Tab. 3.4 on p. 57.

assumed values			fit values								inferred values	
$\dot{m}$	$R_{\mathrm{gap\,in}}$ (R_{g})	$R_{\mathrm{gap\,out}}$ (R_{g})	$\dot{m}$	$R_{\mathrm{gap\,in}}$ (R_{g})	$R_{\mathrm{gap\,out}}$ (R_{g})	χ^2_ν	AIC	BIC	$\Delta\ AIC$	$\Delta\ BIC$	d (R_{g})	M_2 $(10^7 M_\odot)$
					z=0							
0.4	170	230	0.41 ± 0.01	166 ± 14	243 ± 19	1.8	12.3	14.6	–	–	205 ± 12	2.00 ± 1.88
0.4	170	170	0.34 ± 0.01	–	–	7	31.1	32.9	18.8	18.3	–	–
0.4	340	460	0.40 ± 0.01	363 ± 32	505 ± 42	1.1	4.3	6.6	–	–	434 ± 26	1.32 ± 1.49
0.4	340	340	0.36 ± 0.01	–	–	8.3	34.9	35.7	30.6	29.1	–	–
0.4	680	920	0.40 ± 0.01	748 ± 92	986 ± 130	1.5	8.9	11.2	–	–	867 ± 80	0.78 ± 1.57
0.4	680	680	0.38 ± 0.01	–	–	5.8	29.2	30	20.3	18.8	–	–
					z=0.5							
0.4	170	230	0.39 ± 0.01	158 ± 17	200 ± 20	1	3.1	5.5	–	–	179 ± 13	0.49 ± 0.92
0.4	170	170	0.36 ± 0.01	–	–	4.3	24.4	25.2	21.3	19.7	–	–
0.4	340	460	0.41 ± 0.01	280 ± 32	385 ± 46	1.7	10.9	13.2	–	–	333 ± 28	1.18 ± 1.92
0.4	340	340	0.37 ± 0.01	–	–	9	36.1	36.9	25.2	23.7	–	–
0.4	680	920	0.400 ± 0.004	747 ± 77	1039 ± 106	1.4	7.5	9.8	–	–	893 ± 66	1.31 ± 1.79
0.4	680	680	0.39 ± 0.01	–	–	5.4	28.1	28.8	20.6	19	–	–
					z=1							
0.4	170	230	0.40 ± 0.01	162 ± 17	218 ± 23	1.5	8.7	11	–	–	190 ± 14	0.96 ± 1.49
0.4	170	170	0.37 ± 0.01	–	–	8.6	35.4	36.1	26.7	25.1	–	–
0.4	340	460	0.394 ± 0.004	368 ± 52	462 ± 75	1.2	5.9	8.2	–	–	415 ± 46	0.44 ± 1.28
0.4	340	340	0.382 ± 0.005	–	–	3.5	21	21.8	15.1	13.6	–	–
0.4	680	920	0.393 ± 0.003	691 ± 109	912 ± 131	1.2	5.3	7.6	–	–	802 ± 85	0.79 ± 1.84
0.4	680	680	0.39 ± 0.01	–	–	3.9	22.9	23.7	17.6	16.1	–	–

Table continued on the next page.

assumed values			fit values								inferred values	
$\dot{m}$	$R_{\mathrm{gap\,in}}$ (R_{g})	$R_{\mathrm{gap\,out}}$ (R_{g})	$\dot{m}$	$R_{\mathrm{gap\,in}}$ (R_{g})	$R_{\mathrm{gap\,out}}$ (R_{g})	χ^2_ν	AIC	BIC	Δ AIC	Δ BIC	d (R_{g})	M_2 $(10^7 M_\odot)$
z=1.5												
0.4	170	230	0.394 ± 0.004	197 ± 18	274 ± 30	1.2	5	7.3	–	–	246 ± 17	1.31 ± 1.81
0.4	170	170	0.37 ± 0.01	–	–	8.5	35.3	36	30.3	28.7	–	–
0.4	340	460	0.391 ± 0.003	461 ± 86	555 ± 102	1.1	4.6	6.7	–	–	508 ± 67	0.24 ± 1.02
0.4	340	340	0.385 ± 0.004	–	–	2.1	12.7	13.5	8.1	6.8	–	–
0.4	680	920	0.399 ± 0.003	758 ± 255	995 ± 307	1.1	4.1	6.4	–	–	877 ± 200	0.74 ± 3.78
0.4	680	680	0.39 ± 0.01	–	–	4.6	25.4	26.1	21.3	19.7	–	–
z=2												
0.4	170	230	0.399 ± 0.005	157 ± 21	209 ± 32	1.8	11.9	14.2	–	–	183 ± 19	0.86 ± 1.92
0.4	170	170	0.38 ± 0.01	–	–	7.5	33.1	33.9	21.2	19.7	–	–
0.4	340	460	0.398 ± 0.003	306 ± 29	422 ± 41	1.1	4.1	6.4	–	–	364 ± 25	1.22 ± 1.60
0.4	340	340	0.39 ± 0.01	–	–	4.5	25.1	25.9	21	19.5	–	–
0.4	680	920	0.396 ± 0.003	575 ± 165	802 ± 207	1.2	5.9	8.3	–	–	689 ± 132	1.35 ± 4.77
0.4	680	680	0.39 ± 0.01	–	–	6.5	31	31.8	25.1	23.5	–	–

Table A.4: Best fit results for the Scenario II from the sect. 2.5. The fixed parameters are identical to those of Tab. 3.5 on p. 59.

List of Figures

List of Tables

Values of selected constants

For convenience of the reader we select here several fundamental physics constants that are frequently used throughout the calculations and we list their values as a quick reference. For an authoritative overview with precise and updated values of constants and conversion factors, see Tiesinga et al. (2021). For reference we also list the derived physical quantities with the corresponding transformation factor.

Quantity	Value (CGS)
Boltzmann constant	$k = 1.38 \times 10^{-16}$ cm^2 g s^{-2} K
Newtonian's gravitational constant	$G = 6.67 \times 10^{-8}$ cm^3 g^{-1} s
Planck constant	$h = 6.63 \times 10^{-27}$ cm^2 g s^{-1}
Proton mass	$m_\mathrm{p} = 1.67 \times 10^{-24}$ g
Solar mass	$M_\odot = 2.00 \times 10^{33}$ g
Speed of light	$c = 3.00 \times 10^{10}$ cm s^{-1}
Stefan-Boltzmann constant	$\sigma = 5.67 \times 10^{-5}$ erg cm^{-2} s^{-1} K^{-4}
Thompson cross section	$\sigma_\mathrm{T} = 6.65 \times 10^{-25}$ cm^2

Physical quantity	Notation	Transformation factor (CGS) *)
Gravitational radius	R_g	1.48×10^{14} cm
Eddington accretion rate	$\dot{M}_\mathrm{Edd}$	6.74×10^{26} g s^{-1}
Eddington luminosity	L_Edd	1.26×10^{47} erg

*) Assumed primary mass was set to $10^9 M_\odot$.

CGS to geometrized units

Geometrized units are well adapted to the equations of gravitational physics, General Relativity in particular. Also, normalization of the variables to suitable dimensionless form is often introduced in order to reduce complexities of numerical factors, enhance the clarity of formulas and avoid the risk of trivial mistakes. We refer the reader to the most useful and detailed overview in Misner et al. (1973). After setting $c = G = 1$ the transformation factors between CGS and geometrized units are based on the following relations

$$\begin{aligned} 1\,\mathrm{g} &\leftrightarrow 7.41 \times 10^{-29}\,\mathrm{cm}, \\ 1\,\mathrm{s} &\leftrightarrow 3 \times 10^{10}\,\mathrm{cm}. \end{aligned}$$

Abbreviations and acronyms

For convenience we provide a list of abbreviations and acronyms used throughout the text (alphabetic order):

ADAF - Advection dominated accretion flow
AGN - Active galactic nucleus
EHT - Event Horizon Telescope
EMRI - Extreme-Mass Ratio Inspiral
FWHM - Full width at half maximum
GRB - Gamma-ray burst
IMBH - Intermediate-mass black hole
ISCO - Innermost stable circular orbit
LMXB - Low-Mass X-ray Binary
LSST - Legacy Survey of Space and Time
MAD - Magnetically Arrested Disc
MHD - Magnetohydrodynamic
QPE - Quasi-Periodic Eruption
QPO - Quasi-Periodic Oscillation
QPOut - Quasi-Periodic Outflow
QUVIK - Quick Ultra-VIolet Kilonova surveyor
RIAF - Radiatively inefficient accretion flow
RNT - Repeating Nuclear Transient
SED - Spectral energy distribution
SMBH - Supermassive black hole
TDE - Tidal disruption event